中華民國顯微鏡學會

第28屆學術研討會彙刊

PROCEEDINGS OF THE 28TH R.O.C. SYMPOSIUM ON MICROSCOPY

中華民國九十七年六月二十一日
台中市　　中台科技大學
June 21, 2008
Central Taiwan University
of Science and Technology
Taichung, Taiwan

EBT 超泰科技有限公司
E. B. TECH. CO., LTD

專業的電子顯微鏡,材料分析儀器,耗材,相關設備代理商
Electron Microscope, Analysis instruments, Sample preparation tools

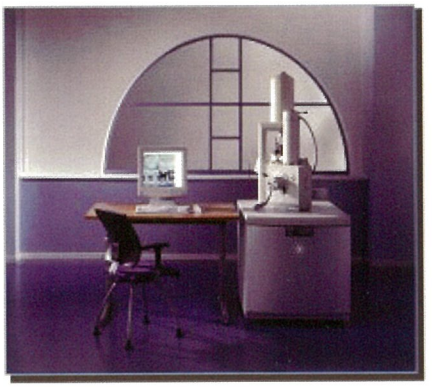

FEI 環境式可變真空掃描電子顯微鏡

FISCHIONE Ion Miller

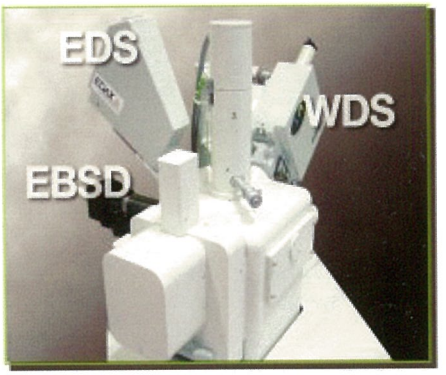

EDAX AMETEK TSL EBSD+EDS+WDS

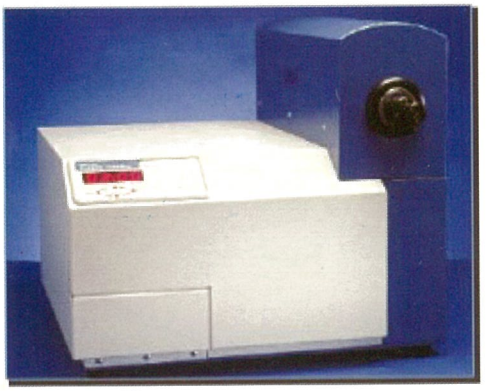

FISCHIONE Plasma Cleaner

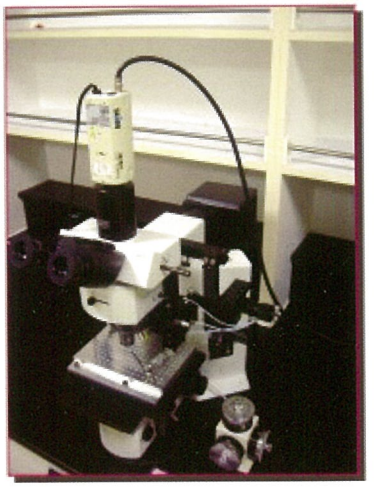

EBT 光學及試片吸針系統

EDAX AMETEK X-光螢光分析儀(XRF)

台北市信義區吳興街156巷16弄7號1樓
電話:(02)2733-2576 傳真:(02)2733-5546
Http://www.ebtech.com.tw
E-mail:service@ebtech.com.tw

目　錄

頁數

中 華 民 國 顯 微 鏡 學 會

PROCEEDINGS OF THE 28TH SYMPOSIUM ON MICROSCOPY

June 21, 2008, Pei-Tun, Central Taiwan University of Science and Technology

830 – 9:30	Registration	
9:30 – 10:00	Opening Ceremony (耕書樓 地下一樓 順之廳)	
10:00 -10:50	Yukihito Kondo	OPERATIONAL PRINCIPLE AND APPLICATION OF Cs CORRECTOR
11:00-11:50	胡宇光	DEVELOPMENT AND APPLICATION OF 20 NM RESOLUTION HARD-X-RAY MICROSCOPY
12:00-13:00	第十四屆第一次中華民國顯微鏡學會年會會員大會	
13:00-14:00	Lunch (耕書樓 二樓 第二會議室)	
Chairs	耕書樓 二樓 第二會議室 (BIOMEDICAL SCIENCE): 黃玲瓏、陳淑華	
14:00-14:15	高資棟	MICROSCOPIC STUDY ON THE STRUCTURE AND COMPOSITION OF FALSE VEIN OF *PTERIS GREVILLEANA* (PTERIDACEAE)
14:15-14:30	顧銓	COMPARISON OF ULTRASTRUCTURE OF *FAGUS* L. (FAGACEAE) POLLEN FROM EXTANT AND FOSSIL SAMPLES IN TAIWAN
14:30-15:00	COFFEE BREAK (耕書樓 二樓 第二會議室)	
Chairs	耕書樓 二樓 第二會議室 (BIOMEDICIAL SCIENCE): 楊瑞森、鄭瓊娟	
15:00-15:15	高肇孚	MICROSTRUCTURE OF MS2 INFECTING ON E. COLI
15:15-15:30	華子恩	IMAGING SUB-CELLULAR STRUCTUTRES WITH ULTRAHIGH RESOLUTION RADIOLOGY
Chairs	耕書樓 地下一樓 順之廳 (MATERIAL SCIENCE): 開執中、陳福榮	
14:00-14:15	曾傳銘	CRYSTALLOGRAPHIC AND LOCAL ELECTRONIC STRUCTURES OF NANOCHECKERBOARDS IN MN-DOPED COBALT FERRITE
14:15-14:30	謝佾蒼	THE MICROSTRUCTURAL EVOLUTION OF NUCLEAR GRADE GRAPHITE IN VERY HIGH TEMPERATURE GAS COOLED REACTORT (VHTGR) CORE ENVIRONMENTS
1430-14:45	陳科夆	HIGH TEMPERATURE TRIPLE-ION BEAM IRRADIATION EFFECT ON HELIUM BUBBLE FORMATION IN Hi-NICALON TYPE-S SiC_f/SiC COMPOSITE
14:45-15:00	COFFEE BREAK (耕書樓 二樓 第二會議室)	
Chairs	耕書樓 地下一樓 順之廳 (MATERIAL SCIENCE): 楊哲人、林招松	
15:00-15:15	李偉任	EFFECTS OF REPEATED IMMERSIONS ON THE FORMATION OF CERIUM NITRATE CONVERSION COATINGS ON AZ31 MAGNESIUM ALLOY
15:15-15:30	顏鴻威	TEM AND HADDF-STEM INVESTIGATION ON NANOMETER-SIZED CARBIDES IN ULTRAHIGH-STRENGTH STEELS
15:30-15:45	蔡篤承	INFLUENCE OF APPLYING A BIAS ON THE CHARACTERISTICS OF TiVCr ALLOY THIN FILMS PREPARED BY DC SPUTTERING
16:10 – 17:00	討論、頒獎、摸彩、閉幕 (耕書樓 地下一樓 順之廳)	

中華民國顯微鏡學會

第十三屆理、監事名錄

理 事 長	游祥明	中臺科技大學護理學院護理系	教授
副理事長	陳福榮	清華大學工程與系統科學系	教授
常務理事	張　立	交通大學材料科學與工程學系	教授
	黃玲瓏	台灣大學生命科學系	教授
	薛富盛	中興大學材料工程學系	教授
理　　事	沈博彥	中山大學材料科學研究所	教授
	林鶴南	清華大學材料科學與工程學系	教授
	陳正弦	台灣大學凝態中心	主任
	開　物	海洋大學材料工程研究所	教授
	黃宏圖	中山大學生物科學系	教授
	黃榮南	台灣大學昆蟲學系	教授
	楊哲人	台灣大學材料科學研究所	教授
	楊瑞森	海洋大學海洋生物研究所	教授
	劉康庭	友聯光學股份有限公司	董事長
	蘇紘儀	台灣積體電路公司	故障分析處處長
常務監事	李志浩	清大工程與系統科學系	教授
監　　事	林招松	台灣大學材料科學研究所	教授
	張庭訓	捷東股份有限公司	董事長
	胡宇光	中央研究院物理研究所	研究員
	陳玉怜	台灣大學醫學院解剖暨細胞生物學研究所	教授
榮譽理事	李英雄	中國醫藥學院研發處	研發長
	侯書文	台灣大學醫學院病理科	教授
	陳脈紀	中興大學植物病蟲害系	教授
	吳信淦	中央研究院植物所	研究員
	林良平	台灣大學農化系	教授
	陳力俊	清華大學科學工程學系	教授
	開執中	清華大學工程與系統科學系	教授
秘 書 長	鄭瓊娟	陽明大學醫學院解剖暨細胞生物學研究所	教授

中華民國顯微鏡學會新會員入會申請書

(一)姓名:_____ 性別:_____

(二)服務機關:_____ 職務:_____

(三)通訊處:_____

_____

Phone: *Fax:*

E-mail:

(四)學歷: 畢業年月

(1)

(2)

(五)經歷:

(1)

(2)

(六)主要研究領域:

(1)

(2)

(3)

(七)申請入會為

(1)永久會員:入會費 NT.600	永久會費 NT.3000
(2)一般會員:入會費 NT.600	常年會費 NT.500
(3)學生會員:入會費 NT.200	常年會費 NT.200
(4)團體會員:入會費 NT.10,000	常年會費 NT.5000

(八)介紹人

(1)姓名:_____ 簽章:_____ 服務機關與職務:_____

(2)姓名:_____ 簽章:_____ 服務機關與職務:_____

(九)申請人簽章:_____

中華民國 年 月 日

【表一】

中華民國顯微鏡學會九十六年收支決算表

(96 年 1 月 1 日至 96 年 12 月 31 日)

單位：新台幣

科目				決算數	上年度決算數	本年度與上年度決算比較數		說明
款	項	目	名稱			增加	減少	
1			本會經費收入	150,480	199,716			
	1		入會費、會員年費	28,200	38,600		10,400	
	2		其他收入	106,000	155,000		49,000	
	3		利息收入	16,280	6,116	10,164		
2			本會經費支出	171,118	171,837			
	1		辦公費	11,628	72,337		60,709	
		1	文具及其他印刷費	10,544	61,515		50,971	
		2	郵電費	1,084	10,822		9,738	
	2		業務費	87,090	41,700	45,390		
	3		學會會刊印刷費	60,000	31,800	28,200		
	4		臨時工資	12,400	26,000		13,600	
3			本期餘絀	**-20,638**	27,879			

理事長：　秘書長：　會計及製表：張秀晶　出納：

【表二】

中華民國顯微鏡學會

現金出納表

中華民國 96 年 12 月 31 日

單位：新台幣

收入之部		支出之部	
科目名稱	金額	科目名稱	金額
上期結存	1,217,986	本期結存	1,197,348
本期收入	150,480		
本期支出	171,118		
合計	1,197,348	合計	1,197,348

理事長：　　秘書長：　　會計及製表：張秀昌　　出納：

【表三】

中華民國顯微鏡學會

資產負債表

中華民國 96 年 12 月 31 日

單位：新台幣

資產		負債、基金及餘絀	
科目	金額	科目	金額
郵局存款—活存	197,348		
郵局存款—定存	1,000,000	餘絀	1,197,348
合計	1,197,348	合計	1,197,348

理事長：　　秘書長：　　會計及製表：張秀[illegible]　　出納：

【表四】

中華民國顯微鏡學會九十七年收支預算表

(97 年 1 月 1 日至 97 年 12 月 31 日)

單位：新台幣

科目				預算數	上年度預算數	本年度與上年度預算比較數		說明
款	項	目	名稱			增加	減少	
1			本會經費收入	160,000	180,000			
	1		入會費、會員年費	30,000	34,000		4,000	
	2		其他收入	110,000	140,000		30,000	
	3		利息收入	20,000	6,000	14,000		
2			本會經費支出	160,000	180,000			
	1		車馬費	0	10,000		10,000	
	2		辦公費	20,000	70,000		50,000	
		1	文具及其他印刷費	15,000	60,000		45,000	
		2	郵電費	5,000	10,000		5,000	
	3		業務費	60,000	30,000	30,000		
	4		學會會刊印刷費	60,000	40,000	20,000		
	5		臨時工資	20,000	30,000		10,000	
3			本期餘絀	0	0			

理事長：　　秘書長：　　會計及製表：張秀晶　　出納：

主題演講

論文宣讀

[生物醫農組]

[材料物理組]

論文壁報

[生物醫農組]

[材料物理組]

P-1 OPERATIONAL PRINCIPLE AND APPLICATION OF Cs CORRECTOR

Yukihito Kondo

Electron Optics Division, JEOL Ltd.

Transmission and scanning transmission microscopy, the revolutionary progresses are proceeding owing to a spherical aberration correction technique. The progresses are not only in resolution but also in analytical sensitivity. These enable us to have an individual atomic column analysis by combination with electron energy loss spectroscopy (EELS).

Spherical aberration collectors (Cs corrector) are categorized into two, one is for a probe forming system (STEM Cs corrector) to serve extremely fine probe below 0.1 nm diameter, and the other is for image forming lens system to serve a ultrahigh resolution around 0.1 nm, when acceleration of electron is 200 kV. Spherical aberration collector is composed of two hexapoles and two sets of transfer doublet lens systems. The hexapole creates the negative Cs aberration for canceling the positive Cs of objective lens and large three-fold astigmatism that is undesirable for image and probe forming. The created undesirable three-fold astigmatism in the first hexapole is canceled out by the reversely excited second hexapole. Thus, we can utilize the negative Cs effectively.

In the presentation, the operating principle and the application results will be shown. The applications are highly resolved images and high spatial resolution analysis of the materials.

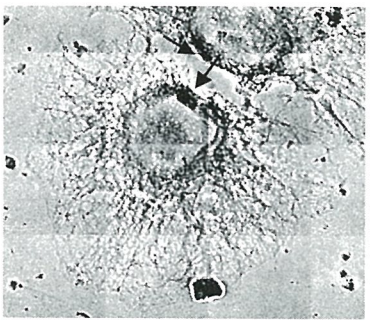

Fig. 1 PANC-1 cells immuno-stained for α-tubulin.
Scale bar, 10μm.

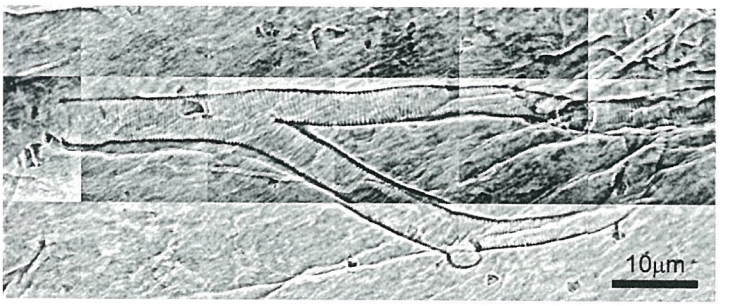

Fig. 2 Muscle fiber in the Drosophila NMJ stained with OsO_4 and uranyl acetate.

B-P-2 MICROSTRUCTURE OF MS2 INFECTING ON E. COLI

KAO, Chao-Fu(高肇孚)[1]; CHU, Zi-Wei(朱志偉)[2]; WU, Chun-Chun(吳純純)[2] and YANG, Jui-Sen(楊瑞森)[1]

[1]Institute of Marine Biology, National Taiwan Ocean University, Keelung, Taiwan
[2]Department of Applied Mathematics, Feng Chia University, Taichung, Taiwan

Phage MS2 was prepared by negative staining for electron microscope examination. Microstructure of MS2 infecting on *E. coli* was studied with reconstruction software by using EM images. MS2 with an ssRNA contains four proteins including a capsid coat protein, a replicase, a lysis protein and an attachment protein. The phage shows an icosahedral particle. A few MS2 were free particles without attachment (Fig. 1 & 2). Most of MS2 were found to attach on the flagella of bacteria(Fig. 3 & 4). Microstructure of attaching MS2 was different from that of free MS2. An attachment face seemed to be showed in EM images.

References

1. Valegard, K., Liljas, L., Fridborg and Unge, T. Nature 1990 (345) 36
2. Bamford, D. H., Burneth, R. M. and Stuart, D. I. Theo. Popul. Biol. 2002 (61) 461
3. Ruprech, J. and Nield, J. Preg. Biophys. Mol. Biol. 2001 (75) 121

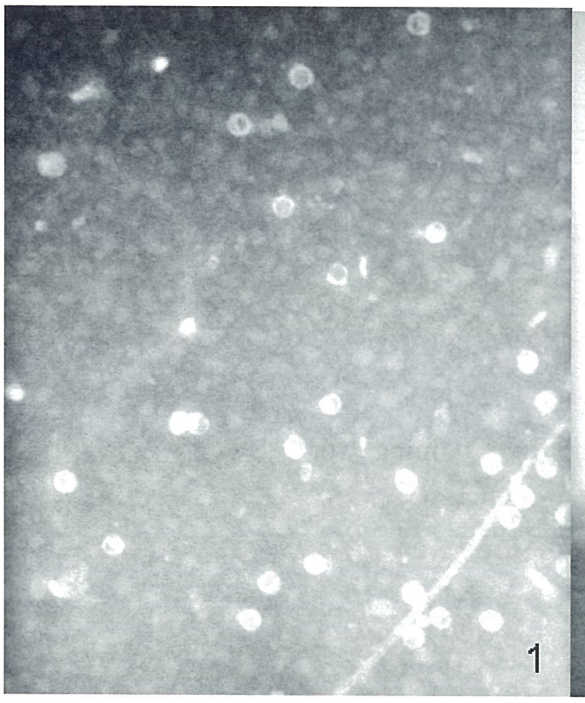

Fig. 1. Phage MS2, free particles.

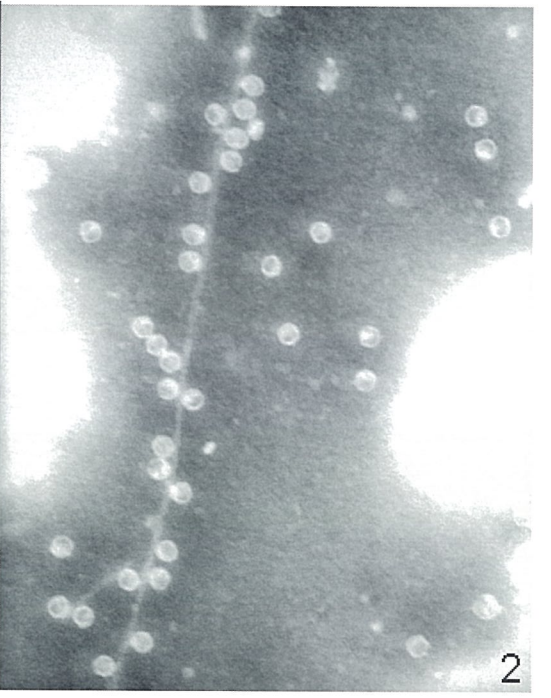

Fig. 2. Phage MS2, attaching particles.

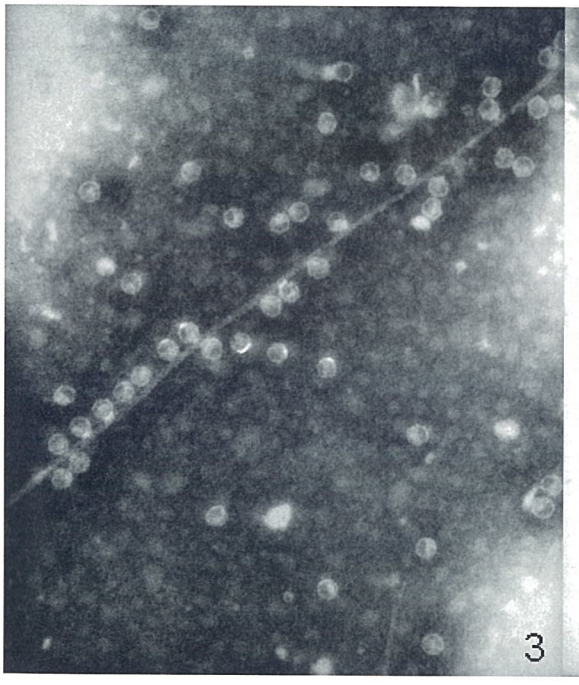

Fig. 3. Phage MS2, attaching particles.

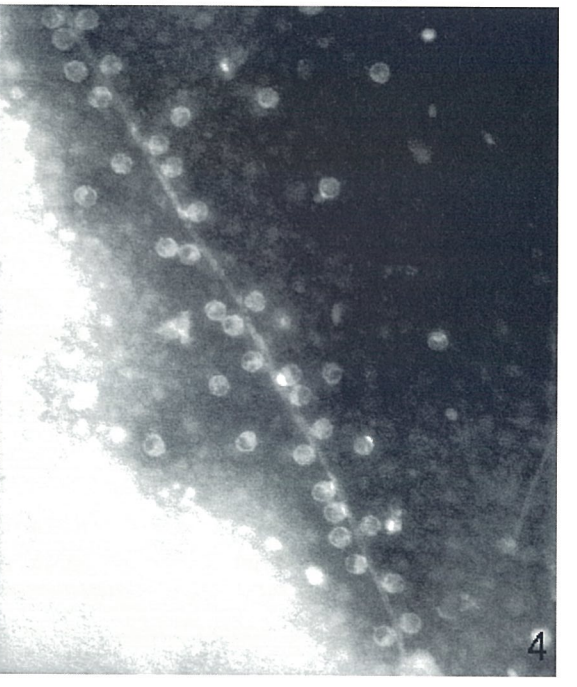

Fig. 4. Phage MS2, attaching particles.

B-P-3 COMPARISON OF SEM MICROSCOPIC STRUCTURE OF *FAGUS* L. (FAGACEAE) POLLEN FROM EXTANT AND FOSSIL SAMPLES IN TAIWAN

KU, Chuan(顧銓) and CHEN, Su-Hwa(陳淑華)

Department of Life Science, National Taiwan University, Taipei, Taiwan

In Taiwan, *Fagus hayatae* L. is the single species of its genus, which is confined to a few mountain ridges in northern Taiwan in a relic-like distribution pattern. However, fossil pollen strongly indicative of *Fagus* was found in lake, basin and deltaic sediments in northern and central Taiwan during the middle Pleistocene (ca. 0.40-0.4 mya) [1]. The *Fagus* pollen from lake sediments in Yilan reached its highest amount about 295 kya [2] and showed great morphological variation, suggesting more than one beech species were present in Taiwan [1]. This study is aimed at distinguishing fossil *Fagus* pollen by SEM microscopic structures and giving a systematic measurement of *Fagus* pollen in Taiwan.

The extant and fresh *F. hayatae* pollen, samples collected from Takaishan and Taipingshan, were treated with acetolysis. For fossil pollen, clay sediments from Yilan [2] were first treated with 47% HF overnight, boiled in 10% KOH for 5 min and finally treated with acetolysis. The solutions of treated fresh pollen and sediments were dropped onto tape on aluminum stubs, dried overnight, coated with gold in a Hitachi Ion Sputter (E-1010) and examined in a FEI Quanta 200 scanning electron microscope. To identify *Fagus* pollen in lake sediments, pollen exine ornamentation was examined carefully to find the distinctive vermiculate pattern of this genus [3]. Lengths of equatorial axes, polar axes and colpi and other characters were measured.

The identification of fossil *Fagus* pollen was supported by its SEM microscopic structure along with LM observations. The vermiculate elements of extant *F. hayatae* pollen had widths of about 0.22 μm while those of the fossil pollen had widths from 0.17 to 0.29 μm. There was no obvious morphological difference between the fresh pollen samples from Takaishan (FIG. 1-FIG. 2) and Taipingshan (FIG. 3-FIG. 4) except for the more clustered pattern of sculptural elements of the Taipingshan sample. The morphology of most fossil *Fagus* pollen was quite different from that of the extant *F. hayatae* pollen. Some fossil *Fagus* pollen had short colpi (FIG. 5) and some others extremely long colpi (FIG. 6). Some fossil pollen had wide and short rodlets (FIG. 7) and some others narrow and long rodlets (FIG. 8). In conclusion, the morphological variation of certain characters of the fossil *Fagus* pollen far exceeds that of the extant *F. hayatae* pollen. It is hence speculated that at least two other *Fagus* species existed in Taiwan.

References

1. Liew, P.-M., Shen, C.-F. and Huang, S.-Y. J. Geol. Soc. China 1994 (37) 549.
2. Liew, P.-M., and Huang, S.-Y. J. Geol. Soc. China 1994 (37) 115.
3. Denk, T. Plant Syst. Evol. 2003 (240) 55.

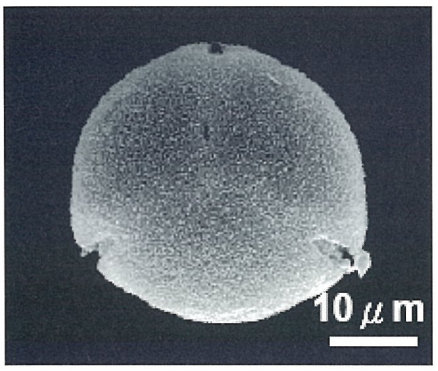

FIG. 1

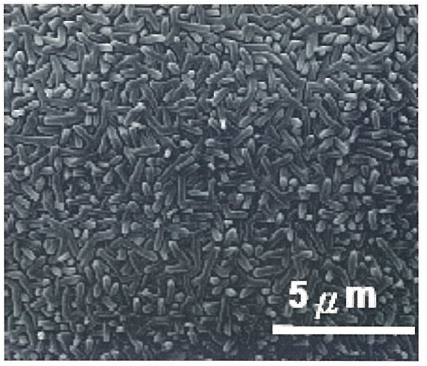

FIG. 2

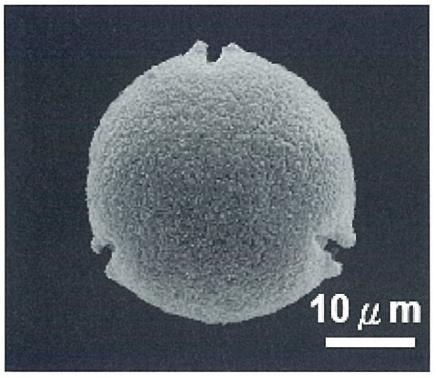

FIG. 3

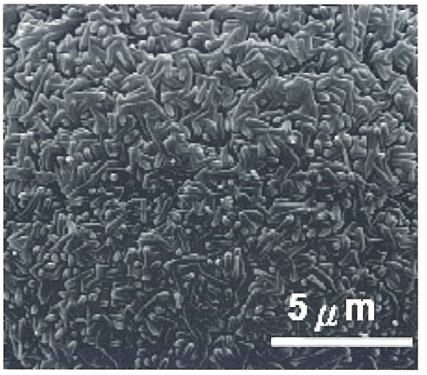

FIG. 4

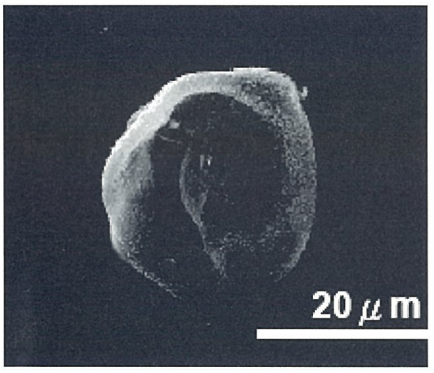

FIG. 5

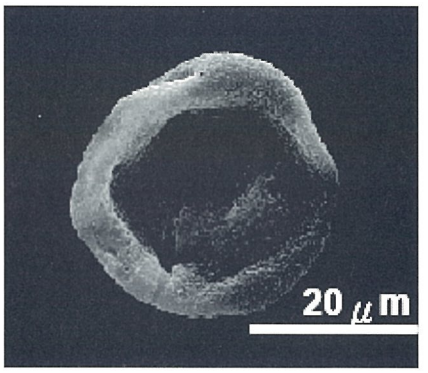

FIG. 6

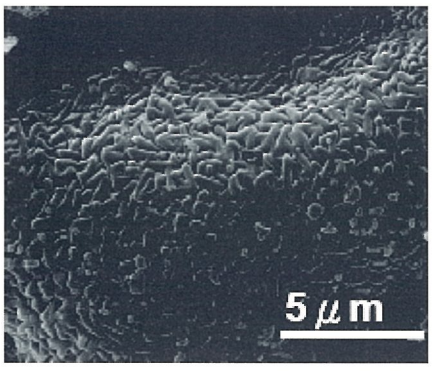

FIG. 7

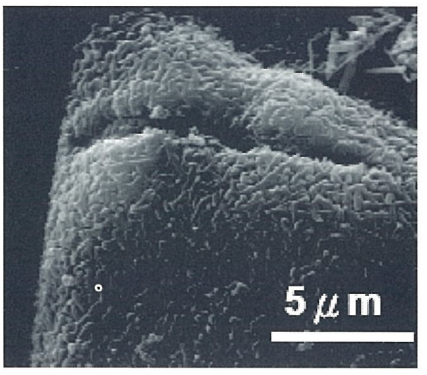

FIG. 8

B-P-4 MICROSCOPIC STUDY ON THE STRUCTURE AND COMPOSITION OF FALSE VEIN OF *PTERIS GREVILLEANA* (PTERIDACEAE)

KAO, Tzu-Tong(高資棟)[1]; CHEN, Shiang-Jiuun(陳香君)[1]; CHIOU, Wen-liang(邱文良)[2]; and KUO-HUANG, Ling-Long (黃玲瓏)[1],

[1] Department of Life Science, Institute of Ecology and Evolutionary Biology, National Taiwan University, 1 Roosevelt Rd., Sec. 4, Taipei 106, Taiwan.
[2] Division of Forest Biology, Taiwan Forestry Research Institute, 53 Nan-Hai Rd., Taipei 100, Taiwan

False vein density is an important character for species identification in genus *Pteris*. However, the structure and composition of false vein are still not well documented. In this report, we have used several microscopic techniques, including clearing (Fig. A), paraffin sectioning (Fig. D), SEM (Figs. B, C, and I-K), wet oxidation (L), and histochemical staining to study false veins in *Pteris grevilleana*. We confirmed that the false vein of *P. grevilleana* is composes of epidermal idioblasts[1]. Epidermal idioblasts are very elongated epidermal cells 200 ~ 1200μm in length scattered on interveinal regions or along tertiary veins and leaf margin of both upper and lower epidermis. On midrib, secondary veins, and indusium no idioblast was found. By using partial polarizing condition, a crystal-like structure was found in the idioblasts (Figs. E-H). By using EDS for trace element analysis, we found the leaf surface deposits mass of silica. Si dot mapping shows the correlation between Si depositions and the distribution of epidermal idioblasts (Figs. J, K). Individual silica bodies were isolated from epidermal idioblasts with wet oxidation method[2]. The silica bodies have two undulating ridges parallel to each other and slight concave at the center of its long axis. Epidermal idioblasts or silica bodies of *P. grevilleana* can also be stained by dyes including SAC (Silver-ammine chromate), CVL (Crystal Violet Lactone), and MR (Methyl Red) [3], which design for stain silica bodies of herbaceous monocots.

References

(1) Wagner, Jr. W. H. Acta Phytotax. Geobot., 1978 (29) 33.
(2) Piperno, D. R. Phytoliths, 2006.
(3) Dayanandan, P., Kaufman, P. B., and Franlin, C. I. Amer. J. Bot., 1983 (70) 1079

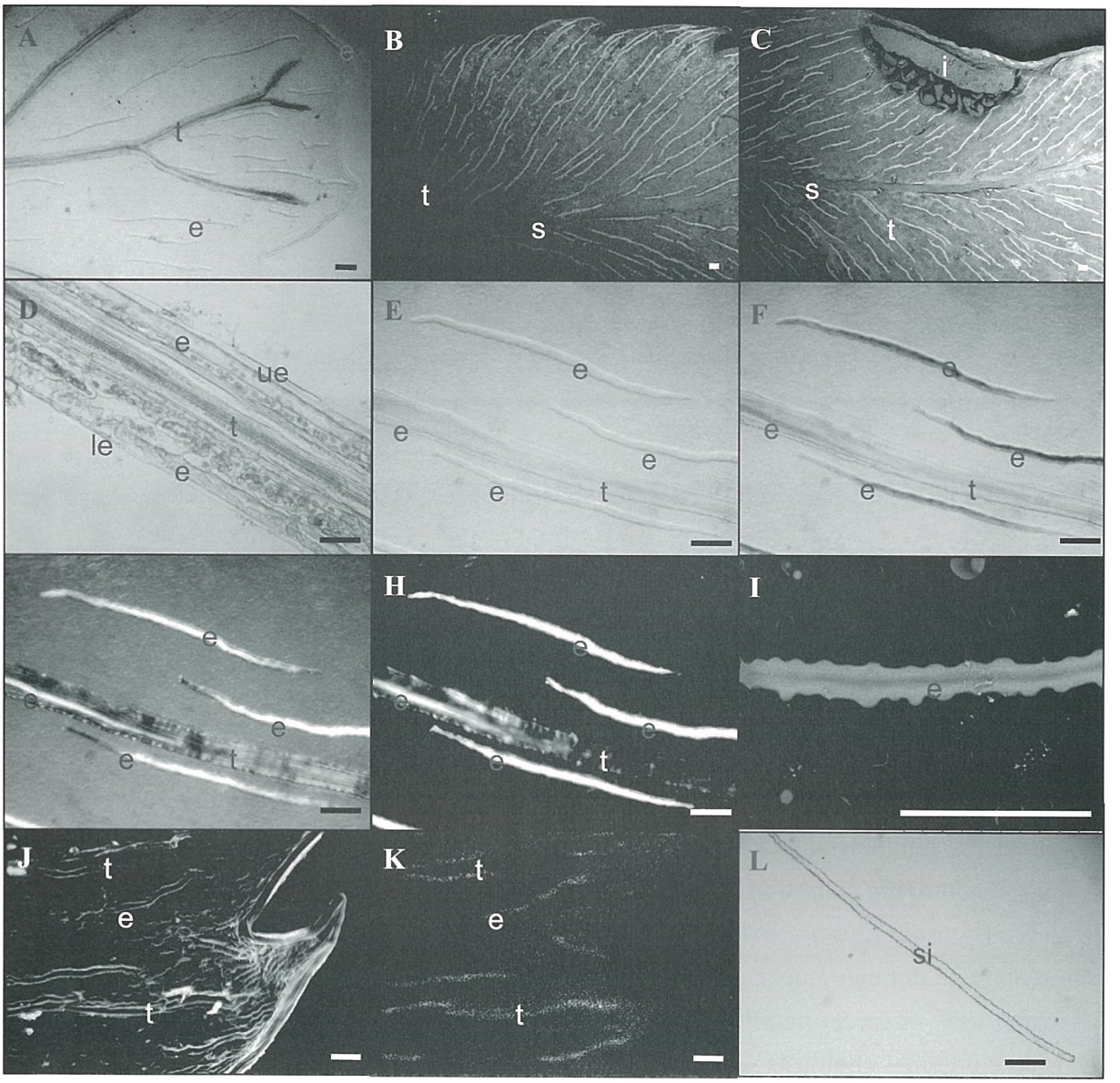

Figures. False veins of *P. grevilleana* observed under different microscopic techniques. **A.** Treat sample with clearing techniques. **B. and C.** Untreated leaf samples observed by a table-top SEM. **B.** Adaxial view. **C.** Abaxial view. **D.** Paraveinal section of leaf, sample embedded by paraffin. **E-H.** Different polarized condition (**E.** 0°, **F.** 30°, **G.** 60°, and **H.** 90°) were used to observe the tertiary vein and epidermal idioblasts. **I.** Surface structure of an idioblast. Sample treat with chloroform and observed under table-top SEM. **J.** leaf adaxial view under SEM **K.** Si dot mapping silica on Fig. J. **L.** Silica body isolated from idioblasts by wet oxidation technique. Scale bar = 100μm. e: epidermal idioblast; le: lower epidermis; s: secondary vein; si: silica bodies; t: tertiary vein; ue: upper epidermis.

B-P-5 MOLECULAR MECHANISM OF THE DOMINANT-NEGATIVE EFFECTS OF P/Q-TYPE Ca^{2+} CHANNEL MUTATIONS ASSOCIATED WITH EA2

JENG, Chung-Jiuan (鄭瓊娟)[1]; SUN, Min-Chen (孫閔貞)[2]; CHEN, Yi-Wen (陳怡文)[2]; and TANG, Chih-Yung (湯志永)[2]

[1]Institute of Anatomy & Cell Biology, College of Medicine, National Yang-Ming Univ., Taipei, Taiwan

[2]Dept. of Physiology, College of Medicine, National Taiwan Univ., Taipei, Taiwan.

Episodic ataxia type 2 (EA2) is an autosomal dominant neurological disorder associated with mutations in the gene encoding pore-forming α_{1A} subunits of human P/Q-type calcium ($Ca_V2.1$) channels. The exact mechanism of how mutant channels cause such clinical EA2 features as cerebellar dysfunctions, however, remains unclear. Our previous functional studies in *Xenopus* oocytes support the idea that EA2 mutants may exert prominent dominant-negative effects on wild-type $Ca_V2.1$ channels. To further pursue the mechanism underlying this dominant-negative effect, we examined the effects of EA2 mutants on the subcellular localization pattern of GFP-tagged wild-type $Ca_V2.1$ channels in HEK293T cells. In the presence of EA2 mutants, wild-type channels displayed a significant deficiency in membrane targeting and a concurrent increase in cytoplasm retention. Moreover, the cytoplasmic fraction of wild-type channels co-localized with an endoplasmic reticulum (ER) marker, suggesting that a significant amount of wild-type $Ca_V2.1$ channels was trapped in the ER. This EA2 mutant-induced ER retention pattern was reversed by lowering the cell incubation temperature from 37 to 27 °C. We also inspected the effects of untagged EA2 mutants on the functional expression of GFP-tagged wild-type $Ca_V2.1$ channels in HEK293T cells. Whole-cell current density of wild-type channels was diminished in the presence of EA2 mutants, which was also reversed by 27°C incubation. Finally, biochemical analyses indicated that EA2 mutants did not significantly affect the protein expression level of wild-type channels. Taken together, our data suggest that EA2 mutants induce significant ER retention of their wild-type counterparts, thereby suppressing the functional expression of $Ca_V2.1$ channels.

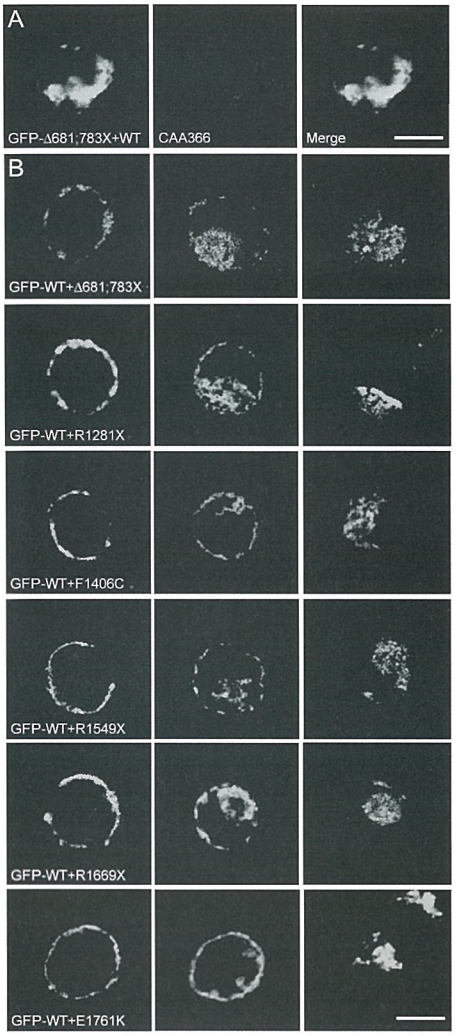

Figure 1. HEK293T cells co-expressing wild-type and EA2 mutant CaV2.1 channels. (A) Cells co-transfected with untagged wild-type α1A subunit and GFP-tagged mutant α1A-Δ681;783X, as well as auxiliary α2δ and β4 subunits. The cells were also counterstained with the CAA366 antibody which recognized the wild-type α1A subunit but not the mutant α1A-Δ681;783X. Note the co-existence of the fluorescence for CAA366 (*red*) and GFP (*green*) in the same cell. (B) Representative GFP fluorescence images of HEK293T cells expressing GFP-tagged wild-type CaV2.1 channels in the presence of untagged EA2 mutants. Three representative midsection cell images are shown for each of the six co-expression conditions to exemplify the three localization patterns: membrane-dominant (*left panels*), cyto-membrane (*middle panels*), and cytoplasm-dominant (*right panels*). Scale bar = 10μm.

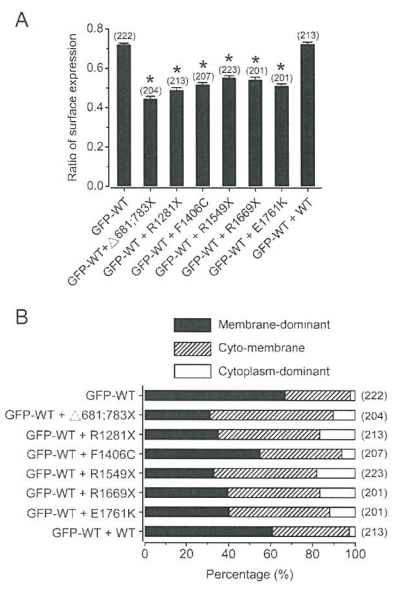

Figure 2. Quantitative analyses of the membrane localization of wild-type CaV2.1 channels in the presence of EA2 mutants. (A) Mean ratios of surface expression for GFP-tagged wild-type channels in the presence of different α1A constructs. (B) Cellular distribution percentages of the three localization patterns of GFP-tagged wild-type channels in the presence of different α1A constructs. The numbers in parentheses refer to the number of cells analyzed for each co-expression condition.

MORPHOLOGICAL CHANGS DURING SPONTANEOUS FUNCTIONAL RECOVERY AFTER SPINAL CORD INJURY

YANG, Cheng-Chang (楊正昌)[1]; LIN, Kwan-Hwa (林光華)[2]
and YU, Shang-Ming (游祥明)[3]

[1] Institute of Anatomy and Cell Biology, National Yang-Ming University, Taipei, Taiwan
[2] Graduate Institute of Physical Therapy, School of Physical Therapy, National Taiwan University, Taipei, Taiwan
[3] Department of Nursing, College of Nursing, Central Taiwan University of Science and Technology, Taichung, Taiwan

The adult mammalian CNS is vulnerable to various injuries or trauma. Spinal cord injury (SCI) results in ischemia and hypoxia followed by a series of degenerating events. Administration of growth factors leads to repair of blood vessels or replacement of neurons and oligodendrocytes in the injured spinal cord. The mechanism of the spontaneous locomotion recovery and regeneration of the spinal cord is still not elucidated at present. Adult male Sprague-Dawley rats (250-300g) were anesthetized with chloral hydrate (360 mg/Kg i.p.) and hemisectioned (left side) at T9 vertebral level. Animals were sacrificed at 6, 12 hours, 1, 4, 7, 14, 21, and 28 days after spinal cord injury. Animals were fixed in 6 % paraformaldehyde- lysine-periodate fixative and prepared for electron microscopy. At the electron microscopic level, one type of the neuron contained many small vacuoles (arrow) and a few large vacuoles in the spinal cord at 7 days after SCI (Fig. A). The large vacuoles showed double membrane-bound structures. A few ribosomes were found in the cytoplasm of the neuron. The other type of the neuron showed abundant ribosomes (arrows) and similar characteristic of small and large vacuoles (Fig. B). Another type of the neuron showed numerous holes (arrow) in the clumped chromatin in the nucleus (Fig. C). The fourth type of the neuron showed a large nucleolus and heterochromatinized materials in the nucleus (Fig. D). At higher magnification, there was a remarked increase in the ribosomes and the rough endoplasmic reticulum (arrow) in the cytoplasm Fig. E). The fifth type of the neuron showed an irregular apoptotic-like body (single arrow) in the nucleus and a slight dilatation of the rough endoplasmic reticulum. Bundles of collagen fibers (arrowhead) and axon-like structure (double arrows) were found in close contact with these neurons (Fig. F).

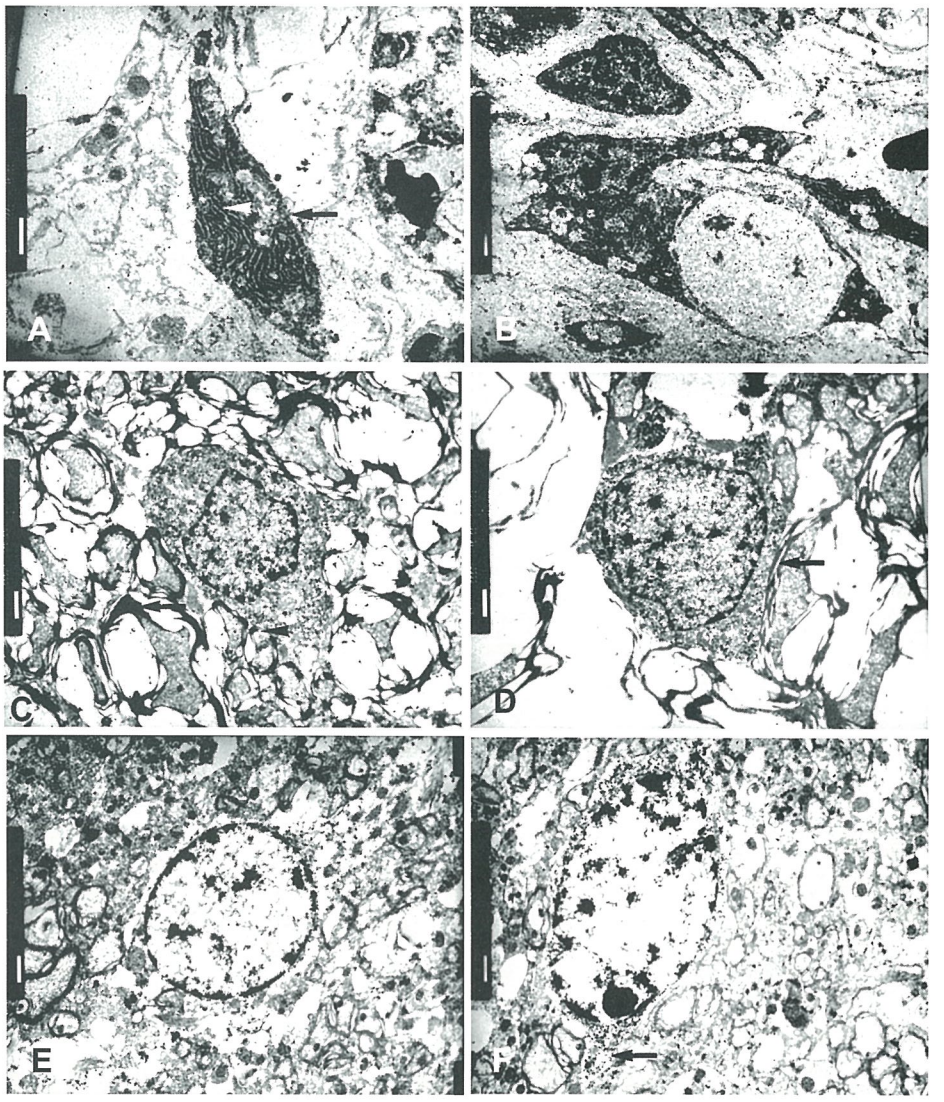
A
B
C
D
E
F

M-P-1 TEM IN
PARTICLES IN A

Kao, Fang-Hsi

Institute of Materials S
Taiwan.

There has recent
containing, high streng
where strength, tough
typical microstructure
However, the careful
nano-sized copper pa
significantly to the str
steels is still at the
precipitation of copper

Fe-0.06C-1.5Mn-
present investigation.
isothermal transformat
then rapidly cooled to
precipitates were form
about 15~25 nm. Whi
slowly, the newer ones
of those particles is alm
twins or some other
nucleation of precipita
instance precipitates gr
the grain boundary. Th
diffusion. Fig. 4 show
planar interphase precip
necessarily be formed
arranged on slightly cur
various treatment condi

References

1. R. A. Ricks, P. R. Ho
2. C. E. Williams and C

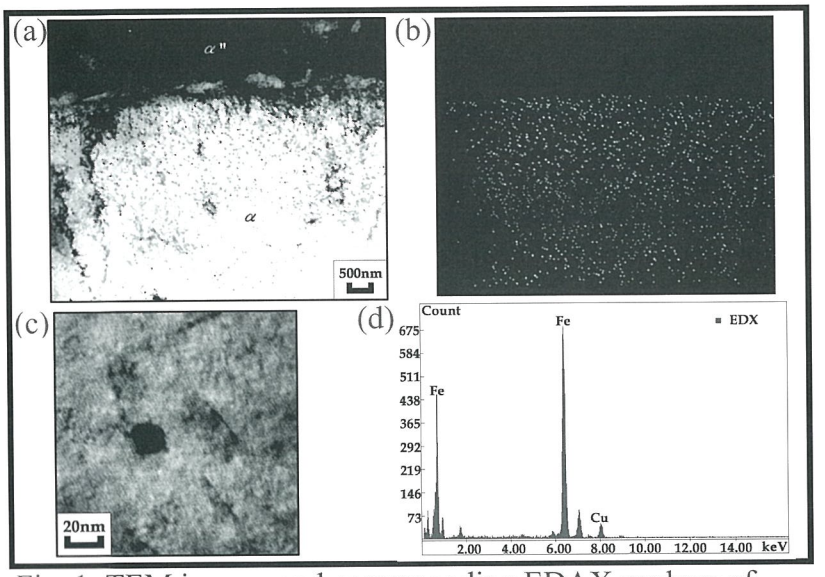

Fig. 1. TEM images and corresponding EDAX analyze of copper precipitates within ferrite; aged at 625℃ for 90 min.

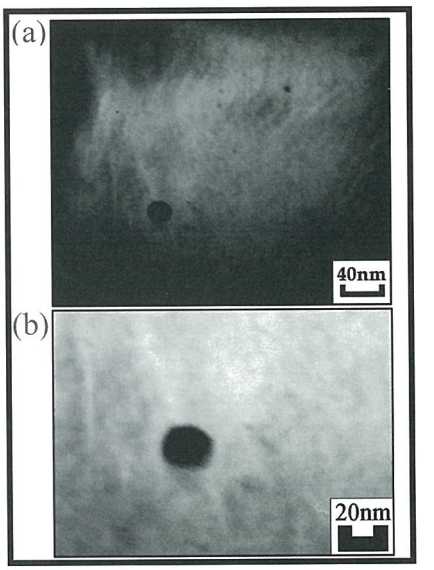

Fig. 2. TEM images of faults within copper precipitates.

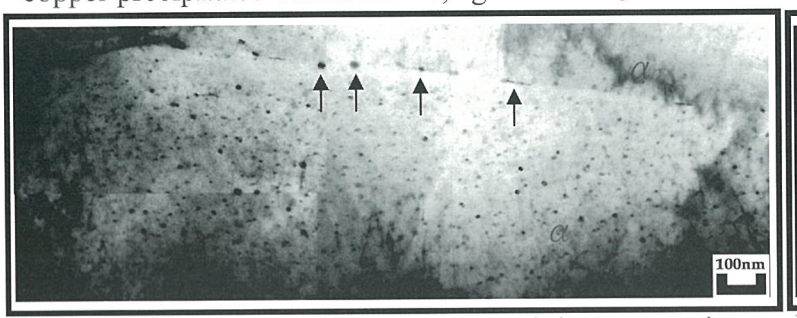

Fig. 3. TEM image showing copper precipitates at grain boundary ferrite/ferrite interphase boundary.

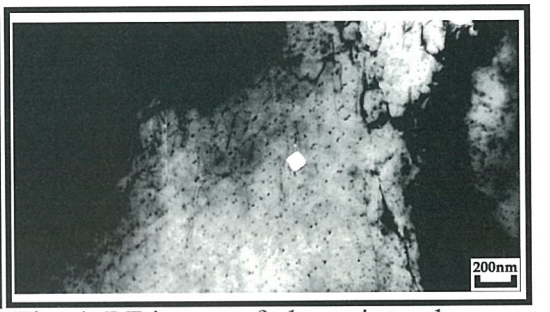

Fig. 4. BF image of planer interphase precipitates; aged at 635℃ for 30 min.

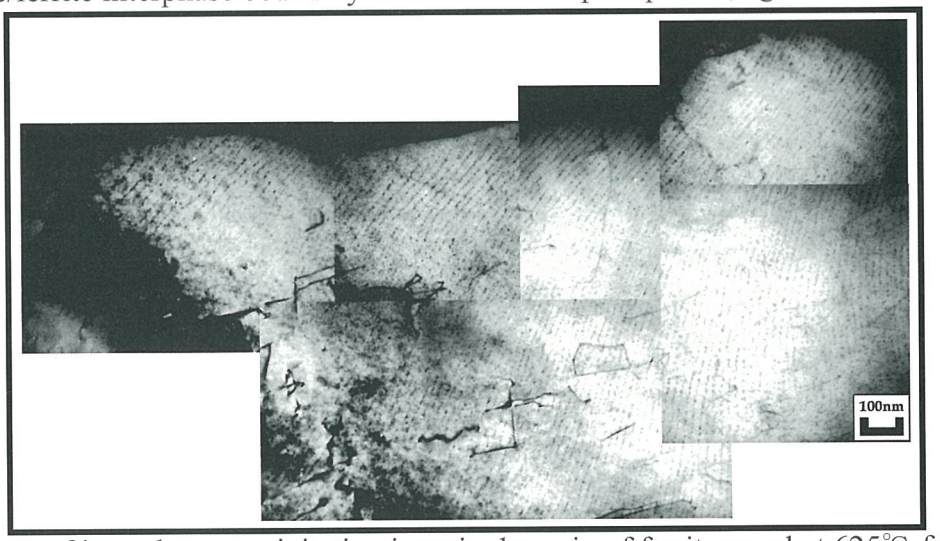

Fig. 5. BF image of interphase precipitation in a single grain of ferrite; aged at 625℃ for 90 min.

M-P-2 TAILOR-MODE THE SMALLEST AND LARGEST SINGLE WALL CARBON NAOTUBE BY *IN-SITU* TEM

CHANG, Yuan-Chih(張淵智)[1]; CHANG, Chia-Seng(張嘉升)[1]; LIAW, Yuan-Hong (廖原鴻)[1]; HUANG, Yang-Shan(黃仰山)[1]; HSU, Tung(徐統)[2] and TSONG, Tien-Tzou(鄭天佐)[1]

[1] Institute of Physics, Academia Sinica, Nankang, Taipei, Taiwan, ROC
[2] Department of Materials Science and Engineering, National Tsing-Hua University, Hsinchu, Taiwan, ROC

Single wall carbon nanotubes (SWNTs) are widely investigated for their excellent properties and are finding promising applications in nano/bio-technology such as nano-electronics, SPM probe, field emission tip, and fuel cell, to name just a few. In this report we present our results on *in-situ* growth and manipulation of a single MWNT. With growth, we produced the smallest SWNT as shown in Fig. 1; with inner shell extraction, we fabricated a SWNT of the largest diameter as shown in Fig. 2. The experiment was performed in an ultra-high vacuum transmission electron microscopy (UHV-TEM, JEOL JEM-2000V) configured with a home made STM riding on a nanopositioning system. The nanopositioning system provided coarse mechanical motions in three dimensions and the fine adjustments were performed with the piezo tube scanner.

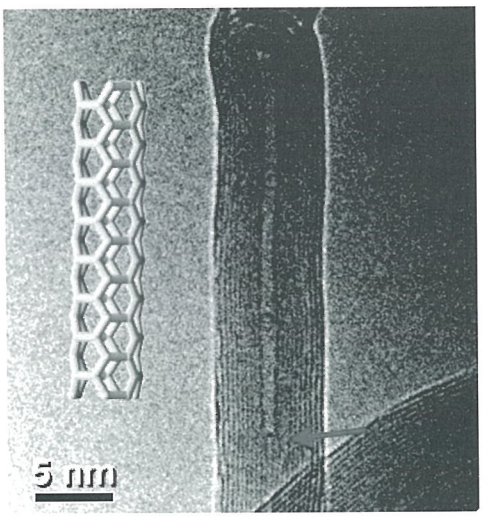

Fig. 1. Transmission electron micrograph shows the smallest SWNT formation. The smallest SWNT is arrowed. Schematic drawing is accompanied to illustrate the smallest SWNT.

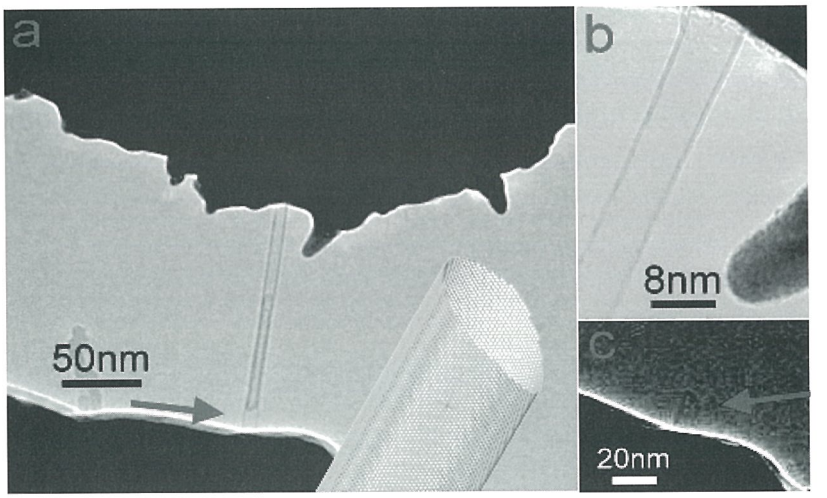

Fig. 2. Transmission electron micrographs show the largest MWNT fabrication at last stage of the extraction process. Schematic drawing is accompanied to illustrate the largest SWNT. (a) The SWNT formation (see arrow) during second internal peeling process. (b) A two-wall tube pulled out after the second peeling process. (c) The remaining SWNT on the base (see arrow) obtained by two internal peeling processes.

M-P-3 ELECTRICAL PROPERTIES MEASUREMENT FLUORINE-DOPED SnO_2 NANOWIRES WITH IN-SITU STM/TEM TECHNIQUE

TSAI, Feng-Yin(蔡豐印)；KAI, Ji-Jung(開執中) and CHEN, Fu-Rong(陳福榮)

Center of Electron Microscopy, Department of Engineering and System Science, National Tsing Hua University, Hsinchu 300, Taiwan

Transparent conductive oxides (TCO) ,such as SnO_2, In_2O_3, CdO, and ZnO, have become increasingly important in a large variety of applications due to demands for optically-transparent, conductive materials.[1-2] To enhance the conductivity, we usually dope suitable atoms introduce more free carriers.[3] It has been widely used as electric leads in optoelectronic devices such as flat panel displays and thin film solar energy cells.

A common TCO used in research and industry is tin-doped indium oxide (ITO). However, ITO experiences a reduction of electrical conductivity when exposed to oxygen at elevated temperatures (> 300 ℃). Therefore, FTO, which is much more thermally stable, is often used as an alternative to ITO. As device size continues to decrease, the potential use of nanoscaled structures of these TCOs grows. However, very little to no work has been published regarding the fabrication of FTO nanowires.[4]

The authors report the growth of F-doped SnO_2 single crystalline nanowires by carrying out the thermal evaporation of solid Sn and SnF_2 powders a in an Ar/O_2 ambient gas. We analyzed the samples with scanning electron microscopy (Fig.1), X-ray diffraction (Fig.2), transmission electron microscopy (Fig.3). From the EDS spectra (Fig.4), we can quantify fluorine-doping in the nanowires is about 2 at%. The electrical properties of rutile-type F-doped SnO_2 low-dimensional structures were analysed using a scanning tunnelling microscopy (STM) in situ holder for transmission electron microscopes (TEM).The measured I-V curve (Fig.5) obtained typically show Ohmic-like behavior between the gold electrode and F-doped SnO_2 nanowires. And the resistivity of FTO NWs is 0.0278Ω-cm, much smaller than pure SnO_2 NWs(289 Ω-cm).

References

[1] Hyoun Woo Kim and Seung Hyun Shim, Journal of the Korean Physical Society, Vol. 47, No. 3, (2005), pp. 516~519

[2] F Hern´andez-Ram´ırez et al, Nanotechnology 17 (2006) 5577–5583

[3] Jin Huang, Aixia Lu, Bin Zhao, and Qing Wan, APPLIED PHYSICS LETTERS 91, 073102 (2007)

[4] B. Russo and G.Z. Cao, Appl. Phys. A 90, 311–315 (2008)

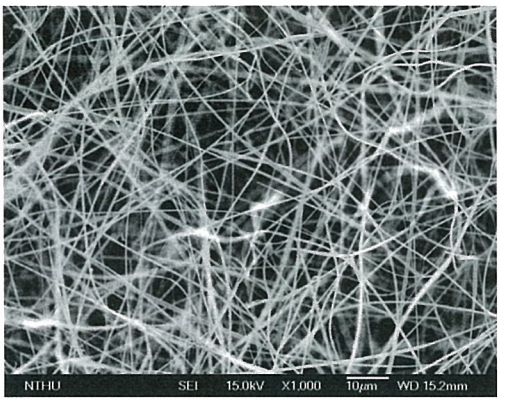

Figure 1. SEM image of FTO nanowires.

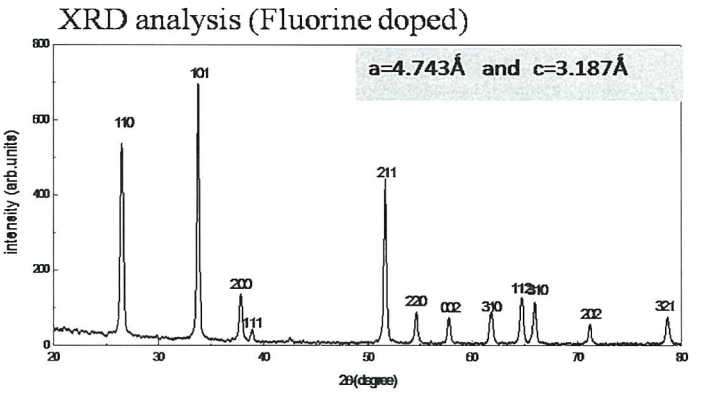

Figure 2. XRD pattern of FTO nanowires.

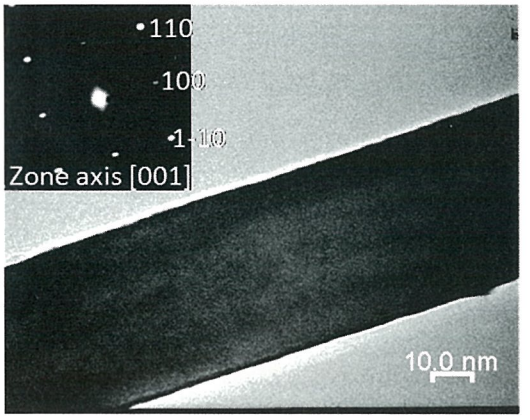

Figure 3a. TEM image of a single crystalline FTO nanowire. The inset shows SAED pattern of the [001] zone axis.

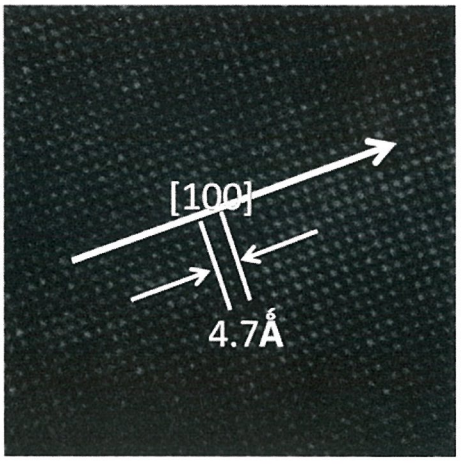

Figure 3b. HRTEM image.

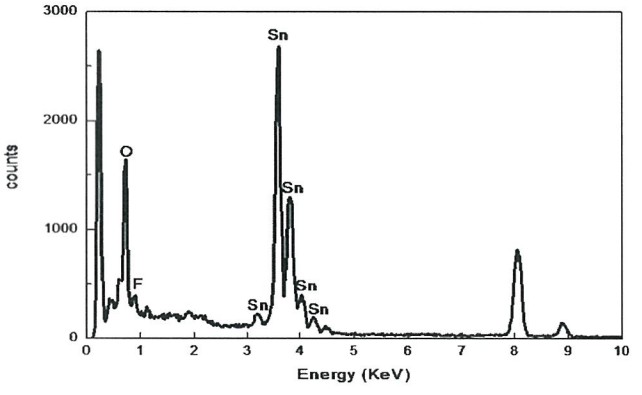

Figure 4. EDS spectra of FTO NWs.

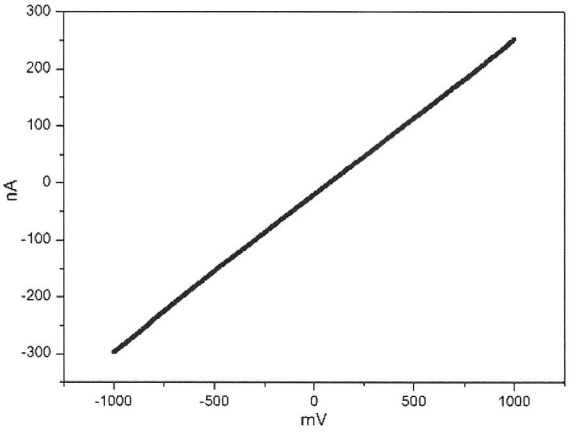

Figure 5. Two-probe *I –V* curve of a single FTO NW by TEM-STM. The inset (upper) shows the I-V curve of a single undoped SnO_2 NW. The other inset (lower) shows the TEM image that gold tip contact with a NW.

M-P-4 BULK AND SURFACE ELECTIONIC EXCITATION IN HfO_2/GaAs (001) HETEROSTRUCTURES BY STEM-EELS

LIOU, Sz-Chian(劉思謙)*, CHU, Ming-Wen(朱明文),* CHEN, Cheng-Hsuan(陳正弦),* LEE, Y. J.(李毅君),** HONG, Ming-Hwei(洪銘輝),** and KWO, Ray-Nien(郭瑞年)***

*Center for Condensed Matter Sciences, National Taiwan University, Taipei, Taiwan
**Department of Materials Science and Engineering, National Tsing Hua University, Hsinchu, Taiwan
***Department of Physics, National Tsing Hua University, Hsinchu, Taiwan

HfO_2 with its high dielectric constant (κ~ 18-25) and large band gap (5.68 eV) is a strong candidate material for effective passivation of the GaAs substrate in metal-oxide-semiconductor field-effect transistors (MOSFETs) [1]. The interface and microstructure of such a HfO_2/GaAs(001) heterostructure have been thoroughly investigated in our previous study [2], while little has been reported about the electronic characterization of this material system. Here, we studied the electronic excitations of HfO_2 films (5 nm in thickness) on GaAs(001) by the conjunction of scanning transmission electron microscopy (STEM) and electron energy-loss spectroscopy (EELS), STEM-EELS, with a 0.2-nm electron probe that determines also the spatial resolution of this technique.

Figure 1a shows a high-angle annular dark filed (HAADF) image of the epitaxial HfO_2 films, revealing an atomically sharp interface between the film and substrate. The formation of amorphous interfacial oxide layers can be excluded accordingly. Figure 1b shows the zero-loss-peak-deconvoluted STEM-EELS spectra of HfO_2 acquired at the different positions indicated in Fig. 1a. Positioning the probe at the bulk of the film (position 4), we observed several broad spectral features above the optical band gap at ~6, ~16, ~28.5, ~35, and ~39 eV, and these peak positions are consistent with the literature report [3]. However, the physical natures of these excitations have never been documented before.

Indeed, the experimental EELS spectra can be satisfactorily understood in the framework of the macroscopic dielectric theory for EELS excitations provided the complex dielectric function of the material is known. Performing Kramers-Krönig analysis on the spectrum #4 in Fig. 1b, the complex dielectric function of the HfO_2 film was derived, Fig. 2. At ~16 eV, the zero ε_1 and vanishing ε_2 (Fig. 2) characteristic to the bulk-plasmon excitation clearly indicate this physical nature to the 16-eV excitation. Moving the probe position from #4 toward the surface #1, the intensity for the bulk-plasmon excitation significantly reduces, while the peak at ~13.5 eV is visibly enhanced, indicating its surface-plasmon nature manifested by a negative ε_1 in the corresponding energy regime (Fig. 2). The peaks at ~6, ~28.5, ~35, and ~39 eV showing

rather sharp o
interband tran
the 6-eV peak
~35-, and ~39
toward #1. T
excitation cha
sharp excitoni
unexpected phe

References

[1] Hong, M., I
(**283**)1897.
[2] Liou, S. C.
and Kwo, J.
Appl. Phys
[3] Frandon, J.,

Figure 1 (a) The S
projection. (b) Th

Figure 2 The com

M-P-5 EXCITATIONS OF SURFACE POLARITONS IN NANO-MATERIALS BY STEM-EELS

Chien-Ting Wu(吳建霆)[a], Chun-Wei Chen(陳俊維)[a], Kuei-Hsien Chen(陳貴賢)[b], Li-Chyong Chen(林麗瓊)[c], Ming-Wen Chu(朱明文)[c], Cheng Hsuan Chen(陳正弦)[c]

[a]Dept. of Materials Science and Engineering, National Taiwan University, Taiwan
[b]Institute of Atomic and Molecular Sciences, Academia Sinica, Taipei, Taiwan
[c]Center for Condensed Matter Sciences, National Taiwan University, Taiwan

Bulk and surface excitations of triangular GaN nanorods were investigated by the conjugation of scanning transmission electron microscopy (STEM) and electron energy-loss spectroscopy (EELS), STEM-EELS. With the 0.2-nm electron probe in STEM-EELS, the excitation of surface polaritons can be thoroughly explored by brining the atomic-scale probe near the surface of nanomaterials in grazing incidence. Modern nanomaterials thus provide new opportunities for studying surface excitations.

Figure 1a shows the typical high angle annular dark field STEM image of the GaN nanorod. The impact parameter dependent STEM-EELS spectra of the nanorod are exhibited in Figure 1b with the electron probe position ranging from impinging the bulk of the nanorod to grazing at a finite distance from the planar surface of the nanomaterial. These STEM-EELS studies show that the predominant excitations at ~19 and ~14.5 eV arise from the respective resonances of bulk and surface plasmons (SP). In addition, the SP peak intensity was found to decay exponentially with the increase in impact parameters, e.g., from 0 to 20 nm away from the planar surface. Unexpectedly, we observed several peaks with the characteristics of surface exciton polaritons [1] (SEP) occurring near interband transitions in the spectral regime below the SP. The positions of these peaks correlate well with peaks in the imaginary part of the complex dielectric function of GaN, signifying their excitonic characters [1]. We also note that the wave fields of these SEP-like excitations are most prominent outside the nanorod surface as characteristic to SPs, while their wave-field exponential decays are much slower compared to SPs.

References

[1] Fuzi Yang, J. R. Sambles, and G. W. Bradberry, PRL, 64, 559–562 (1990).
[2] Acknowledgement: This work was financially supported by the National Science Council, Taiwan.

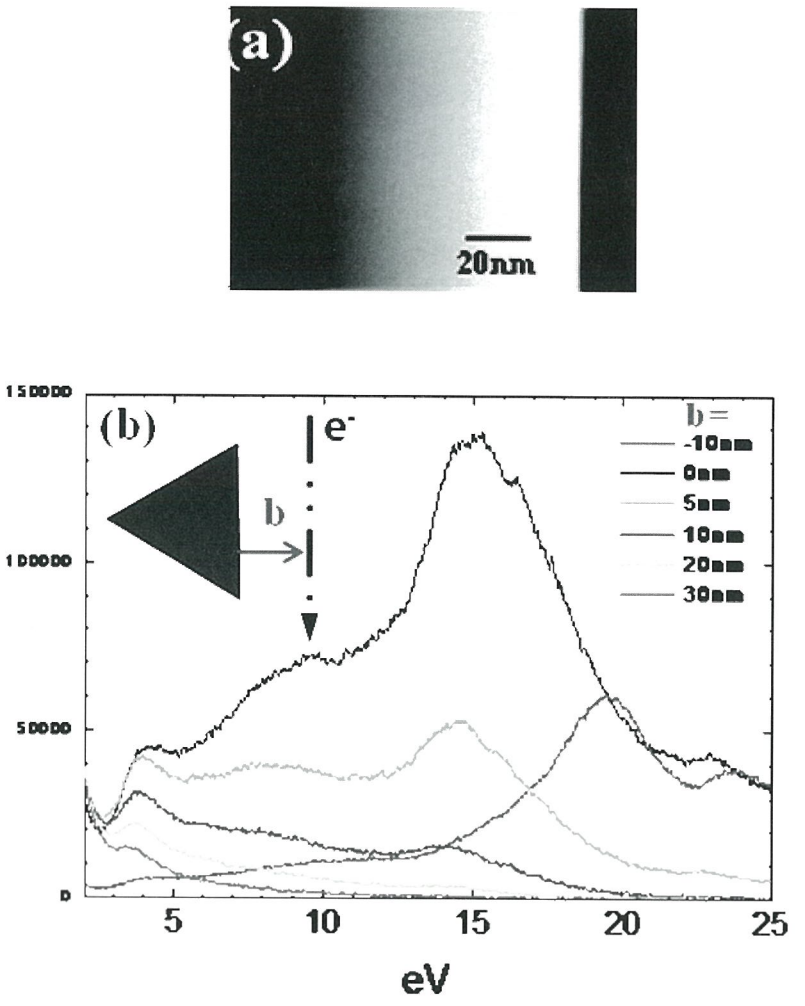

Figure 1. (a) The STEM HAADF image of a triangular GaN nanorod and (b) the impact parameter dependent STEM-EELS spectra of this nanomaterial. Inset, the scheme for the impact parameter.

M-P-6 CRYSTALLOGRAPHIC AND LOCAL ELECTRONIC STRUCTURES OF NANOCHECKERBOARDS IN MN-DOPED COBALT FERRITE

TSENG, Chuan-Ming[a] (曾傳銘), ZHANG, Chenglin[b], YEO, Sunmog[b], CHEONG, Sang-Wook[b], CHU, Ming-Wen[a] (朱明文) and CHEN, Cheng-Hsuan[a] (陳正弦)

[a]Center for Condensed Matter Science, National Taiwan University, Taipei 10607, Taiwan.
[b]Rutgers Center for Emergent Materials and Department of Physics & Astronomy, Rutgers University, Piscataway, New Jersey 08854, USA

Recently, solid-state self-assembly of nanocheckerboards (CB) in Jahn-Teller cations (Mn^{3+}) containing spinel systems was successfully achieved via chemical phase separation mediated by cooperative Jahn-Teller distortions [1,2]. More interestingly, the CBs are mainly stacked with two constituent domains, one is cubic domain with lower Mn concentration and the other is tetragonal domain with higher Mn concentration. In this study, we present the crystallographic and electron energy-loss near-edge structures (ELNES) of these two distinct phases in Mn-doped $CoFe_2O_4$ spinel by using high resolution transmission electron microscopy (HRTEM) and high resolution electron energy loss spectroscopy (EELS).

Fig. 1a and its inset are HRTEM lattice image and the corresponding electron diffraction of CB domain of $Co_{0.6}Fe_{0.9}Mn_{1.5}O_4$ spinel. The CB pattern is found to be an intriguing patchwork of four different types of domains denoted as α, β, γ, and δ. It is noted that α and γ domains are tetragonal (more accurately, orthorhombic) whereas β and δ are cubic. A schematic rendition which clearly shows the intricate arrangement of the four different types of domains is displayed in Fig. 1b. Herein, the lattice constants are estimated from the positions of the diffraction peaks.

The ELNES results reveal that the O *K*-edge, Mn and Fe *L*-edge spectra are much different between these two types of domains, and the Co *L*-edge, however, stays unchanged. Fig. 2 shows the ELNES (O *K*-edge, Mn and Fe *L*-edge) of two constituent domains and parent compounds, $CoMn_2O_4$ and $CoFe_2O_4$. Clearly, the shape and position of characteristic peaks in Mn-rich and Fe-rich domain are similar to $CoMn_2O_4$ and $CoFe_2O_4$, respectively. For the O *K*-edge, three fine-structured peaks around 530eV can be found in Mn-rich domain and $CoMn_2O_4$ as shown in Fig.2a. It's noted that the O *K*-edge ELNES is mainly attributed to the transitions from *1s* core states to oxygen *2p* state hybridized with cations' *3d* orbitals. The presence of Jahn-Teller distortions in the Mn-rich domains is believed to play important roles in the appearance of oxygen *K*-edge fine structures.

References

1. S. Yeo, Y. Horibe, S. Mori, C. M. Tseng, C. H. Chen, A. G. Khachaturyan, C. L. Zhang and S. -W. Cheong, App.Phys.Lett. **89,** 233120 (2006).
2. C. L. Zhang, C. M. Tseng, C. H. Chen, S. Yeo, Y. J. Choi and S. -W. Cheong, App.Phys.Lett. **91,** 233110 (2007).

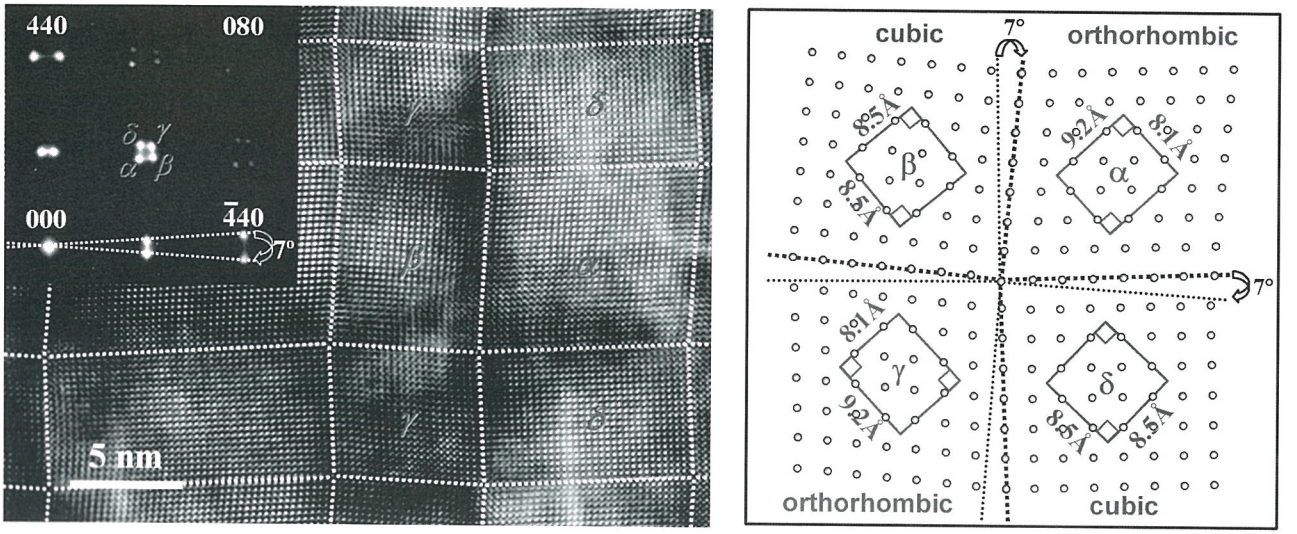

Fig.1. (a) High-resolution TEM image of checkerboard in $Co_{0.6}Fe_{0.9}Mn_{1.5}O_4$ spinel. The checkerboard domain consists of four distinct domains, denoted as α, β, γ, and δ. The β and δ are cubic and α and γ appear to tetragonal. The inset is the diffraction pattern of checkerboard domains and the dashed lines with arrow indicate the rotations of the two cubic domains. (b) Schematic view of how the four domains constitute a checkerboard domain.

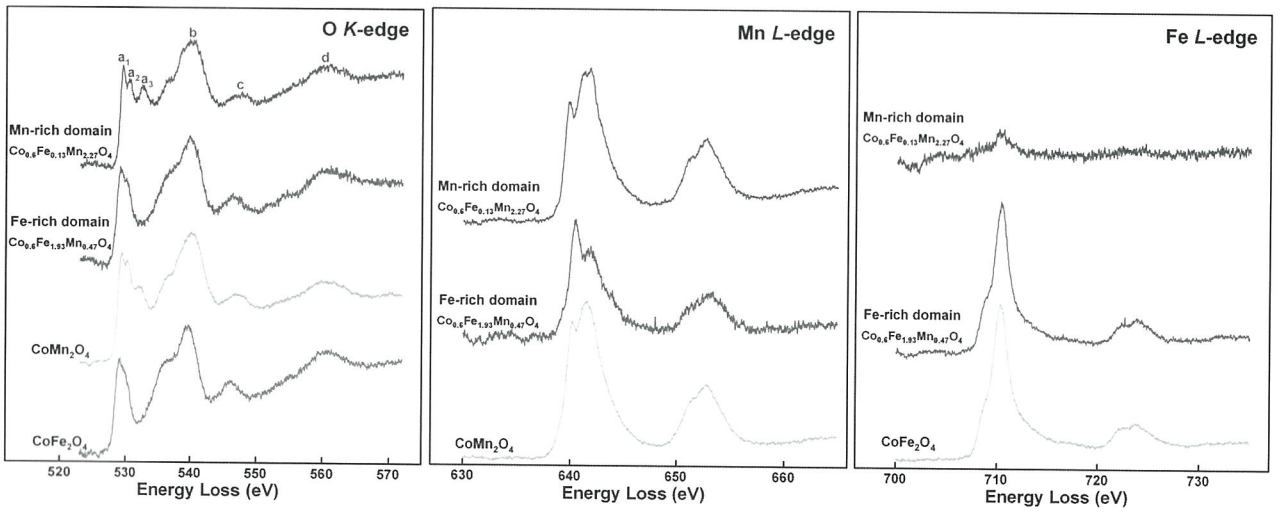

Fig.2. Electron energy loss near-edge spectrum (ELNES) after background subtraction: (a) Oxygen *K*-edge, (b) Manganese *L*-edge, and (c) Iron *L*-edge.

M-P-7 MEASUREMENTS OF RESONANCE FREQUENCY SHIFT DEPENDING ON THE ADSORPTION POSITION OF A SILVER CLUSTER ON A CARBON NANOTUBE

Wang, Shau-Chieh(王少傑);[a.b] Chang, Yaun-Chih（張淵智）;[b]Lien, Dir-Hsien（連德軒）;[b] Hsu, Tung（徐統）;[a*] Chang, Chia-Seng（張嘉升）[b*] and Tsong, Tien-Tzou（鄭天佐）b[2]

[a]Department of Materials Science and Engineering , National Tsing Hua University, Hsinchu, Taiwan

[b]Institute of Physics, Academia Sinica, Nankang, Taipei, Taiwan

It is very important to detect a minute mass in many fields, such as physical, chemical, biochemical sciences [1-3]. One of the methods to measure minute mass is using cantilever-based resonators. The method's basic principle is to measure the mass sensor's resonance frequency shift subjected to the attached mass and then translate the measurement into mass [4]. In this study, we investigated the effect of the position of added mass experimentally with *in situ* transmission electron microscopy and compared the experiment results with finite element method simulation and analytical expression. This experiment used multi-walled carbon nanotubes (MWNTs) as cantilevers (Fig. 1). The frequency shift with an attached silver nanoparticle was measured as a function of the nanoparticle positions. The mass sensitivity in this experiments is about 10^{-18} g. In summary, we have determined the relation of particle positions and mass response in nanoscale, and have demonstrated the attached nanoparticle mass sensitivity at the attogram scale.

This work was supported by the National Program for Nanoscience and Technology managed by the National Science Council of Taiwan under Grant No: NSC96-2120-M-001-006.

References

1. Benes, E.; Groschl, M.; Burger, W. and Schmid, M. Sens. Actuators, A 1995 (48) 1.
2. Thundat, T.; Oden, P. I. and Warmack, R. J. Microscale Thermophys. Eng. 1997 (1) 185.
3. Hauptmann,P.; Lucklum, R.; Puttmer, A. and Henning, B. Sens. Actuators, A 1998 (67) 32.
4. Poncharal, P.; Wang, Z. L.; Ugarte, D. and de Heer, W. A. Science 1999 (283) 1513.

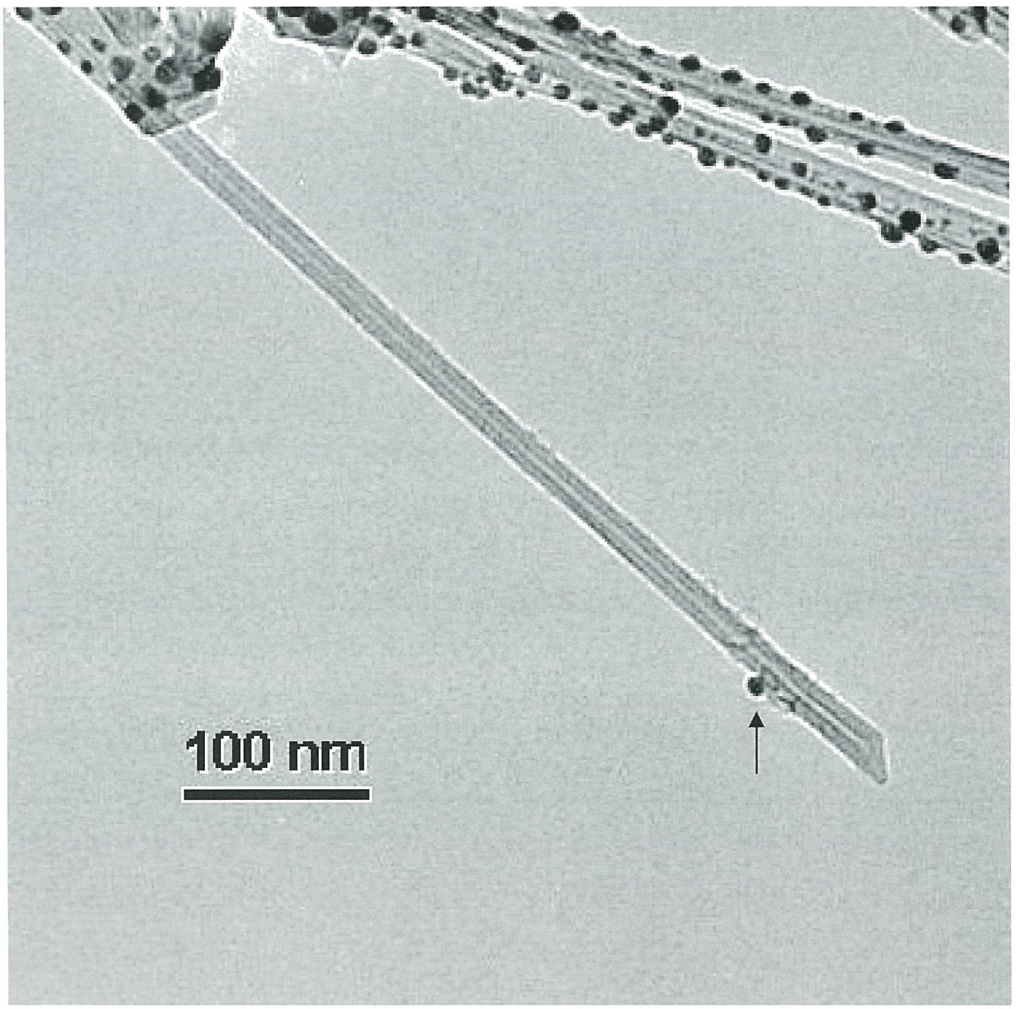

Fig. 1. The transmission electron micrograph of an Ag nanoparticle (arrow) placed on a MWNT.

M-P-8 MICROARC OXIDATION AND HYDROTHERMAL TREATMENT OF BIOMEDICAL Ti-30Nb-1Fe-1Hf ALLOY

* OU, Shih-Fu(歐士輔)[a]；LIN, Chao-Sung(林招松)[b] and PAN, Yung-Ning(潘永寧)[a]
[a] Department of Mechanical Engineering, National Taiwan University, Taipei, Taiwan
[b] Department of Materials Science and Engineering, National Taiwan University
, Taipei, Taiwan

Among all the biomedical material in use, cp.Ti is widely used in bone implant for its light mass, corrosion resistance, durability, high strength and nice biocompatibility. According to previous researches, Young's modulus (106GPa) of cp.Ti is largely higher than that of the bone (10~30GPa). Thus the tress shielding effect will arouse bone atrophy which leads to implant looseness [1-2]. The purpose of this study is to form a hydroxyapatite (HA) coating on the low Young's modulus (62GPa) Ti-30Nb-1Fe-1Hf alloy [3] by microarc oxidation(MAO) and hydrothermal treatment [4].

MAO was performed on Ti-Nb alloy in an electrolyte containing 0.04mol/l beta-glycerophosphate disodium (β-GP) and 0.2mol/l calcium acetate (CA) using a regulated DC power supply at a current density of 50 mA/cm^2. After the microarc oxidation, the samples were placed at the bottom of an autoclave, in which 20 ml of water solution whose pH was adjusted to 9.0–13.0 by adding NaOH, and then the samples were hydrothermally treated at 250°C for 6h. The morphology of the HA crystals was observed by SEM. The structures of anodic oxides were analyzed by XRD and XPS. The compositions of the oxide films were semi-quantitatively analyzed by EPMA.

After MAO, there is a porous oxide film on the sample. The sizes of micropores (Fig. 1.), and the quantity of Ca and P (Table. 1.) tend to increase with increasing applied voltage. When the voltage increases to 300V, the Ca/P is 1.72, which is close to the Ca/P(1.67) of HA. This oxide film is composed of Anatase TiO_2, and it transforms to amorphous phase as applied voltage to 300V (Fig. 3). According to XPS identification, this film contains TiO_2, Nb_2O_5, CaO, $Ca(OH)_2$ and $Ca_2P_2O_7$. HA crystals were precipitated on the film surface after hydrothermal treatment at 250°C for 6 h (Fig. 4), and the amount of HA precipitated increased with increasing pH of water solution. According to the XRD identification, high temperature and high pressure cause the formation of a small amount of tricalcium phosphate (TCP) (Fig. 3) and enhance the oxide film's crystallinity.

References

1. B. Van Rietbergen, R. Huiskes and H.Weinans J. Biomechanics, 1993(26), 369.
2. H. Weinans, R. Huiskes and B. Van Rietbergen J. Orthopaed. Res., 1993 (11), 500.
3. Y.H. Hon, J.Y. Wang and Y.N. Pan Materials Letters, 2004 (58) 3182.
4. H. Ishizawa and M. Ogino. J. Biomed. Meter. Res., 1995(29) 1071.

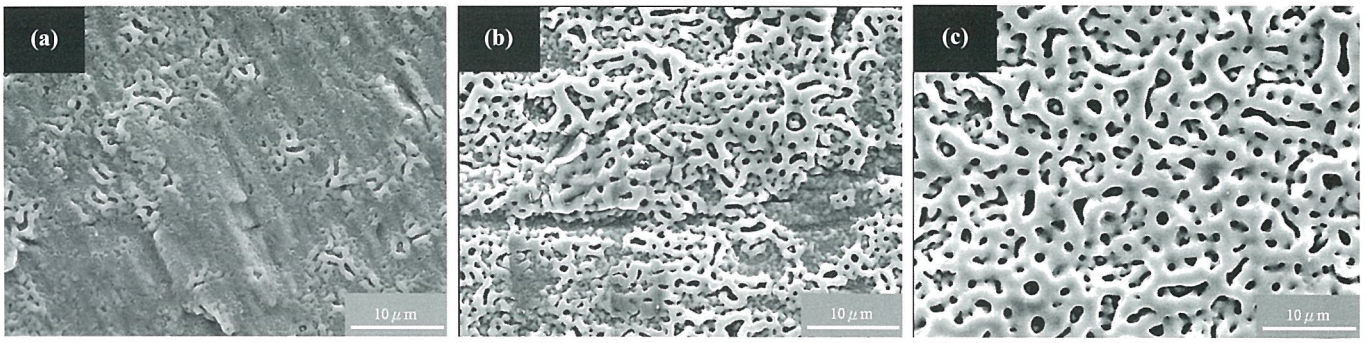

Fig. 1. Morphologies of anodic oxide films of Ti-Nb alloy at 50 mA/cm^2: (a) 100V; (b) 200V; (c) 300V

Table. 1. Parameters of anodic oxidation and oxide films of Ti-Nb alloy

Applied voltage	Ti	Nb	O	Ca	P	Ca/P
200V	17.65	3.83	68.89	4.64	4.73	0.98
300V	12.65	2.82	70.51	8.77	5.10	1.72

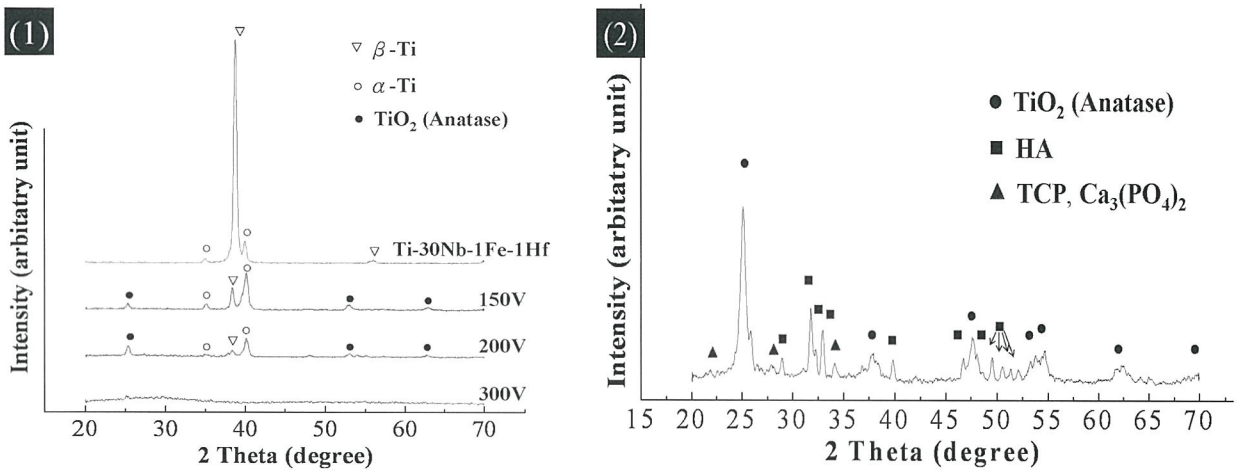

Fig. 3. XRD patterns of anodic oxide films (1) before hydrothermal treatment; (2) after hydrothermal treatment at 250°C for 6 h with water solution pH 9.0

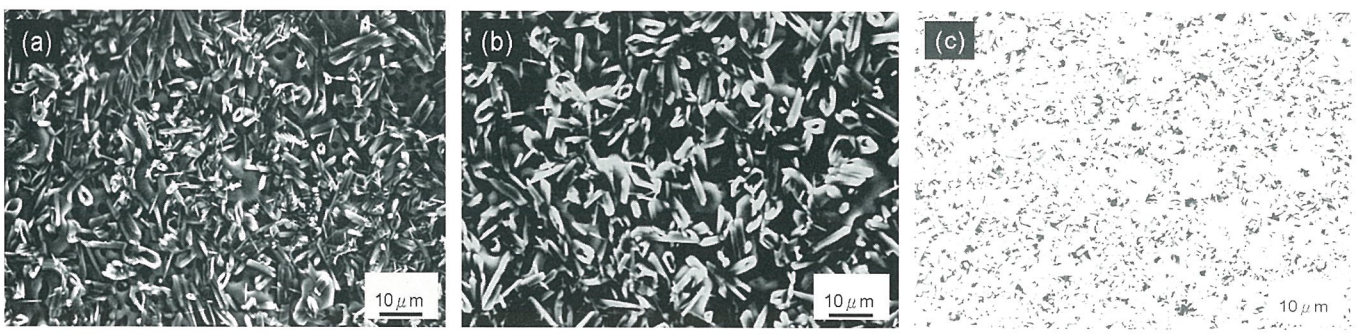

Fig. 4. Morphologies of oxide films treated hydrothermally at 250℃ for 6 h : (a) pH7; (b) pH9; (c) pH13

M-P-9 TEM CHARACTERIZATION OF GADOLINIUM NANOCRYSTAL MICROSTRUCTURE FOR MEMORY DEVICES

Michael R. S. Huang (黃榮喜)[a]；Chuan-Pu Liu (劉全璞)[a]；Yu Kai Chen (陳育楷)[b]；Chao Sung Lai (賴朝松)[b]; and Li Hsu (徐立)[c]

[a]Department of Materials Science and Engineering, National Cheng Kung University, Tainan, Taiwan

[b]Department of Electronics Engineering, Chang Gung University, Taoyuan, Taiwan

[c]Materials & Electro-Optics Research Division, Chung-Shan Institute of Science & Technology, Tao-Yuan, Taiwan

Recently nanocrystal (NC) memory device, composing of discrete charge storage dots, has attracted much research interest since it is considered the promising candidate to replace conventional floating-gate (FG) memory device [1,2]. However, controlling dot density, size uniformity and distribution is the most challenging task in fabrication. These parameters will greatly affect device properties and performance.

In this study, Gadolinium (Gd) NC memory devices are characterized with transmission electron microscopy (TEM) to realize the relationship between the electric property and microstructure. The effect of rapid thermal annealing (RTA) on Gd nanocrystal formation in the gadolinium oxide (Gd2O3) layer is explored through evaluating the dot size, density and distribution under different thermal treatment conditions.

Fig.1. illustrates the device structure. The nomenclature of the specimens with experimental conditions is list in Table 1. In the beginning, a tunneling oxide layer was grown on N-type Si (100) in the furnace. About a 20 nm Gd_2O_3 wetting layer was then deposited by RF sputtering, and RTA was conducted subsequently at various temperatures in N_2 ambient. Eventually blocking oxide was capped on the top of the device by chemical vapor deposition.

According to previous capacitance-voltage (C-V) hysteresis measurements, the samples of P1 and P2 demonstrate considerable memory effect compared with P0 and P3. Through TEM plan-view observation (Fig.2), P1 and P2 show very high density of nanocrystals (Table 1). P2 has relatively larger amount of nanocrystals, which result in a greater memory window than P1. The diffraction ring pattern acquired from sample P2 (Fig.3) indicates Gd nanocrystals embedded in an oxide matrix behaving as charge storage units, which will possess better charge confinement effect and reduce the possibility of current leakage. For the samples of P1 and P2, containing adequate sum of storage dots, up to 5.8 ~ 9.1 x 10^{11} cm^{-2}, can promise great potential for device application in the future.

Ultimately the formation of Gd nanocrystals in a Gd_2O_3 layer during annealing process is still under investigation and further study is required to clarify the mechanism.

References

1. S. Tiwari, F. Rana, H. Hartstein, E. F. Crabbe, and K. Chan *Appl. Phys. Lett.* 68 (1996) 1377.
2. IIgweon Kim, Sangyeon Han, Kwangseok Han, Jongho Lee and Hyungcheol Shin *IEEE Electron Device Letter* 20(1999)1630.

Fig. 1 Scheme of memory device structure.

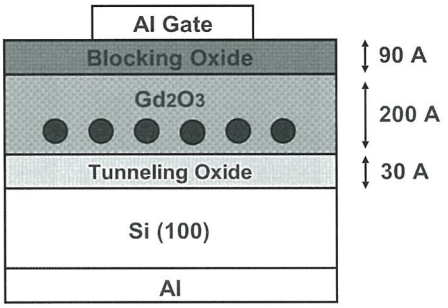

Table 1 Samples numbers, experimental conditions and results.

	RTA Temp (°C)	Memory Window (V)	NC Density (10^{11}/cm^2)
P0	950	0.8	3.9 – 3.2
P1	900	3.2	6.4 – 5.8
P2	850	3.7	9.1 – 7.9
P3	800	1.2	0.46 – 0.61

Fig. 2 TEM plane view observations

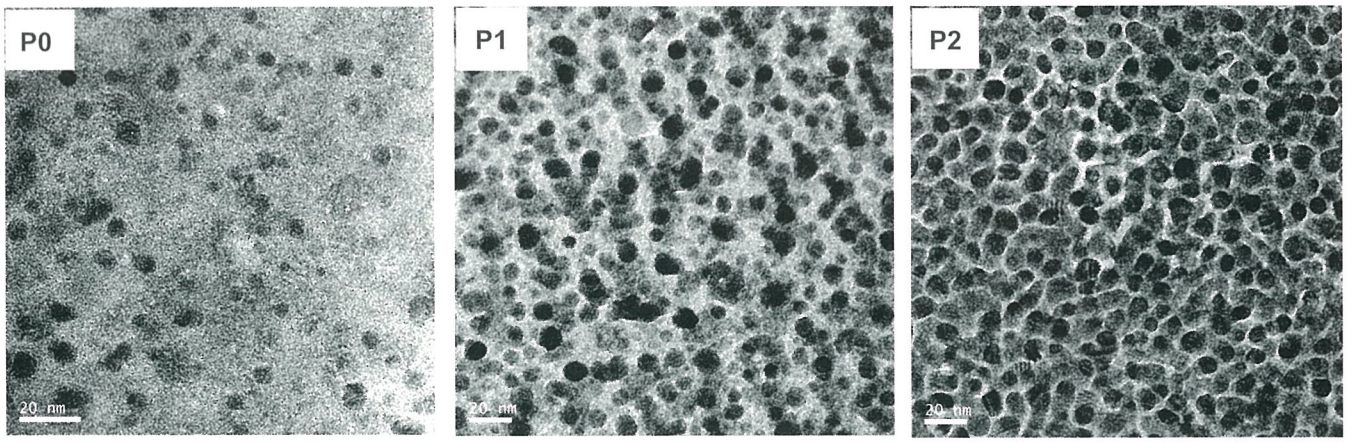

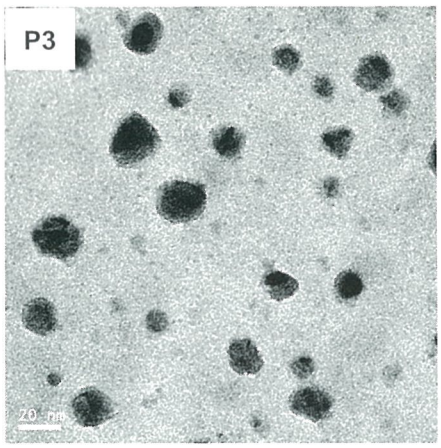

Fig. 3 Diffraction ring pattern of sample P2

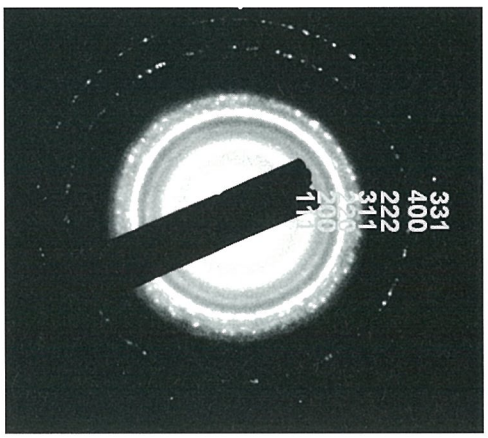

M-P-10 $\{10\bar{1}1\}$ AND $\{11\bar{2}1\}$-SPECIFIC GROWTH AND TWINNING OF ZnO WHISKERS

HUANG, Bang-Hao(黃邦浩)[1], CHEN, Shuei-Yuan(陳水源)[2]
and SHEN, Pouyan(沈博彥)[1]

Institute of Materials Science and Engineering, National Sun Yat-sen University, Kaohsiung, Taiwan.[1]

Department of Mechanical Engineering, I-Shou University, Kaohsiung, Taiwan.[2]

Vapor-liquid-solid (VLS) mechanism of single crystal growth [1] is a well-established process in catalyst-free [2] or catalyst-guided [3] growth of wurtzite-type (W) ZnO nanowires/nanobelts having polar surfaces (0001) and $(0\bar{1}11)$ to minimize the electrostatic energy [4]. Here we report further unusual ZnO whiskers with special habit and twinning via a self-catalyzed VLS growth from the W-ZnO/Zn deposit with a unique preferred orientation $\{10\bar{1}1\}_{W\text{-}ZnO}$ and $(0001)_{Zn}$. To obtain such deposit, Zn target was subjected to pulsed laser (Nd-YAG) irradiation under vacuum (3 $x10^{-5}$ torr) with tramp oxygen from target and/or chamber. Soda-lime glass slide was used to collect the condensates and then fired at 600°C to form W-ZnO whiskers for scanning electron microscopic (SEM, JEOL 6330, 10 kV) and transmission electron microscopic (TEM, FEI Tecnai G2 F20 at 200 kV) observations coupled with selected area electron diffraction (SAED) and point-count energy dispersive X-ray (EDX) analysis.

The rod-like W-ZnO whiskers turned out to develop in random orientation from the areas around the impact craters when the deposits on glass were annealed in air as indicated by the SEM images compiled in FIG. 1. TEM and EDX observations further indicated that the individual W-ZnO whiskers have negligible impurities and extend along the zone axis of the well-developed polar surfaces $\{10\bar{1}1\}$ for a beneficial lower electrostatic energy and surface energy (FIG. 2). Alternatively, the whiskers extend via $\{11\bar{2}1\}$-specific growth twinning and/or coalescence twinning (FIG. 3) for a beneficial fair coincidence-site lattice at the twin boundary as indicated by a schematic drawing showing the unrelaxed oxygen positions of the attached planes (FIG. 4).

References

1. Wagner, R. S. and Ellis, W. C. Appl. Phys. Lett. 1964 (4) 89.
2. Pan, Z.W., Dai, Z.R. and Wang, Z.L. Science 2001 (291) 1947.
3. Ding, Y., Gao, P.X. and Wang, Z.L. J. Am. Chem. Soc. 2004 (126) 2066.
4. Wang, Z.L., Kong, X.Y., Ding, Y., Gao, P., Hughes, W.L., Yang, R. and Zhang, Y. Adv. Func. Mater. 2004 (14) 943.

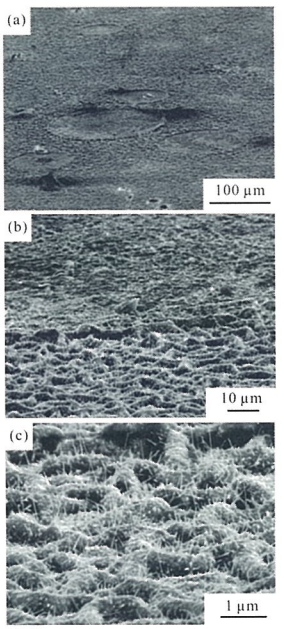

Figure 1.
(a) SEM image (SEI) of the Zn/W-ZnO deposited on glass and then annealed at 600°C for 1 h in air. (b) and (c) Further magnified images to show VLS growth of randomly oriented W-ZnO whiskers.

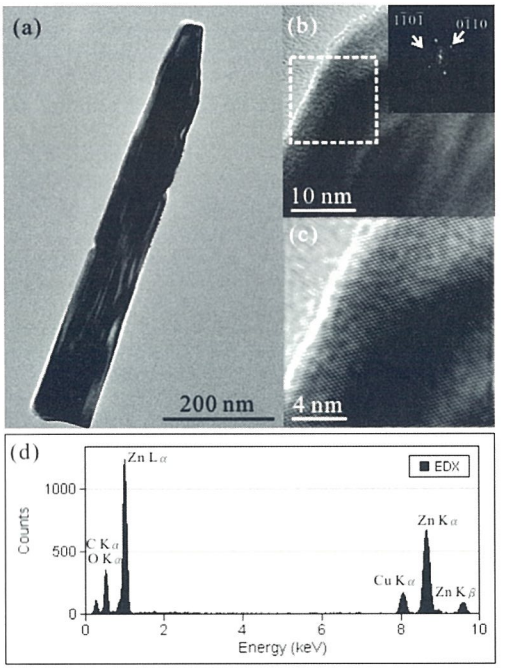

Figure 2.
TEM of a representative rod-like W-ZnO whisker (a) BFI, (b) lattice image and 2-D forward (inset) Fourier transform from the square region (c) inverse Fourier transform of (b), (d) Point count EDX spectrum of the W-ZnO whisker with Cu counts from the specimen holder and C counts from the carbon coated collodion film.

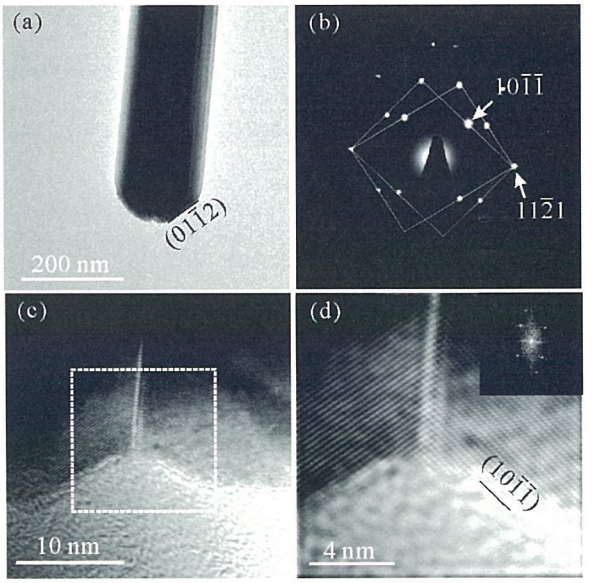

Figure 3.
TEM (a) BFI and (b) SAED pattern of W-ZnO whisker twinned over (11$\bar{2}$1) edge on in [4$\bar{5}$13] zone axis, (c) Lattice image and (d)2-D forward (inset) and inverse Fourier transform from thesquare region in (c) .

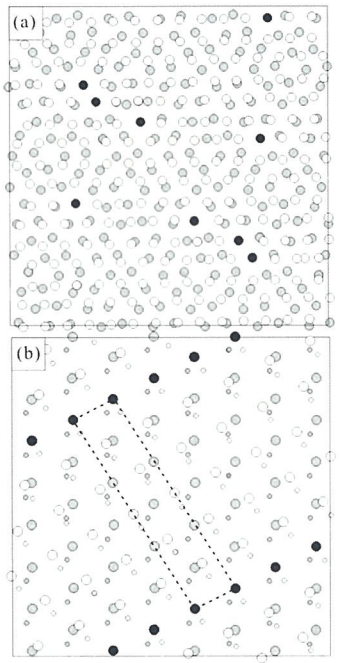

Figure 4.
Unrelaxed oxygen positions of the attached planes of (a) oxygen terminated {10$\bar{1}$1} and (b)cation-anion mixed (11$\bar{2}$1) both having the top (white)and bottom layer (gray) superimposed 52.2 degree off the parallel orientation to form {10$\bar{1}$1} and (11$\bar{2}$1) twin boundaries. The coincidenc sites of oxygen as denoted by dark solid circles show coincidence-site density of 1 in 6, i.e. Σ= 6 in the rectangular area outlined by dashed lines in (b) but poor coincidence in (a).

M-P-11 STUDY OF SURFACE PLASMON POLARITON PROPAGATION ON GOLD NANOWIRE ARRAYS BY NEAR-FIELD SCANNING OPTICAL MICROSCOPY

HUANG, Jyh-Hann (黃志翰) and LIN, Heh-Nan (林鶴南)

Department of Materials Science and Engineering, National Tsing Hua University, Hsinchu 30013, Taiwan

Surface plasmon polaritons (SPPs), which are spatially confined electromagnetic modes related to collective electron oscillations, are now attracting substantial interests. Due to the unique features of SPPs, two dimensional components such as SP mirrors, SP beam splitters [1], SP waveguides [2], etc. can be found in a broad range of applications including nanophotonics and biological sensing.

In this work, SPP excitation and propagation on gold patterns are studied by near-field optical scanning microscopy (NSOM). A schematic diagram of the experimental set-up is shown in Fig. 1. An e-beam lithography system is used to fabricate the required gold patterns on quartz substrates. The SPPs are excited by an attenuated total reflection (ATR) configuration with the use of a transverse magnetic polarized laser source (532 nm). The optical distributions on the gold patterns are studied by a commercial NSOM.

Illuminating gold microstripes (5 μm in width and 20 μm in length) uniformly as shown in Fig. 2(a), the optical image [Fig. 2(b)] shows the excitation of SPP. There is an obvious interference pattern in Fig. 2(b). Fig. 2(c) shows the cross-section profile of the interference pattern [the blue line part in Fig. 2(b)]. The measured wavelength of 480 nm is in good agreement with the calculated wavelength of the surface plasmons (λsp=471 nm). Gold nanowire (130 nm in width and 15 μm in length) arrays are illuminated by focusing a laser beam with two types of incident direction as shown in Fig. 3(a) and 3(d). With the incident direction parallel to the nanowire array [Fig. 3(b)], SPP is excited on one side of nanowire and propagating to the other side [Fig. 3(c)]. The measured wavelength of 479 nm is again in good agreement with the calculated wavelength. With the incident direction perpendicular to the nanowire array [Fig. 3(e)], the electromagnetic field enhancement on both sides of nanowires is 3.5 times larger than that on the quartz [Fig. 3(f)].

Reference

1. Ditlbacher, H., Krenn, J.R., Schider G., Leitner, A. and Aussenegg, F.R., Appl. Phys. Lett. 2002 (81) 1762.
2. Webber, J.C., Lacroute, Y. and Dereux, A., Phys. Rev. B 2003 (68) 115401.

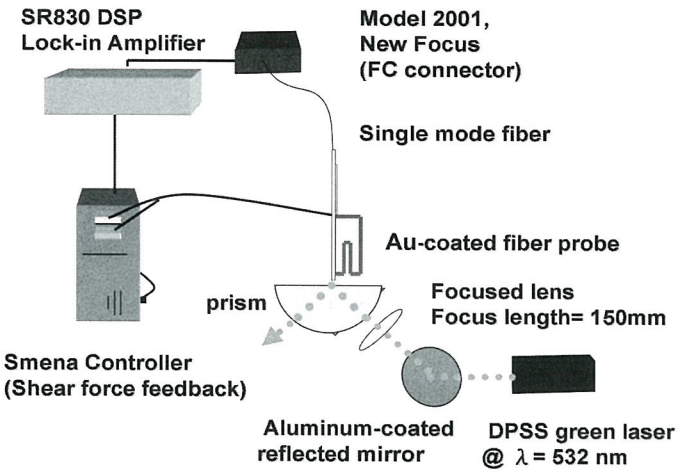

Fig. 1 The schematic of experimental set-up.

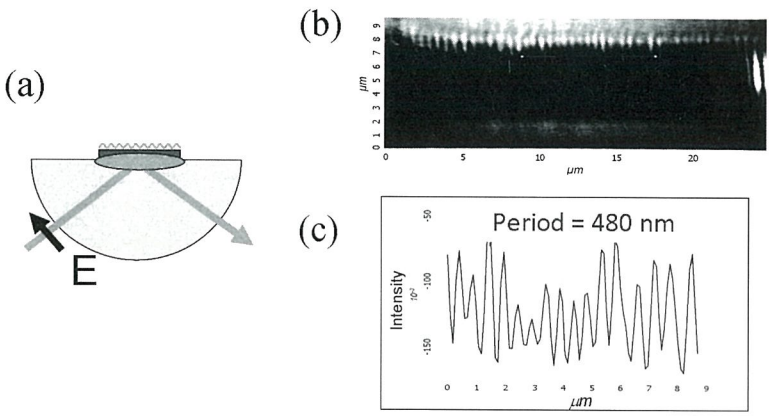

Fig. 2 (a) A schematic diagram of optical excitation. (b) Optical image of single gold stripe. (c) Cross-section profile of (b).

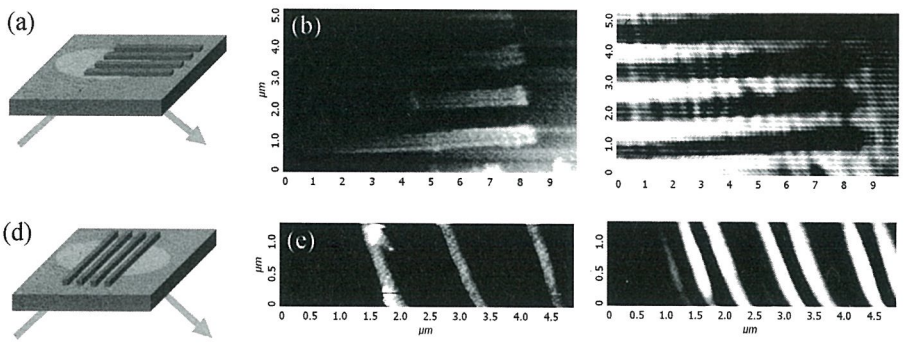

Fig. 3 (a), (d) Schematic diagrams of two different incident laser directions. (b), (e) are height images of nanowire arrays; (c), (f) are the corresponding optical images of (b), (e).

M-P-12 PIEZOELECTRIC CHARACTERIZATION OF SODIUM NIOBATE NANOWIRE BY PIEZORESPONSE FORCE MICROSCOPY

CHEN, Hsiang-An(陳香安)[1], KE, Tsung-Ying(柯聰盈)[1], LEE, Chi-Young(李紫原),[1,2]
LIN, Heh-Nan(林鶴南)[1]

[1]Department of Materials Science and Engineering and [2]Center of Nanotechnology, Materials Science, and Microsystem, National Tsing Hua University, Hsinchu 30013 Taiwan.

One-dimensional metal oxides, nanotubes and nanowires have been extensively investigated in recent years. Studies on the piezoelectricity of lead-free piezoelectric ceramics nanowires have received increasing interest because of their potential usefulness in environmental protection. Crystalline orthorhombic $NaNbO_3$ nanowires, as shown in Fig. 1, were synthesized by the simple base treatment of Nb_2O_5 with 10 M NaOH solution which has been reported in 2008 [1]. To measure the piezoelectric coefficient d_{zz} of an individual $NaNbO_3$ nanowire, piezoresponse force microscopy (PFM) was employed [2, 3]. The experiment was performed under ambient conditions by using a commercial atomic force microscope (AFM; Smena-A, NT-MDT).

As shown in Figure 2a, a nanowire dispersed on an Au film was then found and the AFM tip was held at various locations on the nanowire. A small alternate current (AC) voltage was applied between the Au-coated tip (NSC36/Cr-Au, MikroMasch) and the bottom Au film. The nanowire and consequently the tip vibrated at the same frequency and with the same amplitude due to the converse piezoelectric effect.

The topographic images of two nanowires with widths of 200 and 100 nm and heights of 80 and 120 nm, respectively, are shown in Figure 2b and 2c, respectively. The relationships between the tip deflection and the applied voltage amplitude at the locations A, B, and C marked in 2b and 2c are shown in Figure 2d－f, respectively. As expected, a linear behavior is observed in all curves. The average d_{zz} values are 0.85, 0.95 and 4.26 pm/V, respectively. As can be seen, the d_{zz} of the nanowire in Figure 2c is about four times as large as those of the nanowire in Figure 2b. The outcome suggests that a nanowire with a larger height-to-width ratio vibrates more easily under an applied electric field.

References

1. Ke, T.-Y., Chen, H.-A., Sheu, H.-S., Yeh, J.-W., Lin, H.-N., Lee, C.-Y., and Chiu, H.-T., J. Phys. Chem. C 2008 (in press)
2. Lin, H.-N., Chen, S.-H., Ho, S.-T., Chen, P.-R., Lin, I.-N., J. Vac. Sci. Technol. B 2003 (21) 916.
3. Zhao, M.-H., Wang Z.-L., and Mao, S.X., Nano Lett. 2004 (4) 587.

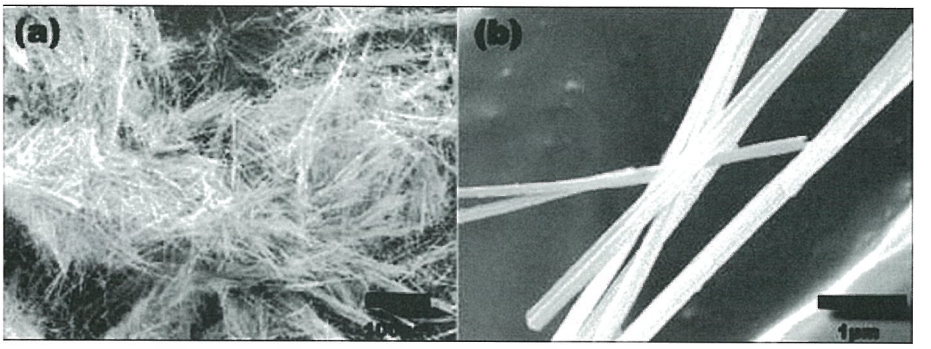

Figure 1. SEM images of the powders obtained by reacting Nb_2O_5 with 10 M NaOH solution. (a) The low magnification SEM image.(b) Enlarged view showing the bundles of the nanowires.

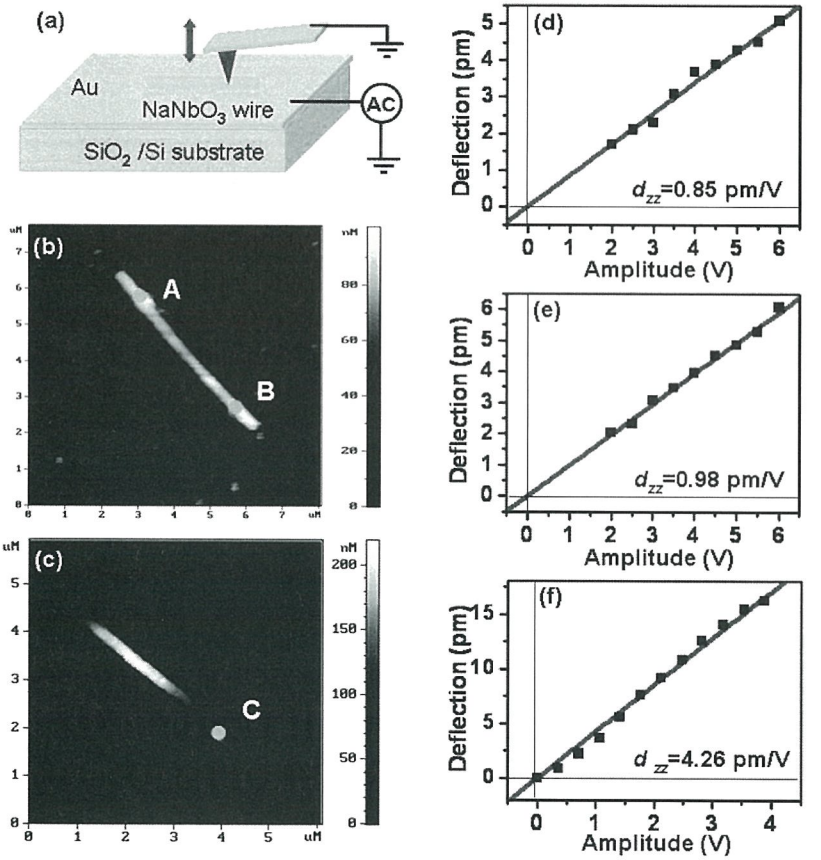

Figure 2. (a) A schematic diagram of the PFM experiment. (b) and (c) Topographic images of $NaNbO_3$ nanowires with widths of 200 and 100 nm, and heights of 80 nm and 120 nm, respectively. (d), (e) and (f) Deflection versus amplitude curves at the positions (d) A, (e) B and (f) C, respectively, marked in parts b and c.

M-P-13 THE MICROSTRUCTURAL EVOLUTION OF NUCLEAR GRADE GRAPHITE IN VERY HIGH TEMPERATURE GAS COOLED REACTORT (VHTGR) CORE ENVIRONMENTS

Y. T. Hsieh (謝佾蒼), J. J. Kai (開執中), F. R. Chen (陳福榮)

Center of Electron Microscopy, Department of Engineer and System Science,

National Tsing Hua University, Hsinchu 300, Taiwan

In very high temperature reactor, nuclear grade graphite is the major core material serving as reflector and moderator for internal structure of a reactor. Due to the high temperature and high neutron flux in the core, graphite will face very serious challenge in terms of microstructural evolution and helium embrittlement.

Graphite has the characteristics to store defect energy inside the crystalline lattice and will releases enormous amount of defect energy when the temperature reaches the critical annealing temperature which may cause serious problem in reactor safety.[refs]

In order to simulate the VHTR core environment, the graphite samples were irradiated by 3MeV carbon ions at temperatures from 500 ℃ to 1000 ℃ in our triple-beam accelerator chamber, and the doses is up to 3 dpa. Generally the most significant change of graphite in the core after irradiation is the variation of lattice spacing. Based on high resolution transmission electron microscope (HRTEM) images and diffraction patterns, the lattice spacing of c-axis can be determined from lattice sum technique[refs]. Our results show that the lattice spacing of {0002} apparently increased 15% after implantation at 600℃, and it only increased 9% and 5% at 500℃ and 1000℃, separately, Fig 1. In HRTEM images, the irradiation area shows wavy deformation of the basal plane and some planar defects, Fig 2. The disorder coefficient σ can be deduced from the FWHM (full width at half maximum) of {0002} peaks in power spectrum of HRTEM images, Fig 3. The parameter σ represents the degree of variation of lattice spacing in c-axis direction and quantity of lattice deformation. From the experimental results, the quantity of lattice deformation depends on the energy stored in the lattice. To combine the disorder coefficient σ and the power spectrum of HRTEM images, the lattice strain energy of graphite in c-axis can be calculated from Eq.1

$$\text{Strain Energy} = \frac{1}{2} E\varepsilon^2 = \frac{1}{2} c_{33} \left(\frac{\varepsilon_{ext}^{\ 2} + \varepsilon_{con}^{\ 2}}{2} \right) \quad \text{----(1)}$$

Where E is Young's modulus, ε is strain = ΔL/L, c_{33} = c-axis Young's modulus, ε_{ext} is strain of extension, ε_{con} is strain of contraction.

From the condition of the most serious deformation, 600℃ 3dpa, the temperature of graphite will be increased over than 900℃ if the strain energy released as the form of thermal energy in a flash, Tab 1. It may cause serious problem in reactor safety.

References

[1] Y. I. Shtrombakh, Journal of nuclear materials, Radiation damage of graphite and

carbon-graphite materials, (1995)
[2] A. Asthana, Y. Matsui, Journal of Applied Crystallography, Investigations on the structural disordering of neutron-irradiated highly oriented pyrolyticgraphite by X-ray diffraction and electron Microscopy, (2005)

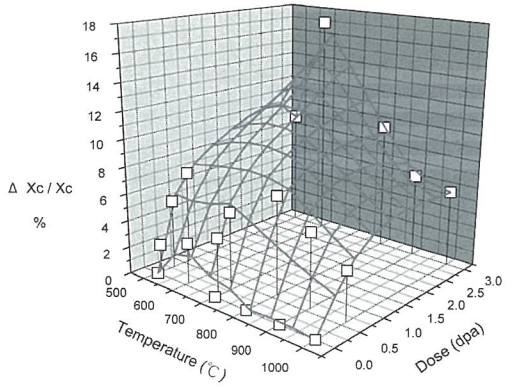

Fig. 1. Shows the dimensional change is different at variant irradiation temperatures.

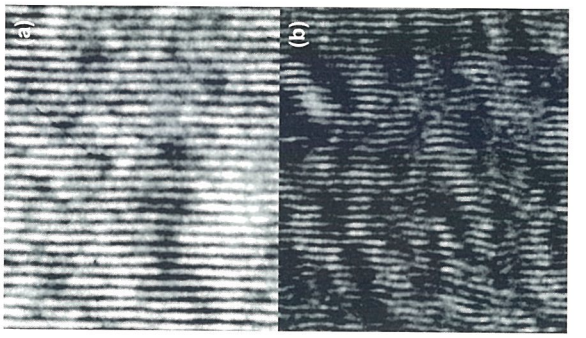

Fig. 2 (a) is un-irradiation graphite (b)is irradiated to 0.6 dpa. Show wavy deformation of the basal plane and some planar defects after ions irradiation.

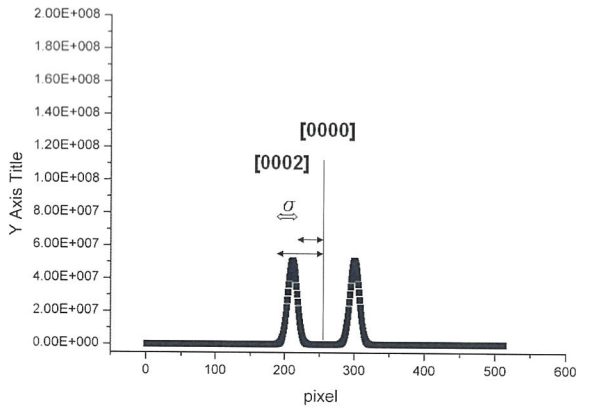

Fig.3 Define the FWHM of the Gaussian profile to be σ, which represent the difference in reciprocal space.

Irradiation Temp. (℃)	Dose (dpa)	Strain energy (J/cm^3)	Raising Temp. (℃)
600	0.4	189.8	123.7
	3	1405.25	916.1
1000	0.6	111.3	72.6
	3	206.2	134.4

*Young's modulus c_{33} = 36.5 GPa
Volumetric heat capacity = 1.534 J / cm^3 • K

Tab.1 Releasing of the strain energy may cause serious problem to graphite.

M_P-14 STEM OBSERVATION ON γ'' CHEMICALLY SENSITIVE PRECIPITATES IN INCONEL 718

LEE, Wei-Chih(李威志)[1], TSENG, Yi-Kai(曾奕愷)[1], Liao, jia-wei(廖家偉)[2], YANG, Jer-Ren(楊哲人)[1]

[1]Department of Materials Science and Engineering, National Taiwan University Taipei, Taiwan
[2] E.B. TECH CO., LTD, Taiwan

Inconel alloys are important industrial materials for oxidation and corrosion resistant application in extreme environments. It retains strength over a wide temperature range, attractive for high temperature applications and the strength is developed by solid solution strengthening or precipitation strengthening, depending on the alloy. It is well known in age hardening or precipitation strengthening varieties, small amounts of niobium, aluminum and titanium combine with nickel to form the intermetallic compounds. γ'' [$Ni_3(Al,Ti)$] is the metastable phase, which tends to transform gradually into the stable phase, δ [Ni_3Nb], during aging. All previous studies have shown the morphology and crystallographic relationship between γ'' and δ clearly, but there is no investigation on the composition of interior γ'' precipitates. This study reveals the composition of γ'' , which contains small amounts of Al, Ti, Nb and Ni.

The present material was provided by GMTC Company and the chemical composition was measured by EPMA(JXA-8200, JEOL), as shown in Table 1.The sample was heated for 10 hours at 900 ℃, and then cooled in the furnace. The nano-structures with the chemical analysis were carried out using FEI TECNAI F30 FEG-TEM equipped with HAADF and EDS detectors. Fig. 1 shows the nano-structure, which reveals the detailed morphology of γ'' . The line-scan EDS analysis and mapping were also carried out in STEM mode in order to confirm the local composition of the core structure, as shown in Fig. 2 and 3. Small amounts of Al, Ti, Nb and Ni within the γ'' indicate the stage of γ'' phase transformation to δ phase.

References

1. Y. Rong, S. Chen, G.. Hu, M. Gao and R. P. Wei, Metall. Mater. Trans., 1999 (30A) 2297.
2. M. Sundararman, P. Mukhopadhyay and S. Banerjee, Metall. Trans., 1988 (19A) 453.
3. D. S. Weaver and S. L. Semiatin, Scr. Metall., 2007(57)1044.

Table 1 Chemical composition of sample. (mass%)

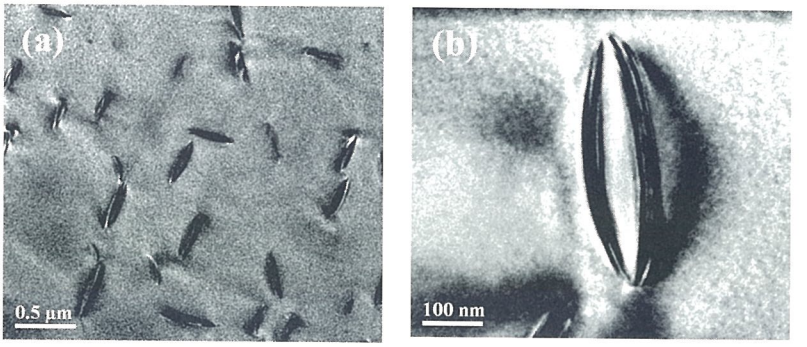

Fig. 1 TEM micrograph of γ'' precipitates from the γ matrix aged at 900℃ for 10 hours: (a) overview of γ'' precipitates within γ matrix, (b) enlarge micrograph.

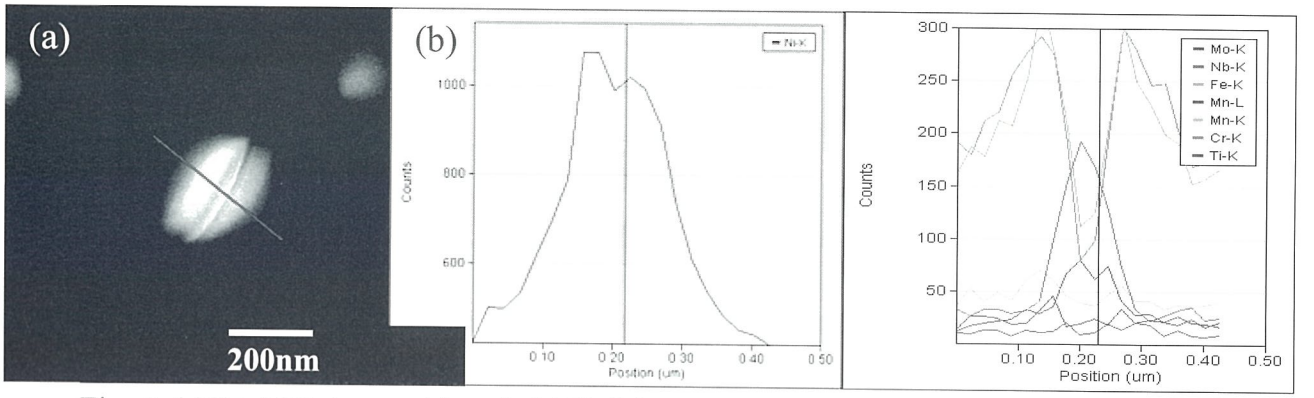

Fig. 2 (a)HAADF image (a) and (b)EDS intensity profile of the γ'' precipitate. The EDS intensity profile is obtained along the line in (a).

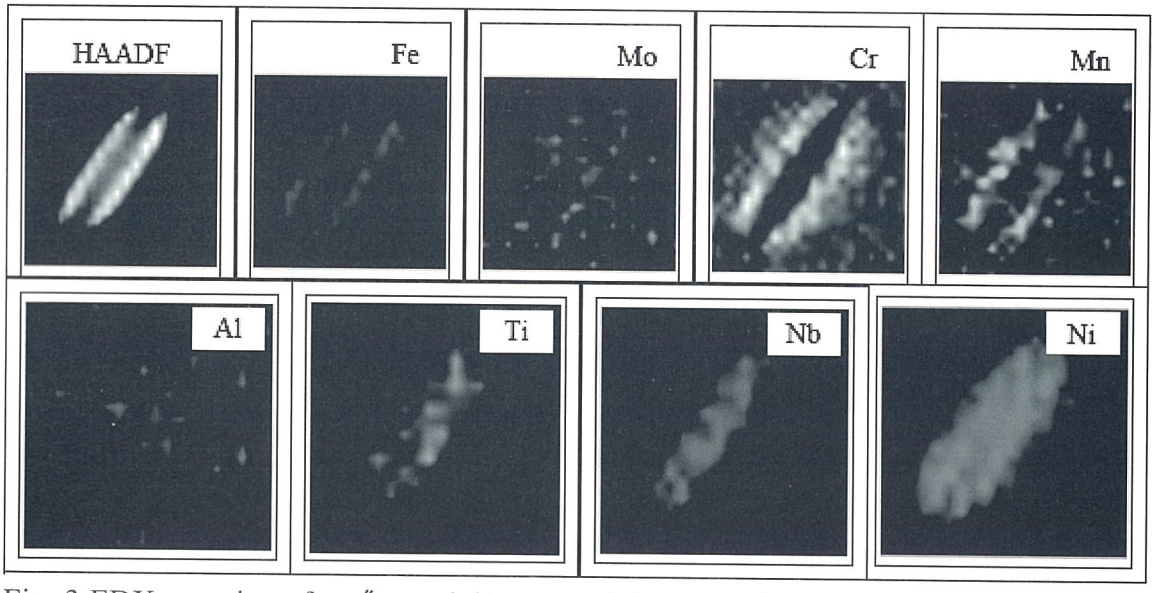

Fig. 3 EDX mapping of γ'' precipitate containing some levels of Fe, Mo, Cr, Mn, Al, Ti, Nb and Ni.

M-P-15 DESIGN AN NEW NON-VOLATILE MEMORY DEVICE USING COPPER NANOBRIDGING IN TANTALUM-OXIDE FILMS

LEE, Wei-Chih(李威志)[1] , S. Maikap[2](麥凱), YANG, Jer-Ren(楊哲人)[1]

[1] Department of Materials Science and Engineering, National Taiwan University Taipei, Taiwan

[2] Department of Electronic Engineering, Chang Gung University, Tao-Yuan,Taiwan

Many kinds of nonvolatile memory (NVM) devices with the technical limitations of scalability potential, higher switching power, nonvolatility, and reliability, etc. have been reported by several groups. To overcome those problems, a resistive switching memory device using novel Cu/Ta_2O_5/TiN/Si memory structure is one of the promising candidates for future nanoscale memories in the semiconductor industry, which has been reported in this study. A TiN metal with a thickness of ~30 nm for a bottom electrode was deposited by sputtering. Then, the high-κ Ta_2O_5 film with a thickness of ~11 nm was deposited by also reactive sputtering. Then, the Cu acted as a top electrode was deposited by thermal evaporation.

A schematic memory structure of the Cu/Ta_2O_5/TiN is shown in Fig. 1(a). To probe the thickness and microstructure of the Ta_2O_5 film, high resolution transmission electron microscopy (HRTEM) was performed. The thicknesses of the high-κ Ta_2O_5 and TiN metal layers are found to be ~11 nm and ~30 nm, respectively [Fig. 1(b)]. The TiN and Ta_2O_5 films were confirmed by EDS analysis [Fig. 1(c) & (d)]. The current-voltage (I-V) sweeping is started from 0V to positive bias (arrow 1 & 2), as shown in Fig. 2. Now the memory device is sweeping back to +1V to 0V (arrows 3 & 4). The memory device can continue the negative voltage up to -1V. (arrow 5 &6). A negative 1V is needed to become a high resistance state of the memory device and the device will maintain the high resistance state from -1V to +0.35V (arrow 7). If one can read the high resistance (R_{high}=2x10^5 Ω) and low resistance (R_{low}=4.4x10^2 Ω) states at a voltage of V_{read} (=0.2V) then the ratio of R_{high}/R_{low} is 4.4x10^2. This nonvolatile memory device can be applied for nanoscale applications.

References:

1. J. R. Hwang et al., IEDM Tech. Dig., 2005, p.161.

2. S. Maikap et al., Semicond. Sci. Technol., vol.22, p. 884, 2007.

3. S. Maikap et al., Appl. Phys. Lett., vol. 91, p. 043114, 2007.

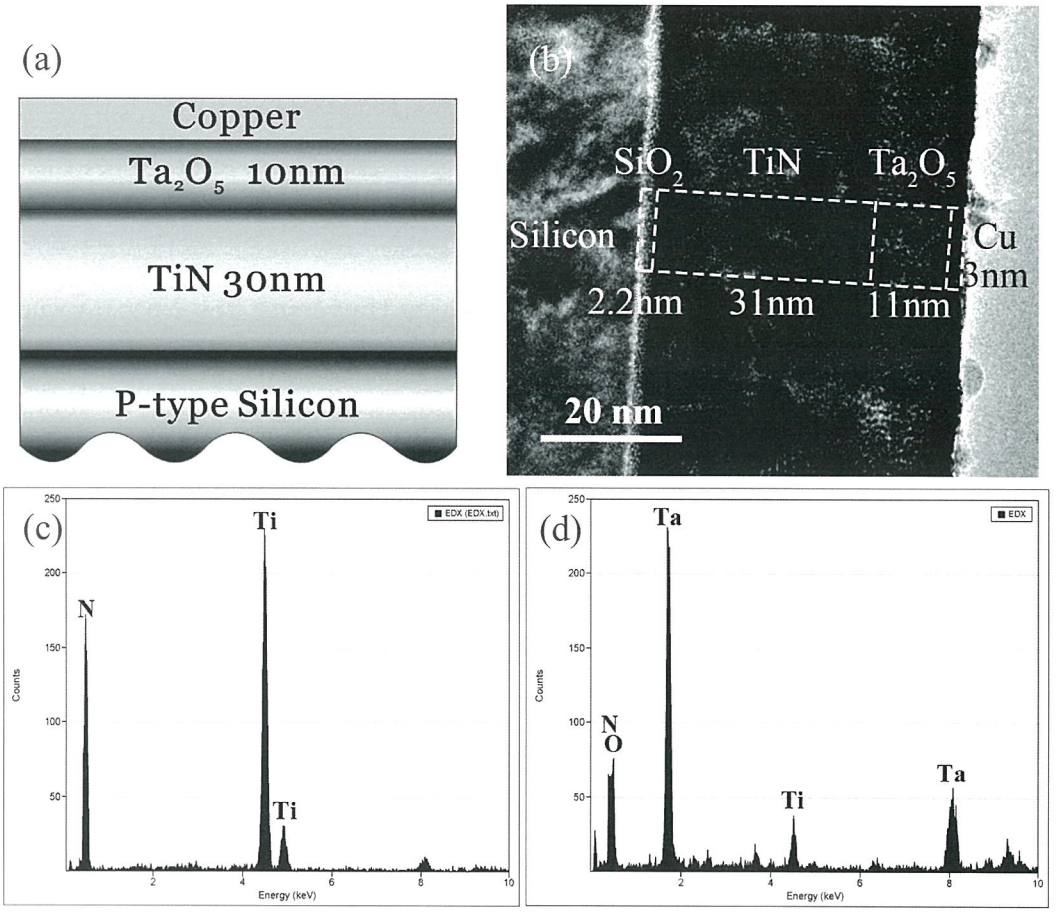

Fig. 1 (a) Schematic diagram of the nonvolatile memory device, (b)cross-sectional HRTEM image of TiN/Ta_2O_5/Cu memory structure and EDS spectrums taken from the area marked as (c)TiN, (d)Ta_2O_5, respectively.

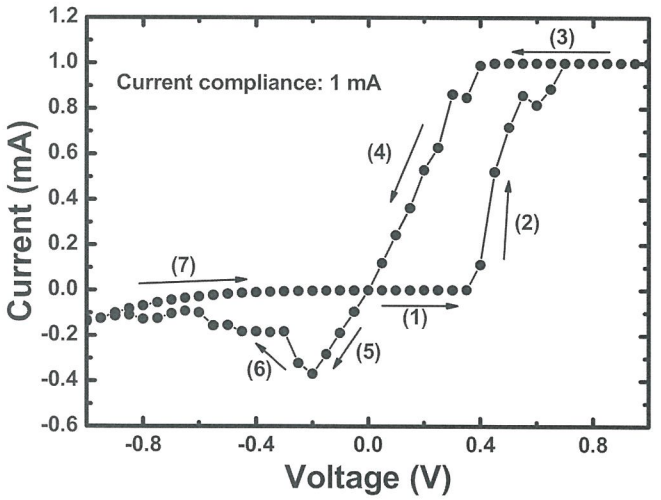

Fig. 2 Current-voltage (I-V) hysteresis window is measured from the Cu nanobridging in the Ta_2O_5 films.

M-P-16 Cu DOED RuO_2 NANOWIRES－ELECTRICAL PROPERTIES MEASURED INSIDE A TRANSMISSION ELECTRON MICROSCOPE

Chen, Cheng-Chi (陳政琦)；Kai, Ji- Jung(開執中)[a] and Chen, Fu-Rong (陳福榮)[a]

[a]Center of Electron Microscopy, Department of Engineering and System Science, National Tsing Hua University, Hsinchu 300, Taiwan

The exceptional physical properties of transition metal oxides (TMO) are of particular interest in developing next-generation materials. RuO_2 belongs to a transition metal oxide family and exhibit many exceptional physical properties like metallic conductivity at room temperature, thermal stability, chemical stability [1]. Therefore, RuO_2 nanowires can be a good candidate for leading wire. However, in order to improve the electrical property, RuO_2 nanowires were doped with Cu ions and electrical properties were measured by nano-probe that has been integrated based on the scanning tunneling microscopy (STM) technique into an TEM holder for transmission electron microscopes (TEM-STM) [2][3][4][5].

RuO_2 nanowires were ion implanted to dosage of $1x10^{16}$ ions/cm^{-2}、$3x10^{16}$ ions/cm^{-2} and $5x10^{16}$ ions/cm^{-2} by 72keV Cu^+ ions, respectively. Then, the specimens were annealed at 350℃ under Ar flow for 40 hours to reduce the damage from ion implantation. The concentrations of Cu were determined from nano-beam EDX to be about 0.76 at%、2.62 at% and 4.28 at% in RuO_2 nanowires for dosage of $1x10^{16}$ ions/cm^{-2}、$3x10^{16}$ ions/cm^{-2} and $5x10^{16}$ ions/cm^{-2}, respectively
(Fig. 1 shows Cu at% vs dosage). The electrical properties of rutile-type RuO_2:Cu low-dimensional structures were carried out with the STM-TEM holder. The STM-TEM holder actually gives I-V relationship of many nano-wires with different length l and cross-section area A under the condition of two probes technique. The I-V data obtained typically show linear behavior between the gold electrodeand Cu doped RuO_2 nanowires at all contact points. The contact resistance (R_c) and resistivity (ρ) from can be determined from fitting the equation $R = R_c + R_{wire} = R_c + \rho \times (l / A)$. In Fig.3 the contact resistance in sample with dose $1x10^{16}$ ions/cm^{-2} is 2.48kΩ and the resistivity is 46.6 μΩ-cm. In Fig.4 the contact resistance in sample with dose $3x10^{16}$ ions/cm^{-2} is 2.12kΩ and the resistivity is 642.8 μΩ-cm.

References

[1] Qingmin Ji and Toshimi Shimizu, The Royal Society of Chemistry 2005
[2] Hiroshi Morikawa and Keisuke Goto, Rev. Sci. Instrum, 59 (1988) 2159
[3] F. Wakaya, Y. Ogi, M. Yoshida, S. Kimura, M. Takai, Y. Akasaka, K.Gamo, Microelectronic Engineering, 73 (2004) 559
[4] Magnus W. Larsson, L. Reine Wallenberg, Ann I. Persson, and Lars Samuelson, Microscopy and Microanalysis: Microscopy Society of America 10 (2004) 41
[5] Pedro M. F. J. Costa A Dmitri Golberg A Guozhen Shen A Masanori Mitome A,J Mater Sci (2008) 43:1460-1470

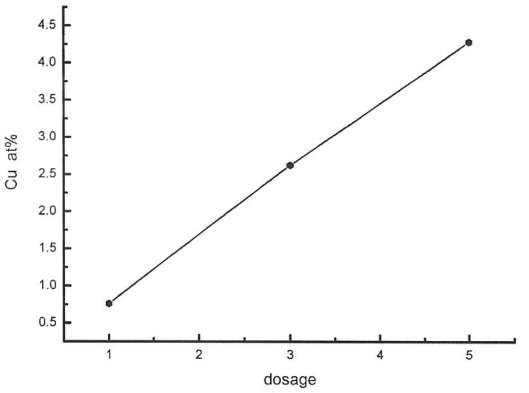

Fig.1 Cu at% vs. the dosage

Fig.(2a) TEM-STM image of Cu doped RuO_2 nanowires.

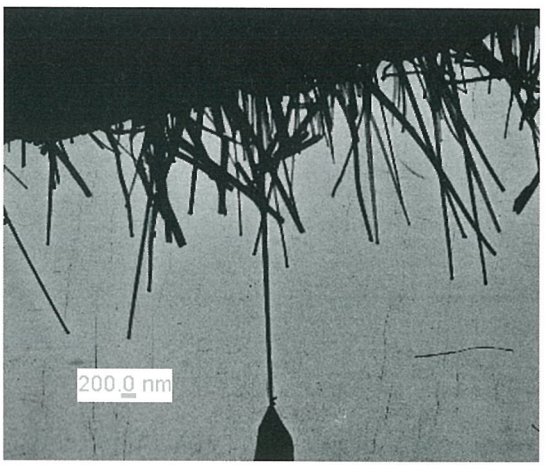

Fig. (2b) A gold STM tip in contact with individual RuO_2 nanowire.

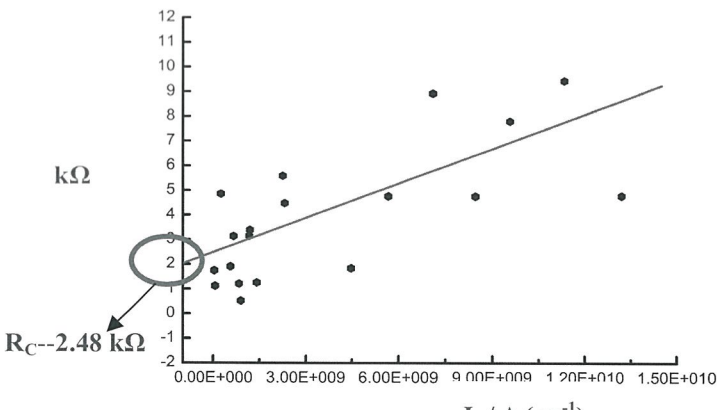

Fig .3 From equation

$R = R_c + R_{wire} = R_c + \rho \times (l / A)$,

the contact resistance (R_c) is 2.48k Ω and resistivity (ρ) is about 46.6μΩ-cm.

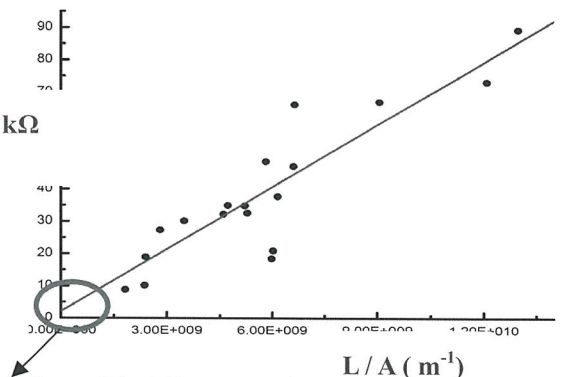

Fig 4 From equation

$R = R_c + R_{wire} = R_c + \rho \times (l / A)$,

the contact resistance (R_c) is 2.12k Ω and resistivity (ρ) is about 642.8μΩ-cm.

M-P-17 MICROSTRUCTURE EVOLUTION OF SINGLE CRYSTAL HEXAGONAL SIC UNDER SI ION IRRADIATION AT ELEVATED TEMPERATURES

HO, Chung-Jung (何宗融)；KAI, Ji-Jun (開執中) and CHEN, Fu-Rung(陳福榮)

Center of Electron Microscopy, Department of Engineer and System Science, National Tsing Hua University, Hsinchu 300, Taiwan

Silicon carbide is considered to be a promising material in nuclear systems, such as the coating of fuel particles in very high temperature reactors (VHTR) [1] and structural material in fusion reactors. The main concerns about using this material are the stability of microstructure during irradiation at high temperatures, the low radioactivity after irradiation, and the high strength at high temperatures [2].

The material used was commercially available single crystal 6H silicon carbide wafer with (0 0 0 6) orientation in its vertical axis. In this study, we irradiated SiC up to 10 dpa using 5.4 MeV Si^{3+} ion beam to simulate the radiation damage produced by neutron bombardment in nuclear reactors. The depth distribution of the displacement and implanted Si ions are calculated by TRIM-code, shown as Fig. 1. The microstructural evolution of irradiated SiC is examined by transmission electron microscopy, and the thickness is determined by Electron Energy-Loss Spectra. After irradiation, the dislocation loops formed above 600 ℃. By using the weak beam dark field technique, dislocation loops was identified as bright spot at dark field images (Fig. 2). The average radius of the loops is 1.78±0.43 nm, and the average density is about 4.69×10^{23}($\#/m^3$). The loop radius decreased to 1.64±0.38 nm as the irradiation temperature increased from 600 ℃ to 1000 ℃, and the density increased to 5.62×10^{23}($\#/m^3$), shown as Fig. 3. Katoh and his coworkers had also found that the dislocation loops in cubic SiC after irradiation at several hundred degrees Celsius [3]. However, the temperature that dislocation loops start to form in 6H SiC is lower and the size of the loops are smaller than which Katoh reported. We will continue to do higher temperature irradiation experiment to obtain the more explicit relation between radiation damage and temperature. Also, identifying whether the loop is interstitial or vacancy type is the destination.

References

[1] R.J. Price, Nucl. Technol. 35 (1977) 320.
[2] L.L. Snead, R.H. Jones, A. Kohyama, P. Fenici, J. Nucl. Mater. 233-237 (1996) 26-36.
[3] Y. Katoh, N. Hashimoto, S. Kondo, L.L. Snead, J. Nucl. Mater. 351 (2006) 228.

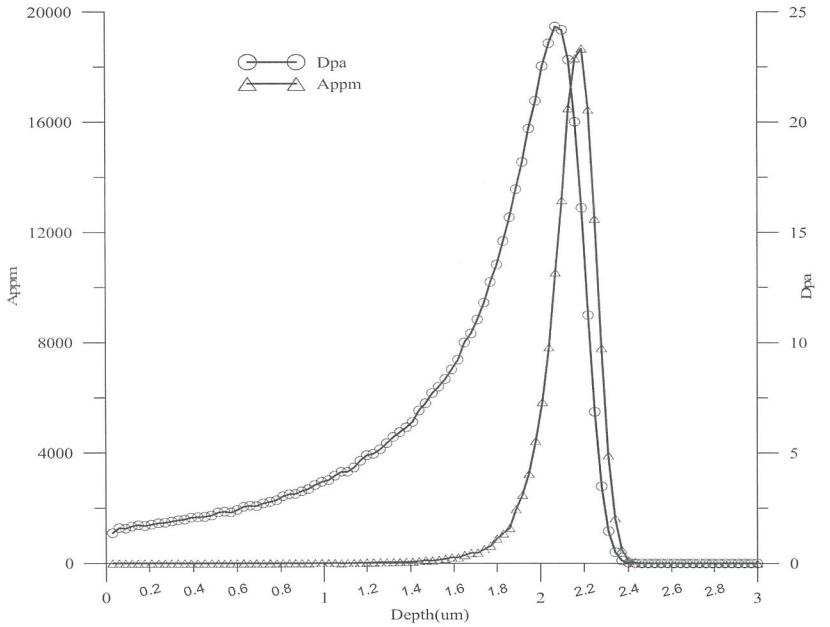

Fig. 1 TRIM-code simulation of depth distribution for displacement and implanted ions

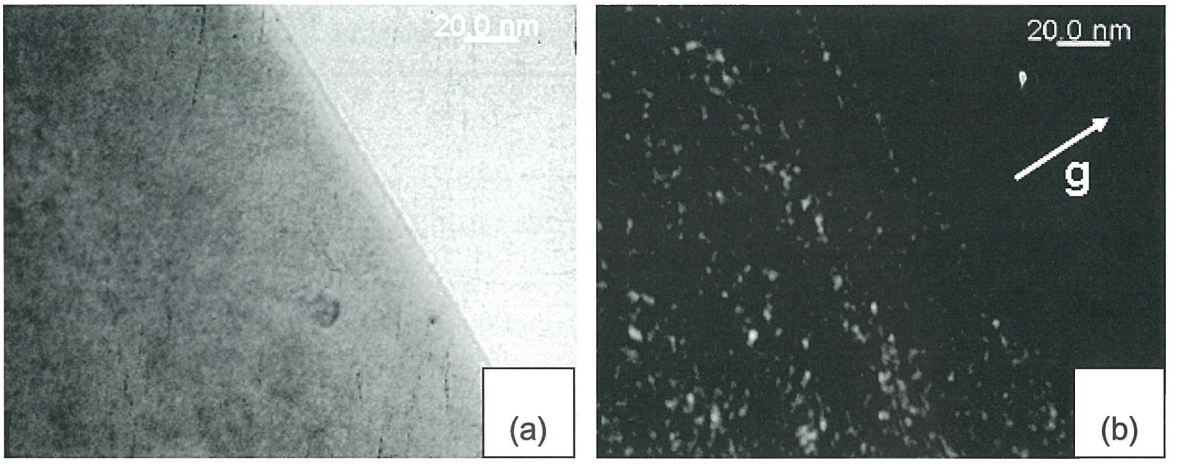

Fig. 2 weak beam (a)bright field and (b)dark field image of 600 ℃ 10 dpa, B~[1 -1 0 0] and g=(0 0 0 6)

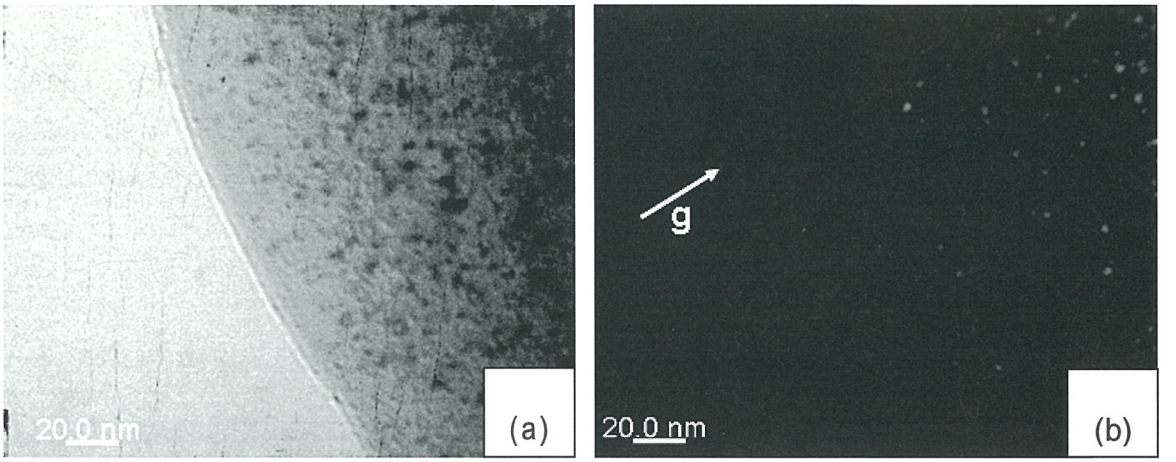

Fig. 3 weak beam (a)bright field and (b)dark field image of 1000 ℃ 10 dpa, B~[1 -1 0 0] and g=(0 0 0 6)

M-P-18 TH

HUANG, Jyun-Hac

Center of Electron M
National Tsing Hua U

Diluted magne
fabricated by incorp
considerable attentio
spin degrees of fre
functionality for micr
ferromagnetic semic
relationship of struct
ions. This result is
temperature DMS t
technology in future s

The substrate w
selected as a dopant
ions/cm^2. Then the sp
under N_2 flow for 3 m

Fig. 1 are low
showing no second
annealing temperatu
quantum interference
the specimens with s
that samples annealed
but with reduction of
M-T curve showing
properties are therefo
measurement shows th
900℃ was higher than
the resistivity after 110

The streaking di
damage of ion implant
second phase or Co cl
from second phase.

Reference:

[1] H.Ohno, science28
[2] T. Dietl, H. Ohno, I
[3] S. J. Pearton, N. Th
N. G. Chu, R. G. W

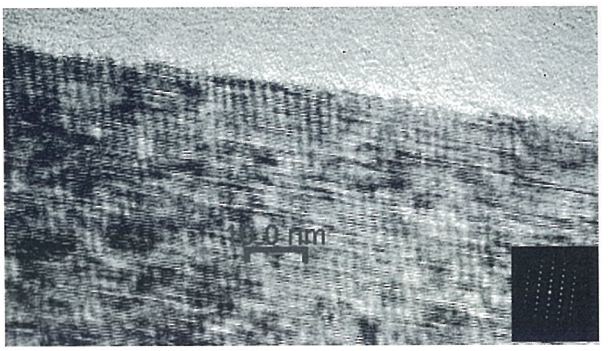

(a)800℃ 2x10^{16} ions/cm^{-2}

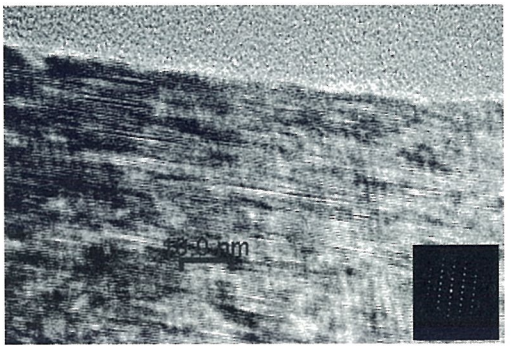

(b)900℃ 2x10^{16} ions/cm^{-2}

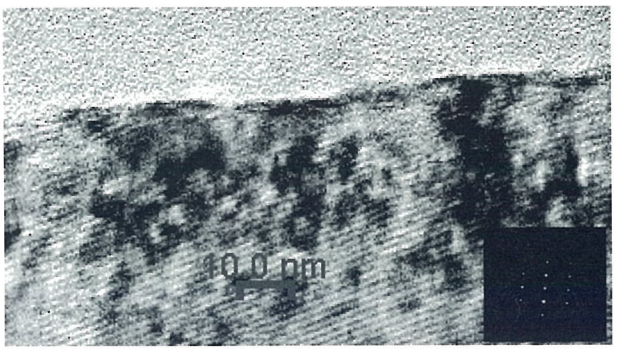

(c)1100℃ 1x10^{16} ions/cm^{-2}

Fig. Ⅰ

TEM analysis of implanted GaN at different annealing temperature, (a) 800℃ 2x10^{16} ions/cm^{-2}, (b) 900℃ 2x10^{16} ions/cm^{-2}, (c) 1100℃ 1x10^{16} ions/cm^{-2}

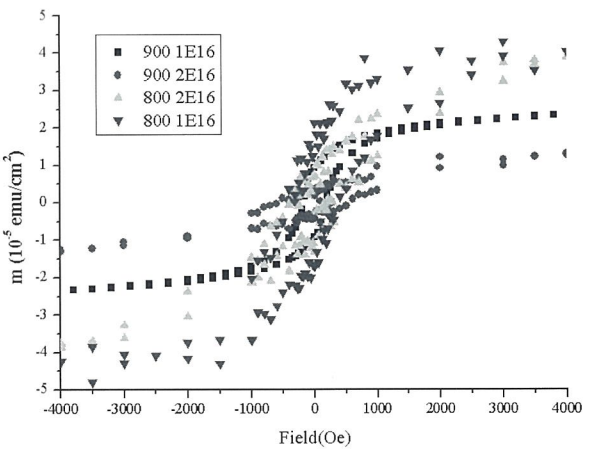

(d)

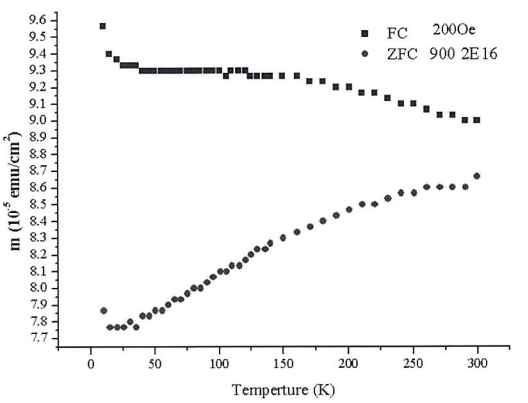

(e)

Fig. Ⅱ

(d) M-H curve of different temperature (e) M-T curve of the specimen annealed at 900℃

M-P-21 HIGH TEMPERATURE TRIPLE-ION BEAM IRRADIATION EFFECT ON HELIUM BUBBLE FORMATION IN Hi-NICALON TYPE-S SiC_f/SiC COMPOSITE

C.H. Chen(陳建宏)[a], K.F. Chen(陳科夆)[a], S. W. Lee(李尚偉)[a], L.U. YU[a], J. J. Kai(開執中)[a*], F. R. Chen(陳福榮)[a], Y. Katoh[b]

[a]Center of Electron Microscopy, Department of Engineer and System Science, National Tsing Hua University, Hsinchu 300, Taiwan
[b]Metals and Ceramic Division, Oak Ridge National Laboratory, Oak Ridge, TN, U.S.A.

Silicon carbide fiber-reinforced silicon carbide matrix composites are the major candidate structural material for fusion reactors. One of the main concerns of the SiC_f/SiC composite is the radiation stability in fusion environment. This study is to investigate the microstructural evolution of SiC_f/SiC composites in fusion reactor, especially the helium cavity formation induced by radiation at elevated temperature. We irradiated the Hi-Nicalon Type-S SiC_f/SiC composite to 10dpa and 100dpa at 1100℃~1300℃ by triple-ion beam irradiation (Si+He+H), and the He/dpa and H/dpa ratio are 150appm and 60appm respectively.

The microstructural evolution of irradiated SiC_f/SiC composite was examined by transmission electron microscopy, and the helium were observed by Electron Energy-Loss Spectrometers (EELS).The energy shift is due to the overlap of the wavefunction of neighboring atoms [1] and it is a function of He density. Lucas et al. have derived the relationship between the energy shift of He K-edge and helium density using a model based on He atom pair interaction potentials. And Fig.4 shows the relation between density and energy shift .

After triple-ion beam irradiation , helium bubbles were formed both in matrix and fiber above 900℃ and the size growing up while increasing radiation temperature (Fig.1 and Fig.2 show that the bubble size becoming larger when temperature increased) [2]. The average bubble size of fig.1 and fig.2 are 2.49nm and 2.93nm. It is observed that hydrogen plays a role to enhance the nucleation rate of He-bubble and in turn reduces the average diameter of the bubbles[3]. Fig.3 shows helium distribution in SiC_f/SiC composite (Considering about helium diffusion at high temperature). Measuring helium bubbles by EELS, about 50%~60% of the incident helium were trapped in bubbles within SiC_f/SiC above 1100℃ radiation temperature.

Reference：

[1] C. A. Walsh, J. Yuan, L. M. Brown, Philo. Mag. 80 (2000) 1507.
[2] P. Jung, J. Nucl. Mater, 191-194 (1992) 377.
[3] G. A. Esteban, A. Perujo, F. Legarda, L. A. Sedano, B. Riccardi, Journal of Nuclear Material, 307-311 (2002) 1430-1435.

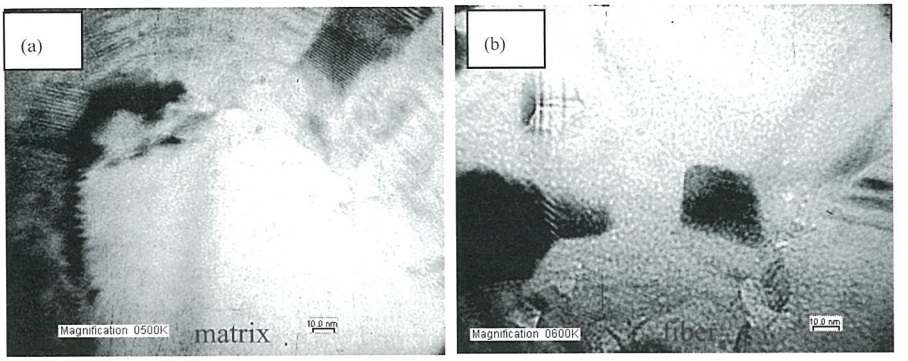

Figure 1 1100℃/10dpa Radiation induced Helium bubbles observed in SiC_f/SiC composites (a)matrix (b)fiber

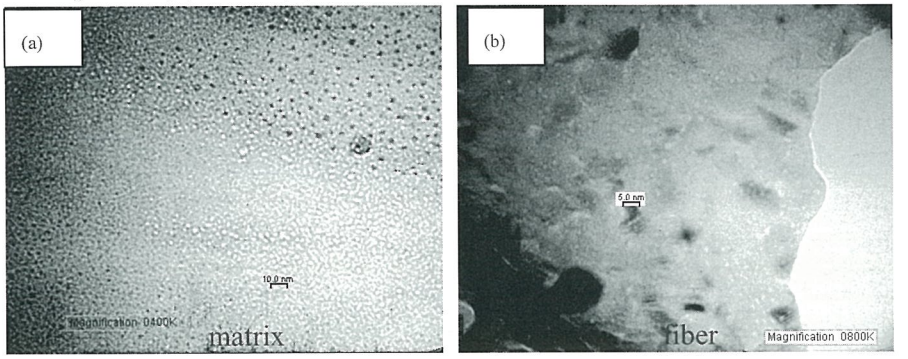

Figure 2 1200℃/10dpa Radiation induced Helium bubbles observed in SiC_f/SiC composites (a)matrix (b)fiber

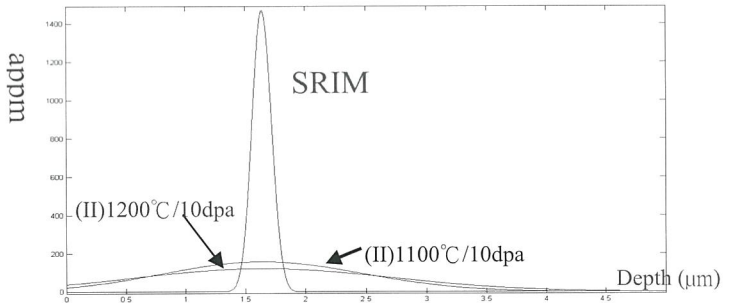

Figure 3 Helium distribution after diffusion simulation

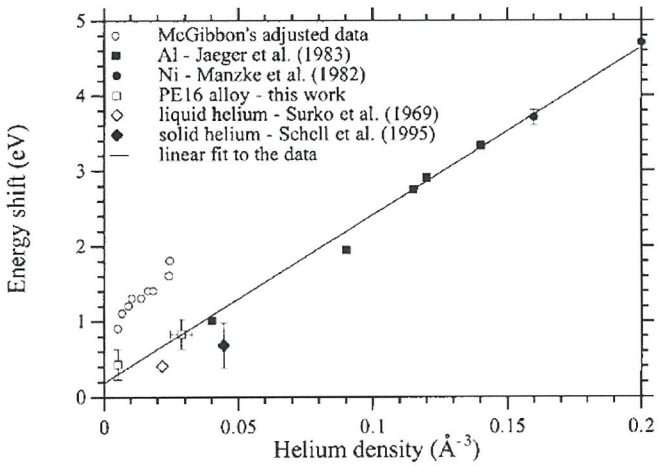

Figure 4 The relation between density and energy shift.

M-P-21 MICROSTRUCTURE EVOLUTION OF VANADIUM CONVERSION COATINGS ON MAGNESIUM ALLOYS

YANG, Kuang-Hsuan(楊光絢)[1], CHENG, Wei-Kun(程偉堃)[2]
and Ger, Min-Der(葛明德)[3]

[1] Department of Chemical and Materials Engineering, Vanung University, Tao-Yuan, Taiwan
[2] Department of Applied Chemistry, Chung Cheng Institute of Technology, National Defense University, Taiwan, ROC

Chemical conversion coatings are widely used on various active engineering alloys to improve paint adhesion and corrosion protection. Due to the environment concern, we have developed a new generation technical solution, vanadium system, to replace hexavalent system. Review of all conversion coating treatments, including chromate and other alternative conversion processes, and the color, thickness, and corrosion resistance of the conversion coatings can be altered by variation of solution composition, pH, temperature, and time of immersion. Thus this study aims to characterize the microstructure evolution of vanadium passive films with immersion time increasing.

Coatings were deposited at room temperature by immersing the AZ31 magnesium alloys in a solution containing $NaVO_3$ $30gl^{-1}$. Surface images indicate although increasing the immersion time, the polishing scratches are still visible because the coating thickness is very thin. Cross-sectional TEM bright-field reveal the structure is consisted of two layers: a compact layer contacting the substrate and a unstructured overlay as the major layer. EDX spectrums show the compositions are mainly $Mg(OH)_2$ and $VO(OH)_2$.

References

1. J. E. Gray and B. Luan, J. Alloys and Compounds, 336(2002), 88.
2. O. Lunder, J. C. Walmsley, P. Mack, K. Nisancioglu, Corr. Sci. 47(2005) 1604.
3. C. S. Lin and S. K. Fang, J. Electrochemical Soc. 152(2005)B54.
4. C.S. Lin, H.C. Lin, K.M. Lin and W.C. Lai, Corr. Sci. 48 (2006) 93.
5. C. S. Lin, C. Y. Lee, W. C. Li, Y. S. Chen and G. N. Fang, J. Electrochemical Soc. 153(2006)B90.

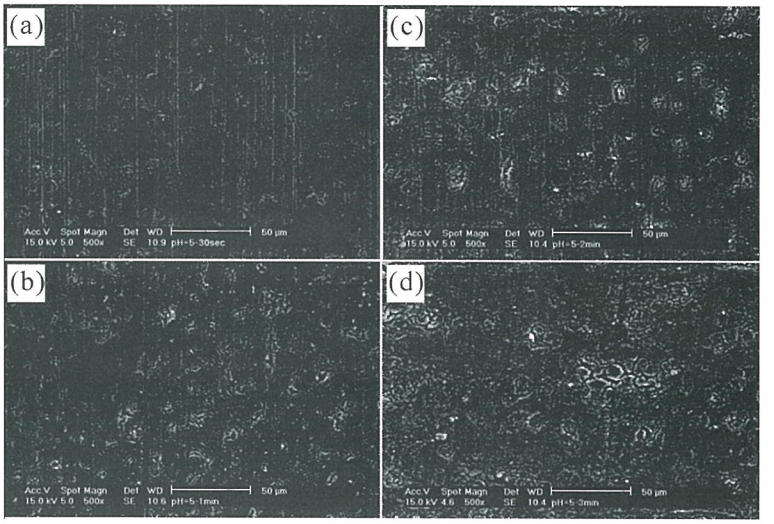

Fig. 1 Evolution of surface morphology on AZ31 plate immersed in the $NaVO_3$ solution for: (a) 0.5, (b) 1 , (c) 2 and (d) 3 min.

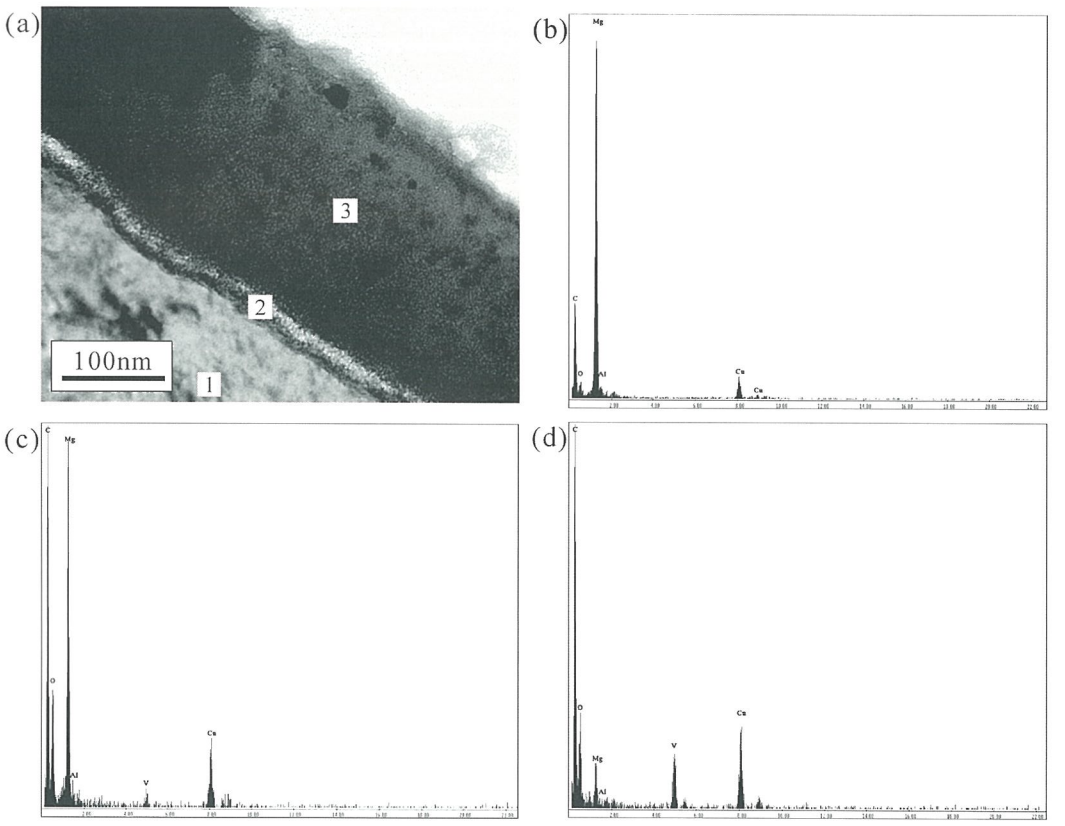

Fig. 2 Cross-sectional TEM bright-field images of the coating immersed in bath for 1 min and EDS analysis taken from the areas marked as 1, 2 and 3, respectively.

M-P-22 TEM AND HADDF-STEM INVESTIGATION ON NANOMETER-SIZED CARBIDES IN ULTRAHIGH-STRENGTH STEELS

YEN, Hung-Wei(顏鴻威), CHEN, Bo-Yu(陳伯宇) and YANG, Jer-Ren(楊哲人)

Department of Materials Science and Engineering, National Taiwan University, Taipei, Taiwan

Nanometer-sized carbides were reported as one of the most effective methods to achieve the ultrahigh-strength steels. Recently, complex carbides (Ti, Mo)C_x which contribute up to 300MPa in newly developed ultrahigh-strength steels has been thought as a landmark of precipitation strengthening in steels [1]. In this study, the interphase precipitation of (Ti, Mo)C_x will be investigated by Transmission Electron Microscope (TEM) and High Angle Annular Dark Field-Scanning TEM (HAADF-STEM) to elucidate the relationship between the ferrite transformation and the carbide formation.

The experimental steel with composition Fe–0.1C–1.5Mn–0.1Si–0.2Ti–0.2Mo was isothermally heat treated at 650°C, 680°C, 700°C, following the austenization at 1200°C, and finally quenched to room temperature as shown. The specimens for optical metallography were mechanically polished and then etched in 2% nital solution. TEM samples were mechined into 350 μm thick discs slit from the dilatometer specimens. The discs were then thinned to 60 μm by abrasion on silicon carbide paper and then electropolished in a twin jet electropolisher using a solution of 5% perchloric, 25% glycerol, and 70% ethanol at -10℃ and 40V.

In the optical metallography as shown in Figure 1, the white contrast reveals the ferritic phase and the dark contrast reveals the martensitic phase. Figure 2 shows the microstructure in the ferritic phase which isothermally transforms at 650, 680, 700°C respectively. It is obvious that a lower isothermal temperature induces a larger size of carbides and sheet spacing of interphase precipitation. This result is highly consistent with the ferritic transformation rate [2]. And the lower isothermal temperature finally leads to lower hardness in ferritic phase as shown in Figure 3.The HAADF-STEM image of nanometer-sized carbides as shown in Figure 4 directly reveals the distribution of Mo (the relative heavy element in the sample) and confirms the chemical composition of the nanometer-sized carbides.

References

1. Y. Funakawa, T. Shiozaki, K. Tomita, T. Yamaoto, and E Maeda, *ISIJ International,* 44 (2004) 1945.
2. R. W. K. Honeycombe, *Metall. Trans. A.* 7 (1976) 915.

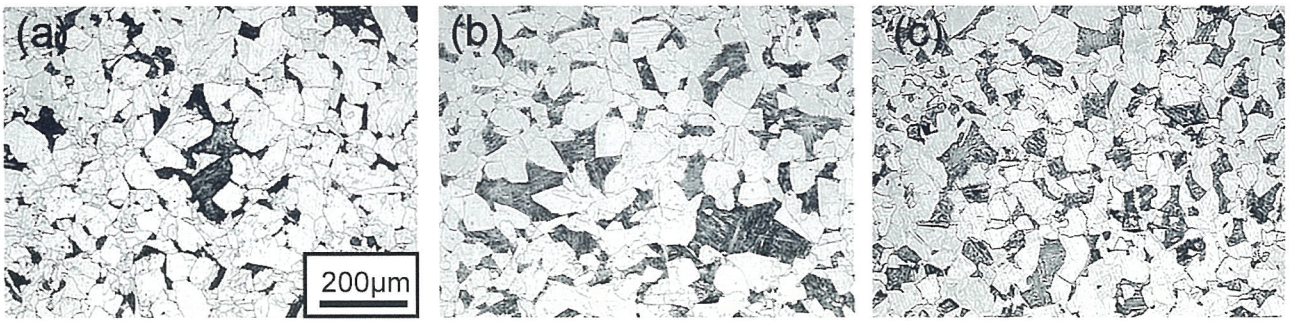

Figure 1 The macrostructure isothermally transforming at (a) 650, (b) 680, and (c) 700°C

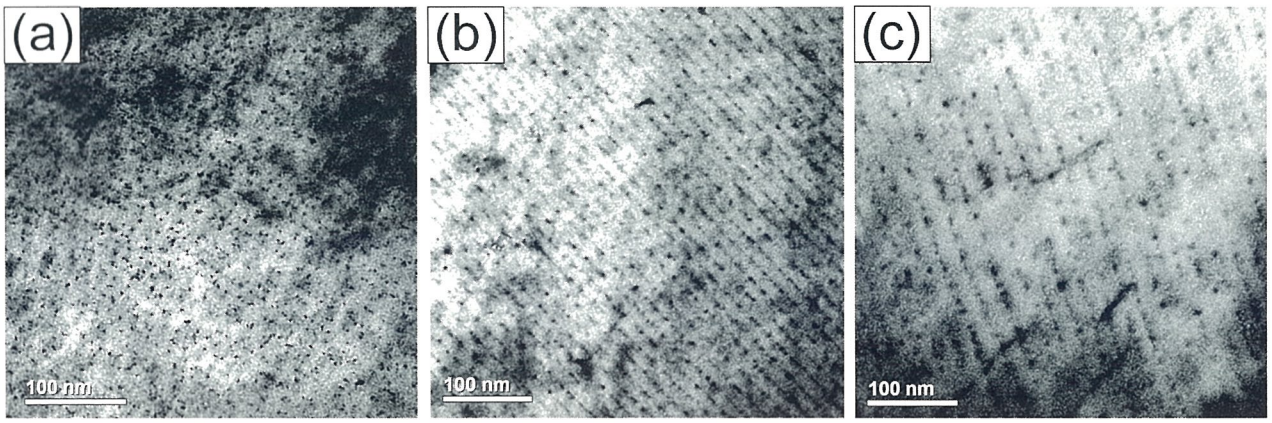

Figure 2 The microstructure of carbides isothermally transforming at (a) 650, (b) 680, and (c) 700°C

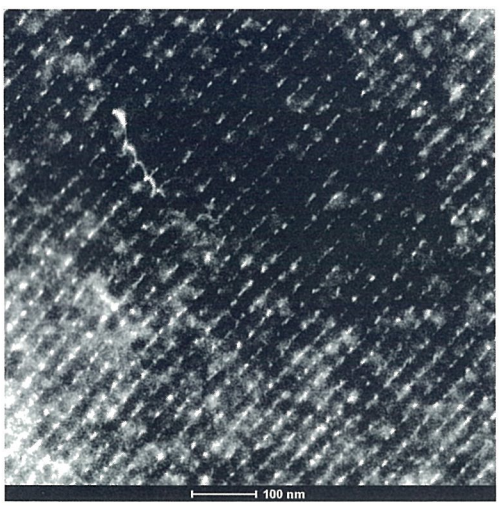

Figure 3 HAADF-STEM image of (Ti, Mo)C_x carbides formed at 680°C.

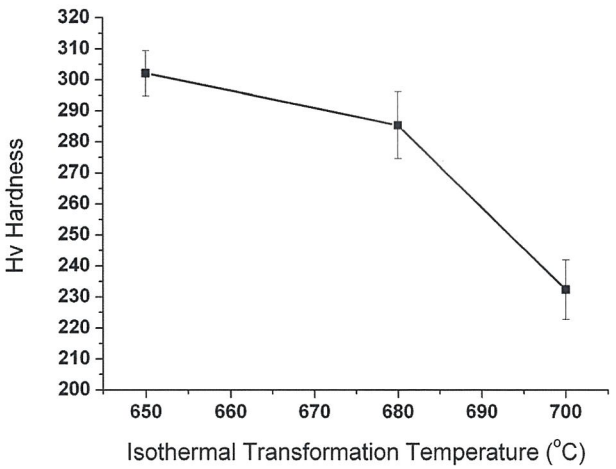

Figure 4 The Relationship between hardness in ferrite and the isothermal transformation temperatures.

M-P-23 EFFECTS OF REPEATED IMMERSIONS ON THE FORMATION OF CERIUM NITRATE CONVERSION COATINGS ON AZ31 MAGNESIUM ALLOY

Wei-Jen Li(李偉任) and Chao-Sung Lin(林招松)

Department of Materials Science and Engineering, National Taiwan University
Taipei 106, Taiwan

Non-Chromate conversion coating treatments are important, that solutions are such as cerium, phosphate/permanganate and stagnate[1-5]. This study was aimed for the effects of repeated immersions in cerium nitrate solution on the formation, corrosion resistance and adhesion. Even if the corrosion resistance of the conversion coatings has generally studied, the correlation of the microstructure is less well studied.

The open circuit potential was measured that keep a tap on formation rate of coating. The surface morphology was investigated by SEM as shown in Fig1. Fig. 1(a) and (b) are investigated many severe cracking on coating, and the surface had partial peel off. After repeated immersion process the coating defects were decreased as shown in Fig. 1(c) and (d). The coating structure and thickness were characterized by cross-section TEM preparation. Fig. 2 shows the cross-sectional TEM of cerium nitrate conversion coating. The coating was composed two layers, from outside to inner are compact layer and porous layer.[3] The major overlay of the coating was cerium oxide and hydroxide that had peeled partially from the substrate due to hydrogen evolution at the interface. In general, the coating with a CeO_2 overlay (compact layer) exhibited a golden yellow color, which became colorful as the coating became thicker.

Moreover, the corrosion resistance and impedance of the coating were measured by polarization test and ac impedance spectroscopy. ASTM D3359-97 was the frame of reference on adhesion test. Results shown the repeated immersions process increased the coating adhesion and corrosion resistance.

References

1. M. Dabala, K. Brunelli, E. Napolitani, M. Magrini, *Surf. Coat. Technol.*, **172**, 227-232 (2003).
2. K. Brunelli, M. Dabala, I. Calliari, M. Magrini, *Corros. Sci.*, **47**, 989-1000 (2005).
3. C. S. Lin and W. J. Li, *Mater. Trans.*, April, **47**, 1020-1025 (2006).
4. D. Hawake and D. L. Albright, *Metal Finishing*, October, 34 (1995).
5. C. S. Lin, H. C. Lin, K. M. Lin, W. C. Lai, *Corros. Sci.*, **48**, 93-109 (2006).

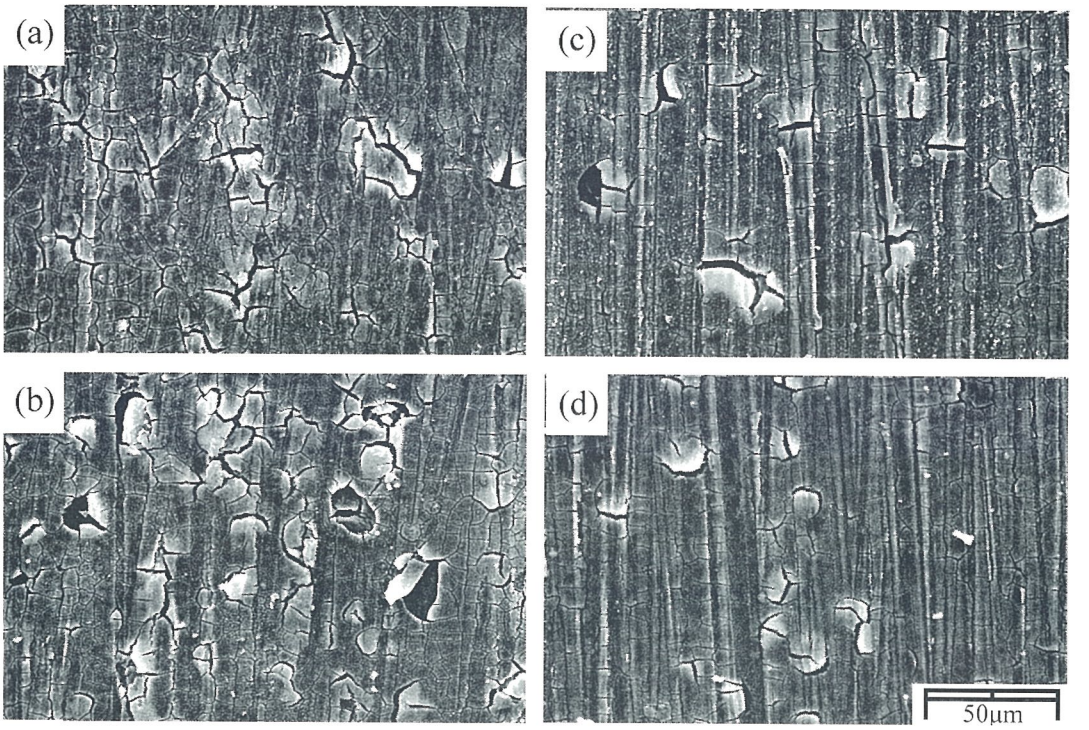

Figure 1 SEM micrograph of the cerium nitrate treated time : (a)60s; (b)180s, and repeated immersion treatmed time : (c)30+150s; (d)60+120s.

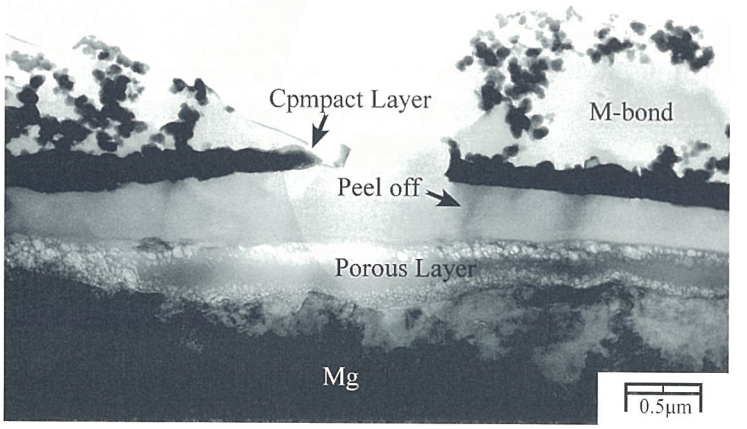

Figure 2 Cross-sectional TEM micrograph of the coated AZ31.

M-P-24 INFLUENCE OF APPLYING A BIAS ON THE CHARACTERISTICS OF TiVCr ALLOY THIN FILMS PREPARED BY DC SPUTTERING

Du-Cheng Tsai(蔡篤承), Hsiao-Chiang Yao(姚曉強) and Fuh-Sheng Shieua(薛富盛)*

Department of Materials Engineering, National Chung Hsing University, Taichung, Taiwan

In generally, pure metals exhibit poor yield strength and plastic deformation. In order to improve the resistance of metal coatings to damage by mechanical action, it is known from studies of evaporation and sputter deposition that the hardness of pure metal can be enhanced through the incorporation of impurities. It was believed that excellent mechanical properties could be expected in the ternary mixed TiVCr alloy films due to solid solution effect. Furthermore, it is noteworthy that the TiVCr can be very simple in composition and microstructure, and easy to analyze due to similar crystal structure and electronegativity.

The TiVCr alloy thin films were deposited on Si wafer by dc magnetron sputtering with power applied to the substrates. Effect of the bias ranging from 0 to -150 V on the microstructure and morphology of the thin films were investigated in detail by transmission electron microscopy (TEM) and field-emission scanning electron microscopy (SEM), respectively. The TiVCr alloy film without bias shows pyramid-like grains and many large voids appear among grains with a columns structure of small diameter (Fig. 1). At a bias of -80 V, the film shows distorted pyramid-like grains and become denser, but still has small voids among grains. It can be observed increase of lateral sizes of the individual columns and decrease of defect density (Fig. 2). As the substrate bias was increased to -150 V, irregular-shape grains began to replace the pyramid-like structure and the original column structure also becomes unapparent (Fig. 3). The greatly dense structure can be gained by applying a substrate bias of -150 V. There is no any data above substrate bias of -200 V in the article since the film appears bubbles and peels off the substrate. A clear conclusion can be successfully drawn from the results is the good correlation between the microstructure, hardness, and resistivity.

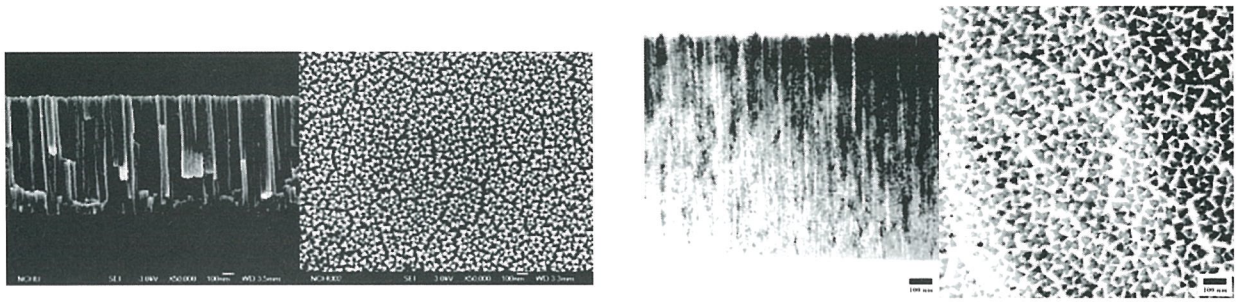

(a)

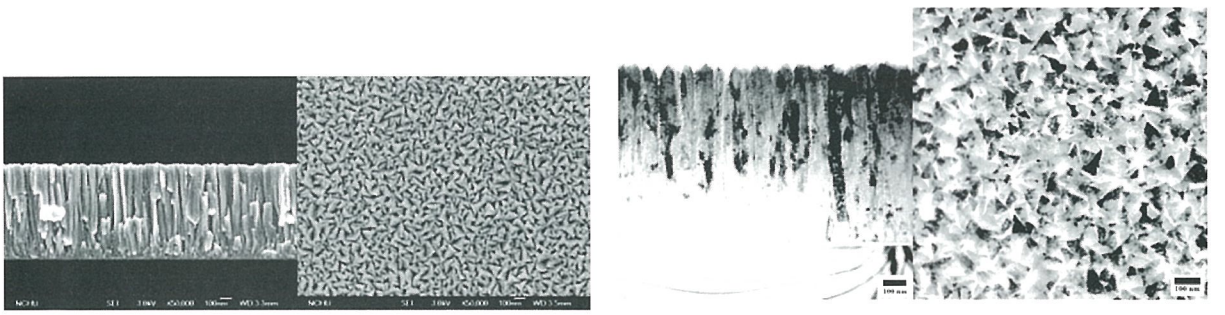

(b)

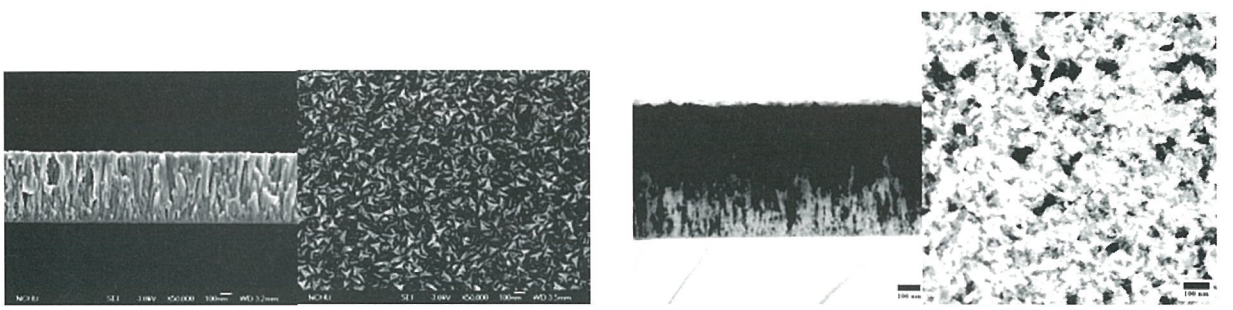

(c)

Figure 1. SEM and TEM images of the TiVCr films deposited at substrate biases of (a) 0V, (b) -80 V, and(c)-150 V

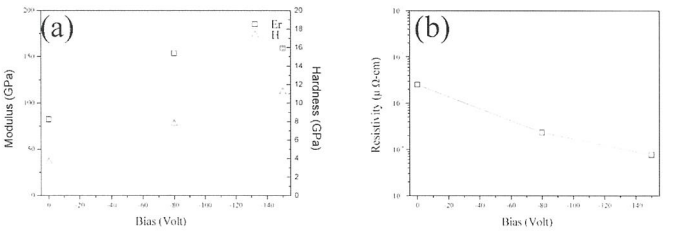

Figure 2. (a) Hardness, elastic modulus, and (b) resistivity of the TiVCr films deposited at various substrate biases.

M-P-25 STRENGTH MODULATION OF QUANTUM-WELL STATES IN PB ISLANDS WITH PERIODIC DISTORTIONS ON SI(111)

YANG, Min-Chi(楊敏麒)[1,2], LU, Shin-Ming(呂欣明)[1], SU, Wei-Bin(蘇維彬)[1], HSU, Tung(徐統)[2], CHANG, Chia-Seng(張嘉升)[1] and TSONG, Tien-Tzou(鄭天佐)[1]

[1] Institute of Physics, Academia Sinica, Nankang, Taipei, Taiwan
[2] Department of Materials Science and Engineering, National Tsing Hua University, Hsinchu, Taiwan

Recent studies using scanning tunneling microscopy (STM) and spectroscopy (STS) have demonstrated that quantum-well (QW) states in a metal film grown on a semiconductor can be a medium to transmit information about the metal/semiconductor interface structure to the surface. For instance, Altfeder et al. have shown that the periodic patterns appearing on thick Pb films are reflections of Pb/Si(111)7×7 and Pb/Si(111)1×1 interface structures, manifested through the QW states.[(1),(2)] Because of the different natures of these two interfaces, the mechanism of reflecting interface structures with QW states are not the same. Recent studies also demonstrate that this difference in interfacial properties may cause different preferred thicknesses of Pb islands,[(3)] though the growth of Pb islands on both interfaces is driven by the quantum size effect.[(4)] We will discuss its possible attribution to the electronic screening effect induced by the lattice distortion in Pb islands.

For this experiment a Si(111)7×7 surface was obtained by annealing the sample to 1400K and then slowly cooling it to room temperature. For preparing the Pb/Si(111)1×1 interface, slightly more than 1 monolayer (ML) of Pb was deposited onto the Si(111)7×7 surface at room temperature and followed by annealing at 750 K for a few seconds. After this process, the 7×7 structure was converted into a 1×1 bulk-terminated structure and a Pb film of an incommensurate (IC) phase was formed. By depositing an additional 1.8 ML Pb on the IC surface at 225 K, three-layer Pb islands were created. Figure 1(a) shows a typical topographic image of the grown Pb islands with thickness of three atomic layers on top of the Si(111) surface, taken at a sample bias of 0.2 V and image size is 890×740 $Å^2$. There appear two types of pattern marked by I and II on these islands. Figures 1(b) and 1(c) display the zoom-in images of type-I and type-II patterns, respectively. Image size of (b) and (c) is 185×77 $Å^2$. The sample was then transferred to a homebuilt STM in which the sample was cooled to 103 K. For detecting the electronic contribution in the pattern at different biases, we use Z-V spectroscopy to probe the electronic structures of Pb islands. Figure 2 shows spectra acquired using the lock-in technique for filled and empty states. The colors of the spectra correspond to those of the crosses in Figs. 1(b) and 1(c). We can observe one peak of the QW state in

each filled state and empty state for all acquired position on both types of pattern.

Our results demonstrate that the pattern on the island surface appears as the superposition of geometric corrugation and local variation of the electronic structure. The former originates from two kinds of interface relaxation, resulting in two types of periodic distortion of the lattice. The latter is due to the periodic strength modulation of quantum-well states in Pb islands, causing inhomogeneity in the integration of the density of states and the bias-dependent pattern. This strength modulation of the quantum-well states can be attributed to the electronic screening effect induced by the lattice distortion in Pb islands.

The authors would like to acknowledge C. S. Kuo, C. Y. Lin, and C. H. Hsieh for assisting in the construction of the STM. This work was supported by the National Science Council, Academia Sinica, and the project of Academic Excellence of the Ministry of Education of Taiwan.

References:

1. I. B. Altfeder, D. M. Chen, and K. A. Matveev, Phys. Rev. Lett. 80, 4895 (1998).
2. I. B. Altfeder, V. Narayanamurti, and D. M. Chen, Phys. Rev. Lett. 88, 206801 (2002).
3. V. Yeh, L. Berbil-Bautista, C. Z. Wang, K. M. Ho, and M. C. Tringides, Phys. Rev. Lett. 85, 5158 (2000).
4. Z. Zhang, Q. Niu, and C.-K. Shih, Phys. Rev. Lett. 80, 5381 (1998).

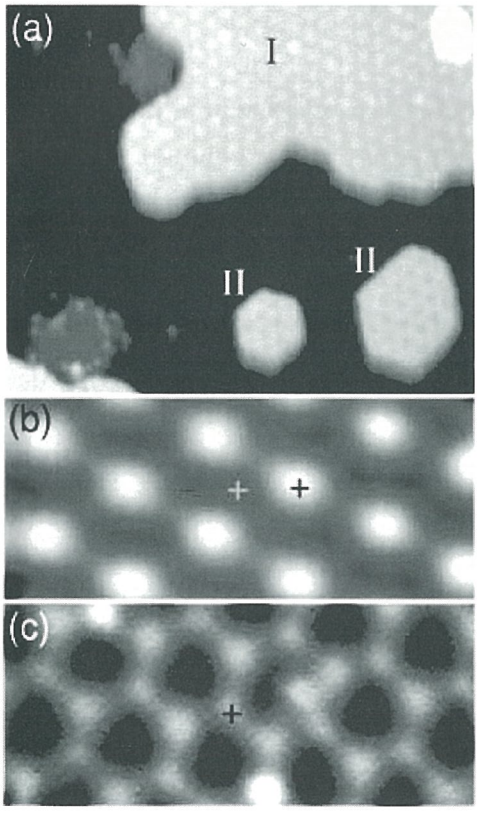

Figure 1

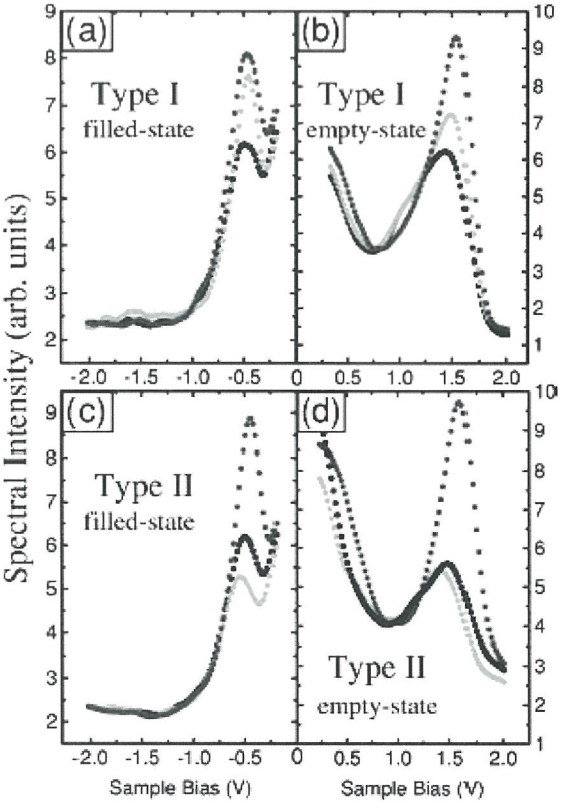

Figure 2

M-P-14 Table 1 Chemical composition of sample. (mass%)

Element	Ni	Fe	Cr	Nb	Mo	Ti	Al	Co	Mn
Content	52.73	18.01	19.20	4.66	2.80	0.94	0.52	0.65	0.11

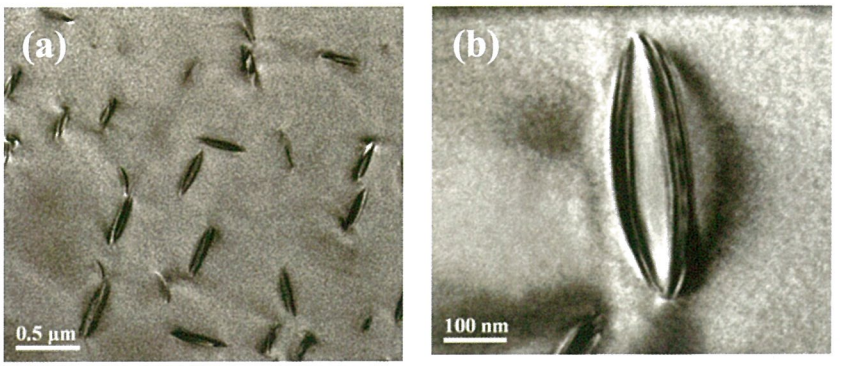

Fig. 1 TEM micrograph of γ'' precipitates from the γ matrix aged at 900℃ for 10 hours: (a) overview of γ'' precipitates within γ matrix, (b) enlarge micrograph.

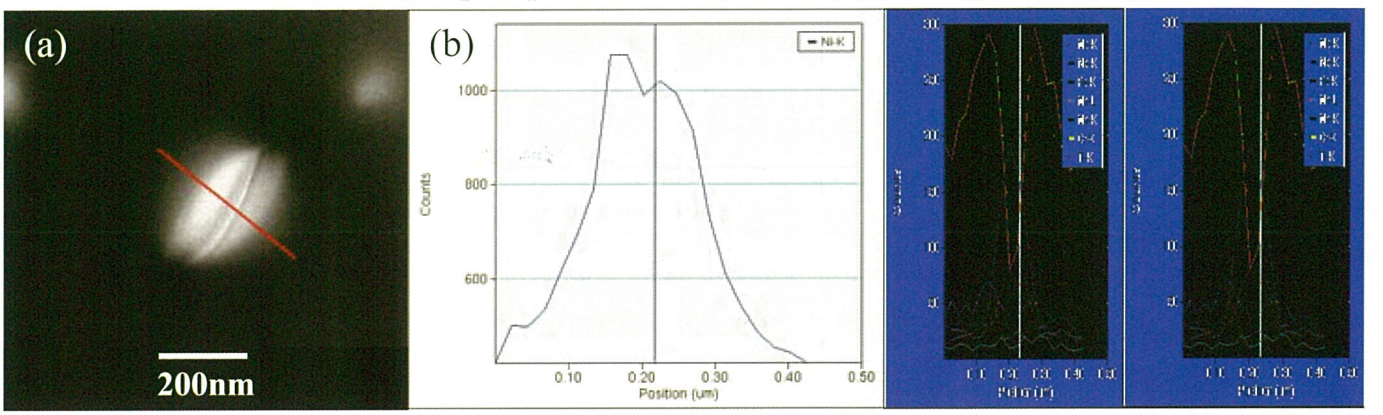

Fig. 2 (a)HAADF image (a) and (b)EDS intensity profile of the γ'' precipitate. The EDS intensity profile is obtained along the line in (a).

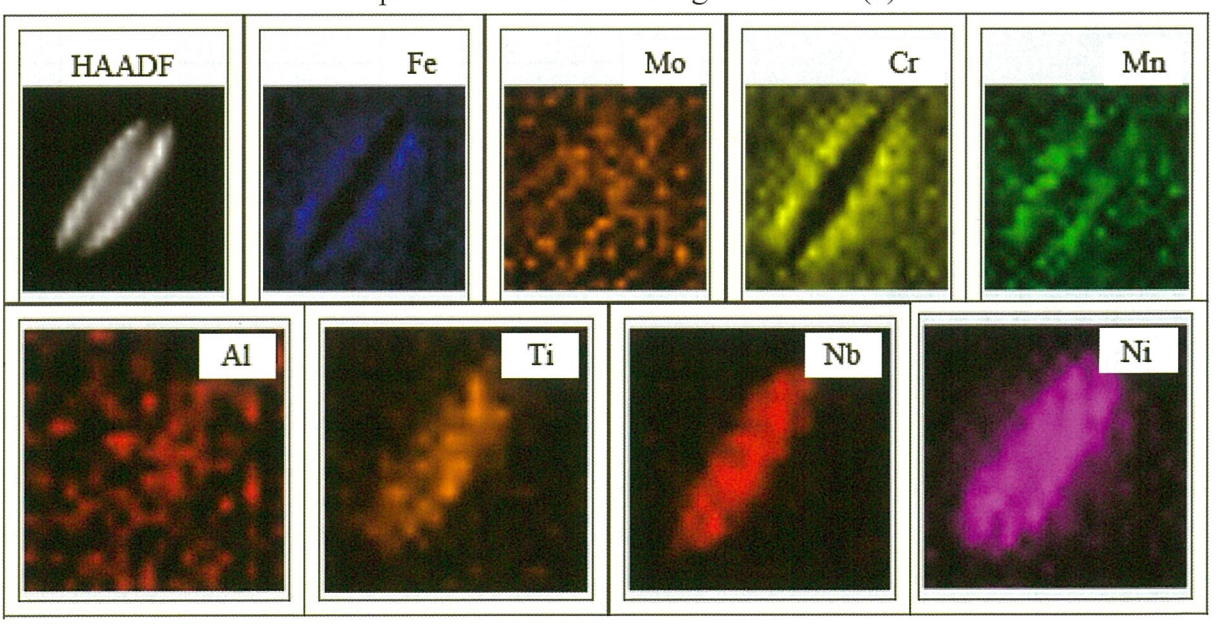

Fig. 3 EDX mapping of γ'' precipitate containing some levels of Fe, Mo, Cr, Mn, Al, Ti, Nb and Ni.

Authors' names and address(in Chinese)

李威志

10617 臺北市羅斯福路四段一號 chief author: 李威志 phone: 02-3366-1353

台灣大學材料科學與工程學系暨研究所 e-mail: d94527006@ntu.edu.tw

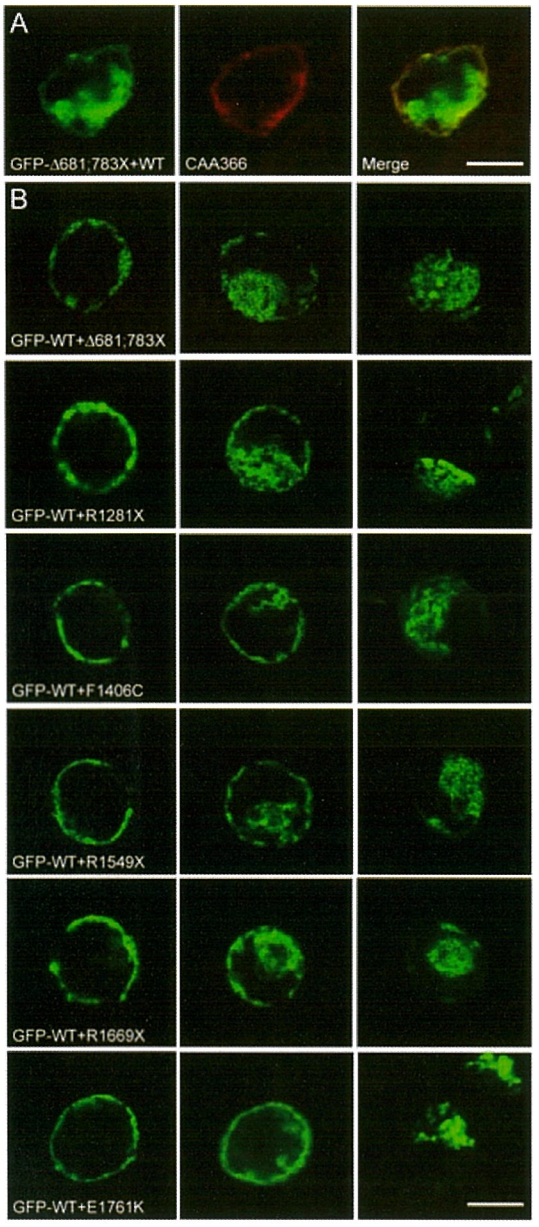

Figure 1. HEK293T cells co-expressing wild-type and EA2 mutant CaV2.1 channels. (A) Cells co-transfected with untagged wild-type α1A subunit and GFP-tagged mutant α1A-Δ681;783X, as well as auxiliary α2δ and β4 subunits. The cells were also counterstained with the CAA366 antibody which recognized the wild-type α1A subunit but not the mutant α1A-Δ681;783X. Note the co-existence of the fluorescence for CAA366 (*red*) and GFP (*green*) in the same cell. (B) Representative GFP fluorescence images of HEK293T cells expressing GFP-tagged wild-type CaV2.1 channels in the presence of untagged EA2 mutants. Three representative midsection cell images are shown for each of the six co-expression conditions to exemplify the three localization patterns: membrane-dominant (*left panels*), cyto-membrane (*middle panels*), and cytoplasm-dominant (*right panels*). Scale bar = 10μm.

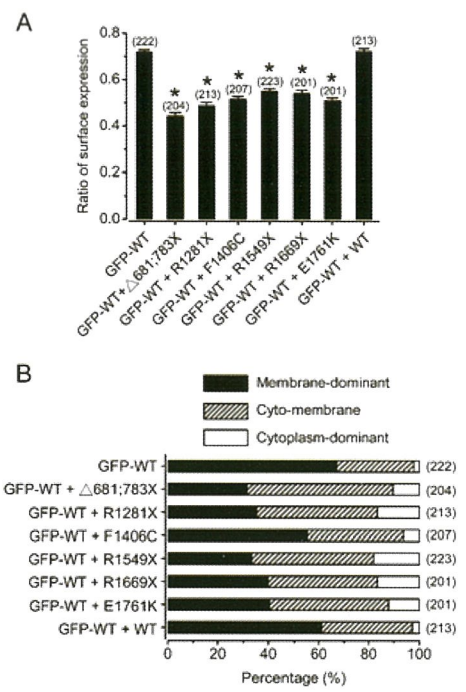

Figure 2. Quantitative analyses of the membrane localization of wild-type CaV2.1 channels in the presence of EA2 mutants. (A) Mean ratios of surface expression for GFP-tagged wild-type channels in the presence of different α1A constructs. (B) Cellular distribution percentages of the three localization patterns of GFP-tagged wild-type channels in the presence of different α1A constructs. The numbers in parentheses refer to the number of cells analyzed for each co-expression condition.

益弘儀器股份有限公司

台北 (02)2755-2266　新竹 (03)578-2020　Website: www.ehong.com.tw
臺中 (04)2245-2181　臺南 (06)209-5135　高雄 (07)334-0407　昆山 (0512)57385666

Hitachi 日立電子顯微鏡

Field Emission PC-SEM S-4800

解像力 1.0nm (at 15Kv)
解像力 1.4nm (at 1Kv)

IN-LENS Field Emission PC-SEM S-5500

解像力 0.4nm (at 30Kv) 1.6nm (at 1Kv)

PC Windows 全自動操作 可變真空電子顯微鏡

解像力 3.0nm / 4.0nm (V.P) [S-3700N 12"含 TMP]
解像力 3.0nm / 4.0nm (V.P) [S-3400N 8" 含 TMP]
解像力 3.0nm / 4.0nm (V.P) [SU-1500 6"] NEW!

週邊附件及前處理設備：

※ HITACHI / EMITECH (Quorum)各式 SPUTTER 蒸鍍機及 CPD
※ HORIBA EDX/ WDS / EBSD
※ HITACHI / E-3500 (Cross-Section Ion Milling System)
※ HITACHI /IM-3000 (Surface Ion Milling system)

桌上型電子顯微鏡 TM-1000

1. 桌上型節能設計
2. 簡單易懂操做方式
3. 對無鍍金處理的絕緣樣品進行觀察
4. 表現深度，展現物體的立體感
5. 可加 EDS 附件，偵測 Na(11)-U(92)元素

==========

※ HITACHI FIB FB-2100/NB5000 (Dual Beam)
※ HITACHI PC-TEM H-7650 (120KV)
※ HITACHI STEM HD-2300A
HD-2700 (Cs correction)
※ HITACHI FE-SEM S-4300
※ HITACHI Analytical FE-SEM SU-70(Schottky) / SU-6600(Low vacuum)

Radnoti

血管環微張力監測系統

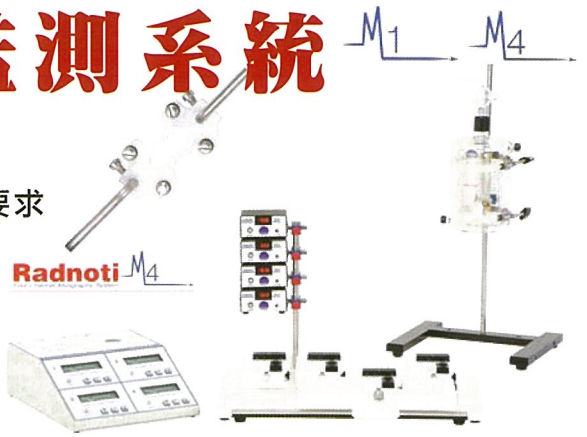

- 適用60um至>1mm直徑之血管環
- 0-0.5gm高靈敏電容式微張力傳感器
- <12.5um位移@0.5gm，成就嚴苛等長量測要求
- 精確數位溫控監測5ml組織槽
- 附電池照明艙槽便於標樣檢視
- 傳感器安全鎖鈕提供過載推頂保護
- 符合人體工學之滑動腕托
- 易於重行組配之模組式設計

如何架裝血管環段及調整張力?

1. 兩平行細絲各自穿過標樣管腔，並分別附著至微小血管支撐架。
2. 每一血管支撐架牴觸表面皆精刻微凹槽以利細絲就定位。
3. 一支架連至微張力傳感器；另一支架至前後調動之精密微標器。
4. 藉上下/左右定位調控鈕以精確調校微小血管支撐架。
5. 兩平行細絲藉鎖定螺絲錨定至個別之支撐架。

※ 各個鎖定螺絲於螺帽下加套軸襯以利細絲咬合

6. 藉調控微標器之前後移動以施加預載張力。

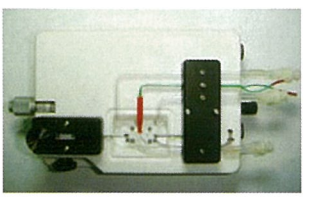

小鼠應用例:

- 主動脈環
- 小腸環
- 腸系膜動脈

TBSI

Developing Tethered and Wireless Solutions for Neurophysiology

神經生理研究之客製化電子積體元件

TBSI (Triangle BioSystems, Inc)專業致力於開發並製造積體生物電子元件及儀器設備。其應用於從腦內或從腦外刺激並擷取神經活性之技術，一向引領該專業領域。

他們設計並生產之專利、摻和信號積體電路及相關系統，同時嘉惠學術研究者及商用新猷研究開發者。

TBSI提供高性能繫線及無線監測系統解決方案以肆應當今日新月異、蔚然大器之神經生理研究。其神經生理研究產品包括：

got wireless?

SciWorks資料擷取/信號分析系統

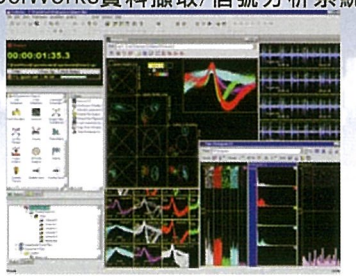

A. 無線遙測記錄系列

- 4頻道無線放大/發射子
- 15頻道無線放大/發射子
- 31頻道無線放大/發射子
- 無線前級接收器

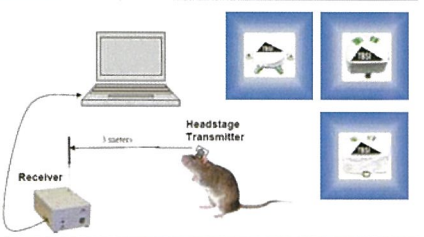

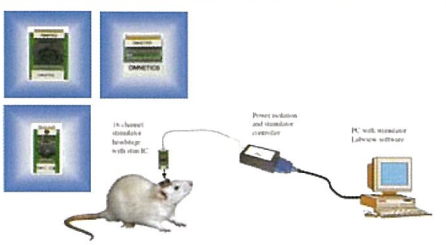

B. 繫線監測記錄系列

- 8或16頻道繫線放大子
- 34頻道繫線放大子
- 主動增益微電極陣列子

日龍儀器股份有限公司

106台北市和平東路二段100號2F-6
電話: 02-27335111 傳真: 02-27332552
E-mail : ubl@ms9.hinet.net

813高雄市左營區太華街278號
電話: 07-5590250 傳真:07-5590251
http://www.upwards.com.tw

Image-Pro® PLUS

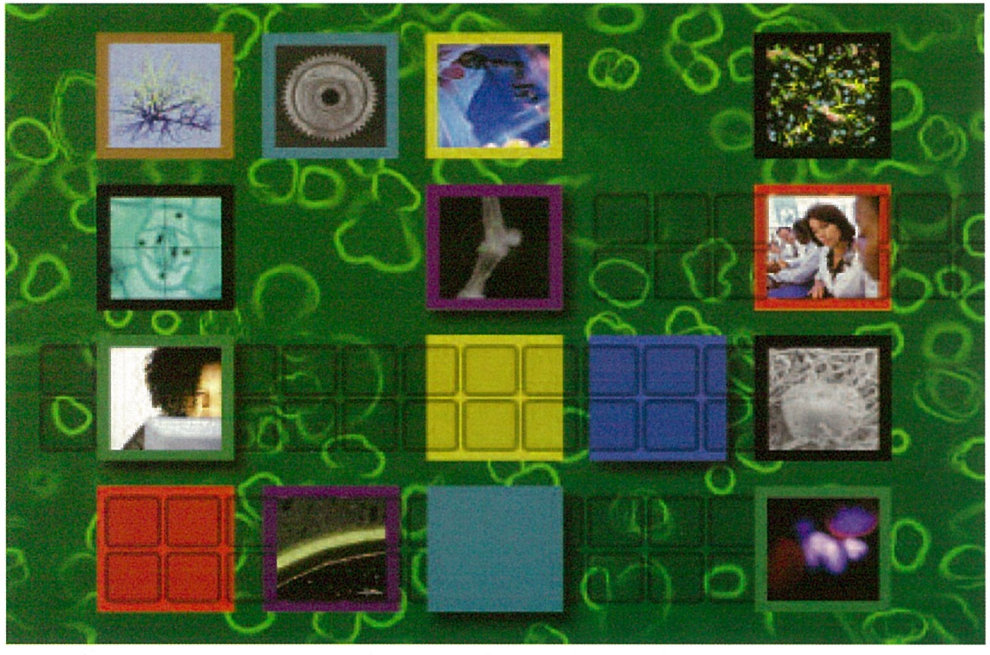

Image-Pro® Plus

Powerful and Customizable
Image Processing and Analysis Software

MediaCybernetics
From Images to Answers®

OPTRONICS

ISO 9001:2000 CERTIFIED
Medical Grade Microimaging Systems™

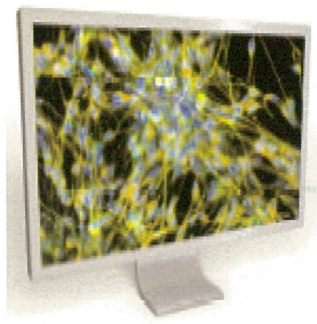

MICROFIRE

Research Grade CCD Imaging for Microscopy

Real-Time Progressive Scan Megapixel Microscope Camera System

- 2-Megapixel Color Imaging
  1600 X 1200 effective pixels creates exceptional image detail and dynamic range in both brightfield and low-light fluorescent images.
- Optronics Exclusive PictureFrame®
  Comprehensive image processing suite with measurement and annotation, scale bar, AVI file-compliant time-lapse imaging, automated image archiving, six position image mixing functionality, flat field correction, background subtraction, live frame averaging with motion compensation and more...
- Direct X Powered
  Real-time, full resolution, full screen preview.
- Intuitive Human Interface
  Powerful software – simple interface means images are captured effortlessly with Optronics point and shoot simplicity.
- TWAIN Compatible Software
  Instantaneous integration within popular imaging applications.
- FireWire® Interface
  Offers "Plug and Play" connectivity from a desktop or laptop computer with data transfer up to 400 mbs.

北區授權經銷商 集可企業有限公司 台北市信義路四段273號5樓 TEL：(02)2704-9669

OLYMPUS

Your Vision, Our Future

RESEARCH SYSTEM MICROSCOPE

BX51/BX61

BX2 SERIES

UIS2

Everything for digital imaging

元利儀器股份有限公司

台中市文心路三段1023號6樓

TEL:04-22933161

FAX:04-22973049

TESCAN
DIGITAL MICROSCOPY IMAGING

Extraordinary FIB-SEM&FESEM&SEM

LYRA\\FIB-SEM

MIRA\\FESEM

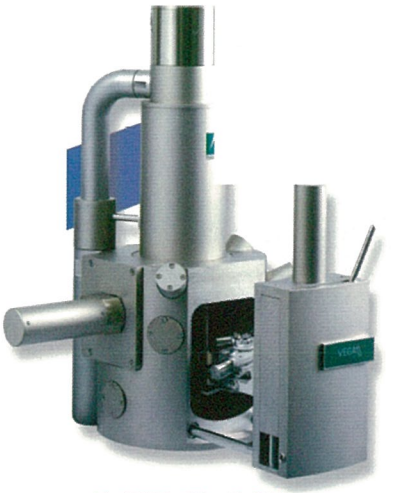

VEGA\\SEM

- TESCAN MIRA\\獨家即時In-Flight Beam Tracing™ ，使工作效能最佳化
- TESCAN獨家Wide Field Optics™設計，提供多樣化之影像模式
- 遠端遙控操作與即時通訊 >>> 搭配 EDS/ WDS/ EBSD 多元組合•自行選擇

BAL-TEC
Preparation to view information

CRITICAL POINT DRYER CPD 030

臨界點乾燥機 CPD030

- 使用於生物試片及微機電樣品之臨界點乾燥
- 低 CO2 用量消耗
- 全自動化冷卻及加熱系統功能
- 大樣品室觀察窗
- 多樣化選擇功能

The economical solution for critical point drying

—— 顯微世界 皓睿專業 ——

Add：北市大同區長安西路56號8F
Tel：(02) 2555-5888
Fax：(02) 2555-5875
http://www.hsictech.com

皓睿科技
Harvest Scientific Corporation

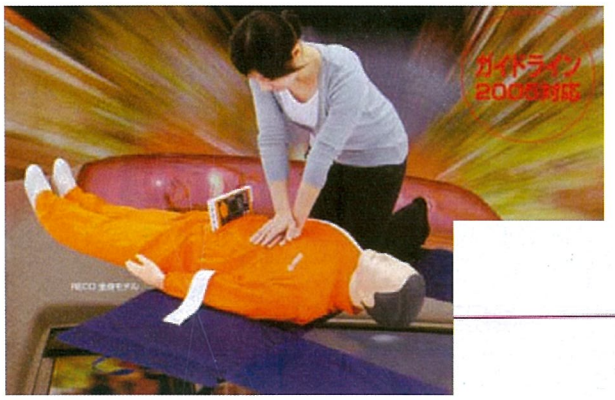

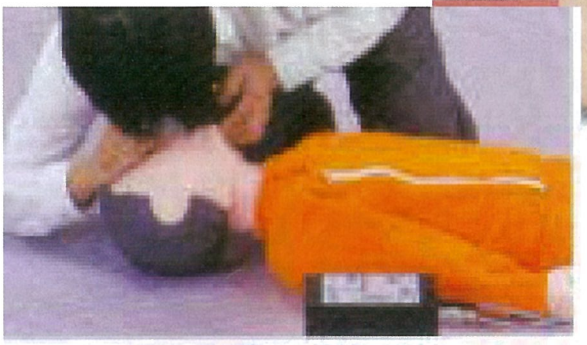

專業代理歐、日、美

幼教模型、急救教材、保健室器材、衛生示教模型、動物塑化標本
生物組織玻片、人體解剖示教模型、急救甦醒安妮模型、
護理專業教室及無障礙空間規劃、模擬病房 / 安寧 / 重症 / 長期照護

群鈺科學股份有限公司

TEL:02-25635636
FAX:02-25363097
台北市中山區民權東路二段26號12樓之8